

**Structural and Biochemical Characterization of the α I-domain, the Ligand
Binding Domain, of Integrins α D β 2 and α X β 2**

by
Collins Aboagye

A dissertation submitted to the Department of Biology and Biochemistry,
College of Natural Sciences and Mathematics

in partial fulfillment of the requirements for the degree of

DOCTOR OF PHILOSOPHY

in Biochemistry

Chair of Committee: Mehmet Sen

Committee Member: Robert J Schwartz

Committee Member: James Briggs

Committee Member: Mark A. White

University of Houston
December 2021

DEDICATION

To my wife and family

ACKNOWLEDGMENTS

This journey, although being one of the most difficult and unforeseen challenges that I have ever experienced, has helped me evolve as an individual. I would first like to thank Dr. Mehmet Sen for being my advisor. I am very grateful that he accepted me in his lab. He has directed my research with the upmost interest and patience making my experience very enjoyable. He has instilled in me the knowledge and shown me the needed techniques necessary to carry out my research. His hard work, dedication, and professional encouragement inspired me to develop and learn the work ethic needed to complete this work. I can't thank him enough for everything he has done for me.

I would also like to express my gratitude to my committee members, Dr. Jim Briggs, Dr. Robert Schwartz, and Dr. Mark White for accepting to be on my committee and for their intellectual support in my academic career.

I would like to acknowledge the members of my laboratory, those who have long moved on to other endeavors and current ones, Dr. Pragya Manandhar, Zeinab Moussa, Omar Abousaway, Tannon Yu, and Micah Castillo, for the help and the good times experienced in the laboratory. I also acknowledge Dr. William R. Widger and members of the Widger laboratory, Jonathan Rangel, and Dr. Abiodun Bodunrin, for all the support and brilliant ideas/discussions during our joint meetings.

Additionally, I would like to express my gratitude to Dr. Donald Raymond, of Broad Institute of MIT and Harvard, for his help on my protein structure determination.

Finally, I would like to thank my family and friends both home and abroad for their tremendous support, love, and understanding during my most stressful times. Mom, Dad, Kofi, and Grace, thank you very much for your motivation and prayers throughout all the long nights

and struggles. Mr. and Mrs. Ekow Kwakye, thank you for always supporting me and taking me into your home as part of your family. I would also like to express my outmost gratitude to my loving wife, Mrs. Adwoa Boatemaa Aboagye. I have no idea where I would be now without you, especially the last four years. You have been with me through it all and supported me with your endless and unconditional love which enabled me to complete this work. Thank you all again for what you have done for me. I am forever grateful and in your debt. Here's to the next adventure!

ABSTRACT

β 2-integrins are among the most complex cell surface metallo-receptors known, and upon ligand binding, its ligand-binding domain (α I-domain) undergoes allosteric conformational changes. These “shape-shifting” events of the α I-domain are key to the mechanism of integrin action allowing metal-dependent bidirectional regulation of cellular signaling across the cell membrane in events such as migratory behavior and inflammatory responses of myeloid cells. α D β 2 was specifically detected and showed a distinctive contributing role in the inflammatory response in human atherosclerotic lesions and white adipose tissue during metabolic syndrome. α D β 2 appears to be a unique regulatory receptor in macrophage retention and egress in the inflamed tissue and thus, is emerging as a potential drug target. However, perhaps since it was very recently discovered, the recognition specificity and the molecular basis of α D β 2 ligand-binding are essentially unknown. Herein, we determined the structure of the α D I-domain without divalent cation and in the presence of the chloride salts of Mg^{2+} . While overall the α D I-domain structures are highly similar to other α I-domains, several residues in the vicinity of its MIDAS differ from other α I-domain, which, together with change in surface charge, revealing why some α I-domains recognize an overlapping set of ligands with different affinity as well as a set of non-overlapping ligands. The thermal stability as well as the α D I-domain affinity are altered by metal ions. Metal ions endow unique ligand-affinity and thermodynamic stability to the α D I-domain structure. We also discovered that α D β 2 binds to iC3b molecule, a complement factor in the immune system, in a metal-dependent manner.

The α X I-domain structure has been extensively studied by X-ray crystallography. However, these crystal structures only provide the average positions and arrangement of individual atoms of this protein in either metal-ion free state or open state NMR experiments are able to probe

molecular motions at the nanosecond timescale and are ideal for studying the transition between the open and closed states in integrins. Here, we report the triple resonance NMR backbone assignment of the αX I-domain integrin, as a preliminary experiment for future structural and dynamic studies.

TABLE OF CONTENTS

<i>DEDICATION</i>	<i>ii</i>
<i>ACKNOWLEDGMENTS</i>	<i>iii</i>
<i>ABSTRACT</i>	<i>v</i>
<i>LIST OF TABLES</i>	<i>ix</i>
<i>LIST OF FIGURES</i>	<i>x</i>
<i>LIST OF ABBREVIATIONS</i>	<i>xiii</i>
<i>Chapter I: Biochemical and Structural Characterization of αD I-domain of the Integrin αDβ2</i>	<i>1</i>
1 INTRODUCTION	1
1.1 Cell surface receptors	1
1.2 Integrin superfamily	2
.....	4
1.3. Leukocyte-specific integrins	4
1.4. Tissue and cellular distribution of leukocyte β 2 integrins.....	5
1.5. Ligands of leukocyte β 2 integrins	6
1.6. Integrin structure	7
1.6.1. Extracellular domains	7
1.6.2. The membrane spanning or transmembrane helices.....	10
1.6.3. The cytoplasmic tail	11
1.7 Integrin activation and conformational changes.....	12
1.8.1 Integrin α D β 2: chromosomal location and expression	14
1.8.2. The roles/importance of α D β 2.....	14
1.8.3 Ligands of α D β 2	16
1.9. Divergence, structural features and conformational changes of the α I domains.....	17
1.9.2 Cation binding to integrins.....	22
2. MATERIALS AND EXPERIMENTAL PROCEDURES	24
2.1 The α D I-domain expression	24
2.2 Purification of integrin α D I-domain	25
2.3 Crystallization	26
2.3.1 Screening	26
2.3.2 Optimization	27
2.4 X-ray diffraction and structural determination.....	29
2.4.1 X-ray diffraction data collection.....	29
2.4.2 Indexing and integration of X-Ray data	29
2.4.3 Structure determination	29
2.4.4 Model building and refinement	30
2.4.5 Structure validation and figure preparation	31
2.5 Differential Scanning Fluorimetry (DSF).....	31
2.7 E-IgM-iC3b Rosetting assay	33
2.8 Epitope exposure.....	33
2.9 Flat bottom adhesion assay	33
3. RESULTS	35
3.1 Expression and purification of the α D I-domain.....	35
3.2 Crystal structure of the α D I-domain integrin protein	38

3.2.1 Crystallization of α D I-domain	38
3.2.2 Data collection, molecular replacement and structure refinement	49
3.3 X-Ray structure of the α D I-domain	54
.....	56
3.4 Difference between M^{2+} -free and M^{2+} containing α D I-domain Structures.....	56
3.5 Surface charge of the α D I-domain crystal structure	58
3.6 Comparison of the α I-domains	59
3.7 Characterization of α D I-domain, the ligand binding domain of leukocyte integrin α D β 2, affinity to divalent cations	65
3.7.1 Introduction.....	65
Results.....	69
3.7.2 The α D I-domain stability is affected by M^{2+} -ion-binding	69
3.7.3 Thermodynamics of divalent cation affinity to the α D I-domain	74
3.8 Functional characterization of α D β 2 with the β 2-specific mAbs and M^{2+} ions	77
3.8.1 Binding of α D β 2 to E-IgM-iC3b (Cell based assay by Zeinab Moussa).....	77
3.8.2 Functional characterization of α D β 2 with the β 2-specific mAbs	77
3.8.3 Differential effect of M^{2+} -ions in α D β 2 ligand binding	80
4. DISCUSSION.....	81
5 CONCLUSION AND FUTURE PROSPECTS	89
5.1 Conclusion	89
5.2 Future prospects	91
 <i>Chapter II: The integrin αX I-domain: Expression, Purification and Triple Resonance Backbone Assignment.....</i>	
1. INTRODUCTION.....	93
1.1 Integrin α X β 2: chromosomal location and expression	94
1.2 Roles/Importance and effect of α X β 2 expression.....	94
1.3 α X β 2 ligands	96
1.4 The α X I-domain	96
2 MATERIALS AND EXPERIMENTAL PROCEDURES.....	99
2.1 Expression and purification of α X I-domain in minimal media.....	99
2.2 Expression of double-labelled α X I-domain in minimal media	99
2.3 Expression of triple-labelled α X I-domain in minimal media	100
2.4 Purification of NMR samples.....	101
2.5 NMR sample conditions and acquisition	102
2.6 Triple resonance experiments and backbone specific NMR assignment	102
3. RESULTS.....	104
3.1 Expression and purification of isotopically labeled α X I-domain	105
.....	107
3.2 15 N heteronuclear single quantum coherence (HSQC) experiment.....	107
3.3 NMR backbone assignment	109
5 CONCLUSION AND FUTURE DIRECTIONS	115
<i>APPENDIX I: Media, gels and buffers for αD I-domain sample preparation.....</i>	<i>116</i>
<i>APPENDIX III: Media and buffers for NMR sample preparation</i>	<i>123</i>
<i>Bibliography.....</i>	<i>130</i>

LIST OF TABLES

Table 1. Concentration of syringe and cell contents in each α D I-domain- M^{2+} -ion titration.....	32
Table 2. Hampton Research Index-HR2-130 screen reagents that were selected for optimization and the description of the crystalline material they produced.....	41
Table 3. Hampton Research Index-HR2-144 screen reagents that were selected for optimization and the description of the crystalline material they produced.....	41
Table 4. Molecular Dimensions screen ProPlex (MD1-38) reagents that were selected for optimization and the description of the crystalline material they produced.....	43
Table 5. Data collection and refinement statistics.....	50
Table 6. Sequence identity, pI and estimated surface charge comparison between the α D I-domain and its homologous β 2 integrin family members. The total surface charge for each protein was computed in PYMOL.....	61
Table 7. The melting temperatures obtained for the α D I-domain- M^{2+} -ion binding experiment via DSF.....	70
Table 8. Values of thermodynamics parameters—Gibbs free energy (ΔG), enthalpy (ΔH), entropy (ΔS) of M^{2+} -ions affinity to the α D I-domain.....	75
Table 9. Significant variations in the amino acid residues around the MIDAS region of α D I-domain and its closest homologues.....	82
Table 10. NMR Acquisition Parameters.....	102

LIST OF FIGURES

Figure 1: Schematic diagram of different types of cell surface receptors.....	2
Figure 2: Classification of integrin family of heterodimers.....	4
Figure 3: Integrin structure and domain organization.....	9
Figure 4: Schematic of different integrin conformations.....	13
Figure 5: Integrin structure showing the multiple functional domains.....	19
Figure 6. Structural rearrangement of the α M I domain MIDAS.....	21
Figure 7: Illustration of vapor diffusion methods of crystallization.....	28
Figure 8: FPLC purification of the α D I-domain protein by affinity chromatography and the SDS-PAGE analysis.....	36
Figure 9: FPLC purification of the α D I-domain protein by gel filtration chromatography and the SDS-PAGE analysis.....	37
Figure 10: Gel filtration purification of digested α D I-domain protein by FPLC and the SDS-PAGE analysis.....	38
Figure 11: First crystals of α D I-domain obtained using Hampton Research's HT-HR2-130 crystal screen.....	40
Figure 12: Crystals of the α D I-domain obtained using Hampton Research's HT-HR2-144 crystal screen.....	42
Figure 13: Crystals of the α D I-domain obtained using Molecular Dimensions screen ProPlex (MD1-38) crystal screen.....	43
Figure 14: The birefringent and multilayered irregularly shaped crystals of the α D I-domain obtained after optimization of the Hampton Research crystallization conditions.....	45
Figure 15: Clear/birefringent long rods, rod clusters, and three-dimensional crystals of the α D I-domain obtained after final optimization of the Hampton Research crystallization conditions.....	46
Figure 16: Crystals of the α D I-domain protein after refining crystallization conditions with formulation reagents from the Molecular Dimensions screen.....	47
Figure 17: Crystals of the α D I-domain grown in a reservoir containing 0.1 M HEPES buffer and 12.5 % - 25% w/v PEG 3,350.....	48

Figure 18: A high-resolution diffraction image of the (A) Mg ²⁺ -bound (PEG3350 precipitant) and (B) Mg ²⁺ -free (Malic acid precipitant) αD I-domain.....	51
Figure 19: Ribbon representation of the two models of αD I-domain.....	52
Figure 20: Ramachandran outliers in the refined model of αD I-domain protein.....	53
Figure 21: The hydropathy index plot of αD I-domain protein sequence.....	54
Figure 22: Annotated cartoon diagram of the refined model structure of the αD I-domain protein showing the secondary structure composition.....	55
Figure 23: Representation of the MIDAS region of the αD I-domain.....	56
Figure 24: Structural changes between two crystal lattices with and without Mg ²⁺ -ion.....	57
Figure 25: Electrostatic surface charge representation of integrin αD I-domain.....	59
Figure 26: Sequence alignments of the β2 integrin family.....	60
Figure 27: Illustration of the MIDAS residues (conserved residues) of the αD I-domain and homologous structures.....	62
Figure 28: (A) Differences in helical propensity of the α7-helices of members of the β2 integrin αI-domain.....	63
Figure 29: Differences in the electrostatic surface charges was obtained by PYMOL.....	64
Figure 30: Schematic representation of thermal shift assay using DSF.....	67
Figure 31: Representation of basic principle of ITC technology and experimental curves.....	68
Figure 32: the Hofmeister or lyotropic effect via increasing the ionic strength did not contribute to the increase in the T _m of the αD I-domain.....	71
Figure 33: M ²⁺ -binding affect the stability of the αD I-domain.....	72
Figure 34: M ²⁺ -binding affect the stability of the αD I-domain.....	73
Figure 35: The ITC plots represent the change in the enthalpy during metal ion titration.....	76
Figure 36: E-IgM-iC3b binding assay and rosetting micrographs.....	78
Figure 37: Differential effect of different M ²⁺ -ions in three different concentrations are probed in our fibrinogen binding assays.....	79
Figure 38. Structural rearrangements during integrin activation.....	96
Figure 39. Difference in the magnesium coordination at MIDAS in the closed and open states of the αX I-domain.....	97

Figure 40: Affinity chromatography purification of the α X I-domain protein and SDS-PAGE Analysis.....	105
Figure 41: FPLC purification of α X I-domain protein by gel filtration chromatography and the SDS-PAGE analysis.....	106
Figure 43: FPLC purification of the α X I-domain by size exclusion chromatography and the SDS-PAGE analysis.....	107
Figure 44: HSQC of double labeled α X I-Domain.....	108
Figure 45: HSQC of triple labeled α X I-domain.....	109
Figure 46. $^2\text{D}/^{13}\text{C}/^{15}\text{N}$ -labeled triple resonance HN(CO)CACB and HNCACB spectra.....	110
Figure 47: α X I-domain residues assigned in HSQC.....	111
Figure 48. $^2\text{H}/^{13}\text{C}/^{15}\text{N}$ Triple resonance HNCACB and HN(CO)CACB plots and mapped split peaks...	113

LIST OF ABBREVIATIONS

6X - His tag - hexahistidine tag
Å- angstrom(s)
bp - base-pair(s)
cm - centimeter(s)
COSY- correlation spectroscopy
CV - column volume
Da - Dalton(s)
DGM - defined glutamate media
DMSO - dimethyl sulfoxide
DNA - deoxyribonucleic acid
EDTA - ethylenediaminetetraacetic acid
FPLC – fast performance liquid chromatography
HEPES - 2-[4-(2-hydroxyethyl) piperazine-1-yl] ethanesulfonic acid
HPLC - high performance liquid chromatography
HSQC - heteronuclear single quantum correlation spectroscopy
I-domain Inserted Domain
IPTG - Isopropyl-beta-D-thiogalactopyranoside
kb - kilobase(s)
kDa – kilodalton(s)
kV - kilovolt(s)
L- litre (s)
LB - Luria-Bertani
LC - liquid chromatography
Log10 - logarithmic transformation to the base 10
ln - natural logarithmic transformation
M - molar
Mb - mega-base(s)
mg - miligram(s)
MIDAS - metal ion dependent adhesion site
mL - mililiter(s)
mm - millimeter(s)
mM – millimolar

ng – nanogram
nm – nanometer
NMR - nuclear magnetic resonance
NOE - nuclear overhauser effect
OD600 - optical density at 600 nm
PAGE - polyacrylamide gel electrophoresis
PBS - phosphate buffered saline
PCR - polymerase chain reaction
PMSF - phenylmethylsulfonyl fluoride
ppm - parts per million
RMSD - root mean square deviation
ROESY - rotating-frame overhauser enhancement spectroscopy
SDS-PAGE - sodium dodecyl sulfate polyacrylamide gel electrophoresis
rpm - rotations per minute
SDS - sodium dodecyl sulfate
t - time
TCEP - 2-tris(carboxyethyl) phosphine hydrochloride
TRIS - tris(hydroxymethyl)aminomethane
 μg - microgram(s)
 μL - microliter(s)
 μM – micromolar
UV - ultra-violet

Amino acid	Three-letter abbreviation	One-letter abbreviation
Alanine	Ala	A
Arginine	Arg	R
Asparagine	Asn	N
Aspartic Acid	Asp	D
Cysteine	Cys	C
Glutamine	Gln	Q
Glutamic Acid	Glu	E
Glycine	Gly	G
Histidine	His	H
Isoleucine	Ile	I
Leucine	Leu	L
Lysine	Lys	K
Methionine	Met	M
Phenylalanine	Phe	F
Proline	Pro	P
Serine	Ser	S
Threonine	Thr	T
Tryptophan	Trp	W
Tyrosine	Tyr	Y
Valine	Val	V

Chapter I: Biochemical and Structural Characterization of α D I-domain of the Integrin α D β 2

1 INTRODUCTION

1.1 Cell surface receptors

The ability of cells to respond to environmental changes depends on the interaction between external stimuli and cell-associated receptors. This interaction causes the activation of the signal transduction pathways responsible for regulating cellular response to changes in conditions of the environment. Most often cells have intracellular receptors, but the cellular stimuli exerted by these receptors cannot cross the plasma membrane and, therefore, require the assistance of cell surface receptors to facilitate the interaction and response to changes in the external stimuli (Popovic and Wilson, 2018).

Cell surface receptors are transmembrane receptors or integral proteins embedded in the plasma membrane of the cell. They play an important role in maintaining communication between intracellular processes and various types of extracellular signals such as hormones, cytokines, growth factors, and neurotransmitters. Cell surface receptors usually perform the function of receiving and translating cues upon the binding of external ligand molecules and cytoplasmic adaptor proteins present on the surface of the cell membrane, resulting in immune system response. These receptors are therefore involved in life processes such as cell activation, cell adhesion, innate immunity, and signaling pathways (Cuatrecasas, 1974; Popovic and Wilson, 2018).

Cell surface receptors can be classified into the following types: ligand-gated ion channels, G-protein coupled receptors, receptor tyrosine kinases, toll-like receptors, and integrins (Figure 1). All these types of surface receptors play unique and critical roles in the three stages of signal transduction which include reception, transduction, and response.

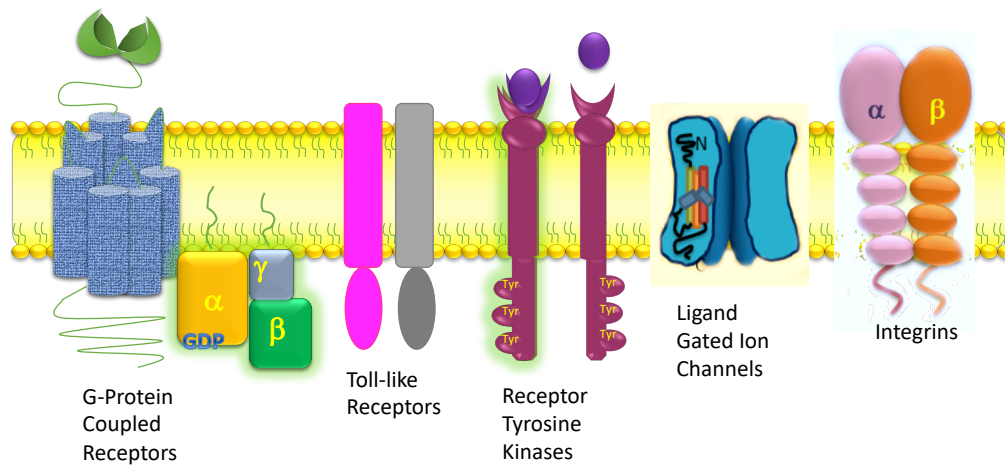


Figure 1: Schematic diagram of different types of cell surface receptors. (adapted from PicScience LLC © 2013)

1.2 Integrin superfamily

Integrins are α/β heterodimeric cell surface receptors that function to mediate cell–cell and cell–matrix interactions. They are also involved in essential processes such as cell migration, proliferation, differentiation, and bidirectional signal transduction (Abram and Lowell, 2009). Integrin–extracellular matrix (ECM) binding generates signals that are transmitted into the cell (**outside-in signaling**) while extracellular binding activity is regulated from the inside of the cell (**inside-out signaling**). This bidirectional signaling makes integrins unique cell surface receptors. Integrins have been shown to respond to both external and internal ligands through large changes in receptor conformation, which are strongly associated with integrin function. Thus, they can be

classified as allosteric receptors. Additionally, integrins are metalloproteins since cations play central roles in their physiological function (Hynes, 2002).

Integrins were first identified in metazoans, including some of the earliest-appearing animals such as sponges, cnidaria, corals, and jellyfish (Muller, 1997; Pancer et al., 1997). However, no integrin subunit has been detected in prokaryotes, plants, or fungi (Whittaker and Hynes, 2002). Integrin α and β subunits are present in invertebrates and vertebrates, while the latter have expansions of the integrin subunit set (Hynes, 2002).

In humans, there are eighteen α -subunits and eight β -subunits, which associate to form 24 non-covalently linked heterodimers. Each of the 24 integrins undertake a specific and nonredundant function despite the redundancy in ligand specificities, which is evident due to the diversity of integrin superfamily (Takada et al., 2007).

Nine of the α subunits contain an extra inserted α I-domain of approximately 220 amino acids. Studies have shown that the α I-domain is critical for integrin–ligand binding. These nine α I-domain-containing integrins—all of which are found only in chordates—include four collagen receptors ($\alpha 1$, $\alpha 2$, $\alpha 10$, and $\alpha 11$) and five leukocyte-specific receptors (αL , αM , αX , αD , and αE) (Figure 2) (Johnson and Chouhan, 2014). In addition to the collagen and leukocyte-specific receptors, vertebrates have the RGD receptors (αV , $\alpha 5$, $\alpha 8$, and αIIb), which recognizes the triple sequence, RGD, in molecules such as fibronectin, vitronectin, and laminin receptors ($\alpha 3$, $\alpha 6$, and $\alpha 7$) and mediates adhesion to basement laminins. Finally, a pair of related integrins ($\alpha 4$ and $\alpha 9$) recognizes both extracellular matrix proteins such as fibronectin and Ig-superfamily cell surface counterreceptors such as VCAM-1 (Hynes, 2002).

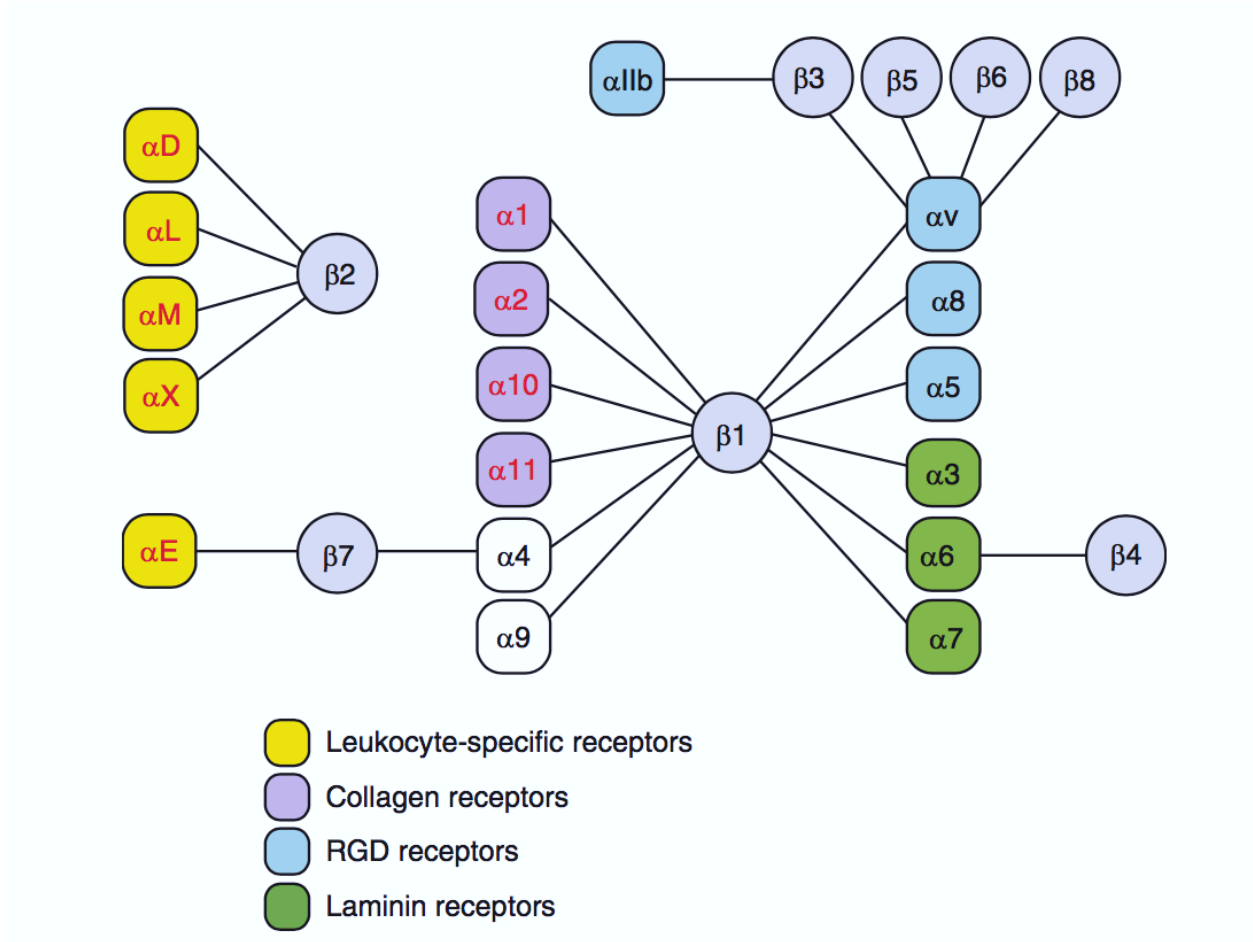


Figure 2: Classification of integrin family of heterodimers. Heterodimers of 18 types of α subunits and 8 types of β subunits combine to form 24 different integrins shown as connected by solid lines. Adapted from (LaFoya et al., 2018)

1.3. Leukocyte-specific integrins

Most leukocyte functions are dependent on members of the integrin family known as the leukocyte-specific receptors. Leukocytes circulate in the blood and body fluids before moving into tissues to become involved in counteracting invading pathogens or to participate in other immune functions (Arnaout, 2016). Leukocyte integrins, which include all four $\beta 2$ integrins together with $\alpha E\beta 7$ and $\alpha 4\beta 7$, play vital roles in the innate immune response to injuries and infections in the

body. These innate immune functions include interaction of phagocytic cells with the endothelium and extracellular matrix, ingestion of complement-opsonized pathogens, degranulation, cytokine production, and transmigration of leukocyte across the vasculature. Leukocyte integrins are also involved in lymphocyte proliferation, survival, and differentiation in adaptive immunity (Gahmberg et al., 2009; Hadley and Higgins, 2014). The functional state, density, and topography of leukocyte integrins are regulated by chemokines, cytokines, lipid signaling molecules, and “cross-talk” from other adhesion molecules (Harburger and Calderwood, 2009). The leukocyte-specific $\beta 2$ -integrins are the most abundant leukocyte integrins and consist of four closely related glycoproteins critically involved in leukocyte adhesion and migration during inflammatory immune responses. The $\beta 2$ -subunit was originally identified as CD18 and the α -subunit as CD11. It should be noted that the overproduction or deficiency of any member of the leukocyte $\beta 2$ integrins affect the normal innate or adaptive immune function, as exemplified in Leukocyte Adhesion Deficiency Type-I. This subfamily of $\beta 2$ -integrins include: $\alpha L\beta 2$ (LFA-1, CD11a/CD18), $\alpha M\beta 2$ (Mac-1, CD11b/CD18), $\alpha X\beta 2$ (CD11c/CD18), and $\alpha D\beta 2$ (CD11d/CD18) (Abram and Lowell, 2009; Arnaout, 2016; Hu et al., 2010).

1.4. Tissue and cellular distribution of leukocyte $\beta 2$ integrins

Expression of each $\beta 2$ integrin vary among the leukocyte subpopulations. That is, the expression profile on different leukocytes is unique for each member of the leukocyte $\beta 2$ integrin subfamily. For instance, $\alpha L\beta 2$ is expressed on all leukocytes but predominates on lymphocytes. Integrin $\alpha M\beta 2$ is the most abundant integrin on neutrophils, but also found on other myeloid cells like monocytes, macrophages, natural killer (NK) cells, fibrocytes, some mast cells, and lymphocytes like B cells, $CD8^+$ T cells, and on $\gamma\delta$ T cells (Arnaout, 1990; Gahmberg et al., 2009; Hynes, 2002). $\alpha X\beta 2$ is found mostly on other myeloid cells like monocytes, myeloid dendritic

cells, macrophages, and dendritic cells of the splenic white pulp and marginal zone. It is also expressed on NK cells and some subsets of T and B cells (Keizer et al., 1987a; Rosenkranz et al., 1998; Wagner et al., 2001). α D β 2, which is the major focus of my thesis, is the least studied member of this group of integrins and is expressed mainly on macrophages and eosinophils. Recent studies have shown that α D β 2 is significantly upregulated on inflammatory macrophages in both humans and mice (Miyazaki et al., 2014; Noti, 2002).

1.5. Ligands of leukocyte β 2 integrins

Leukocyte β 2 integrins bind to a diverse collection of large molecules or ligands. These ligands are either sub-endothelial matrix proteins or plasma proteins such as fibronectin, complement factors, and fibrinogen. Integrins α M β 2 (CR3), and α X β 2 (CR4) are known as complement receptors, while α D β 2 is so far identified as a fibrinogen receptor (Gahmberg et al., 1997; Hyun et al., 2009).

All four members of the leukocyte β 2 integrins have been shown to bind to at least one member of the intercellular adhesion molecule (ICAM) family and several other types of ligands. α L β 2 binds ICAMs 1–5, the neuronal glycoprotein telencephalin, and junctional adhesion molecule 1 (JAM1) (Ostermann et al., 2002; Tian et al., 1997). The human endothelial cell-specific molecule-1 (ESM-1) also binds directly to integrin α L β 2 and blocks ICAM-1 binding (Bechard et al., 2001). α M β 2 is very promiscuous and binds to over 40 reported ligands including iC3b, ICAMs 1– 4, fibrinogen, fibronectin, Factor X, JAM-3, and some proteases (Arnaout, 2016). α X β 2 binds vascular cell adhesion protein 1 (VCAM-1), iC3b, fibrinogen, and ICAMs 1 and 4 (Arnaout, 2016; Sadhu et al., 2007). α D β 2 binds to VCAM-1 and ICAM-3 (Van der Vieren et al., 1999). In addition to these ligands, α X β 2 and α D β 2 bind to several additional types of ligands including plasma

proteins, extracellular matrix components, and even carbohydrates (Arnaout, 2016; Yakubenko et al., 2008).

1.6. Integrin structure

The overall integrin structure consists of non-covalently associated α and β subunits containing α I and β I domains, with flexible linkers between them (Figure 3). These domain insertions contribute significantly to signal transmission (Luo and Springer, 2006). Each of the α and β subunits consist of a large extracellular multi-domain, a single membrane-spanning domain, and a short unstructured cytoplasmic tail linking integrins to the cytoskeleton. The β 4 subunit has a long fibronectin-type III cytoplasmic domain instead of a short unstructured cytoplasmic tail. Based on the primary structure, the α and β subunits contain about 1000 and 750 amino acids, respectively, although the sizes of different integrins slightly vary (Campbell and Humphries, 2011).

1.6.1. Extracellular domains

The crystal structures of α V β 3 and α X β 2 were the first complete extracellular domain or ectodomain of α I-less and α I-containing integrins successfully determined (Campbell and Humphries, 2011; Xie et al., 2010; Xiong et al., 2001). In α I-less integrins, the α -subunit consists of four extracellular domains: a seven-bladed β -propeller domain, thigh domain, and calf1 and calf2 domains (Figure 3) (Campbell and Humphries, 2011; Xiong et al., 2001; Zhu et al., 2008). α I-integrins has a fifth domain called the α I-domain, which shares the fold of the von Willebrand factor. The α I-domain is always inserted between blades 2 and 3 of the β -propeller domain and is the major ligand binding domain. The α I-domain recognizes the ligand directly when present and is thus very important for integrin activation and signaling (Diamond et al., 1993; Michishita et

al., 1993; Springer and Wang, 2004). The α I-domain consists of six β -sheets surrounded by seven amphipathic α -helices. Comparatively, the α I-domain shows intrinsic flexibility and conformational changes within the domain critical for regulating its binding affinity, unlike the other α subunit domains, which manifest relatively rigid structures (Springer and Wang, 2004). The integrin–ligand interactions are dependent on the presence of divalent cations, such as Mg^{2+} ion, which is coordinated by residues in MIDAS (metal-ion-dependent adhesion site) of the α I-domain. Upon ligand binding, the α I-domain transitions from a closed/low affinity to an open/high affinity state, which leads to the conformational arrangement in other parts of the α I-domain (Liddington and Ginsberg, 2002; Springer and Wang, 2004).

The N-terminal region of the integrin α -subunit contains seven repeats of about 60 amino acids, which fold into a seven-bladed β -propeller domain. The β -propeller domain directly participates in ligand recognition in the α I-less integrins (Springer, 1997; Springer and Wang, 2004; Xiong et al., 2001). The thigh and calf domains of the α -subunit have been shown to have similar, immunoglobulin (Ig)-like, β -sandwich folds. However, they consist of 140–170 residues with more β -strands than typical Ig-like domains (Campbell and Humphries, 2011; Xiong et al., 2001).

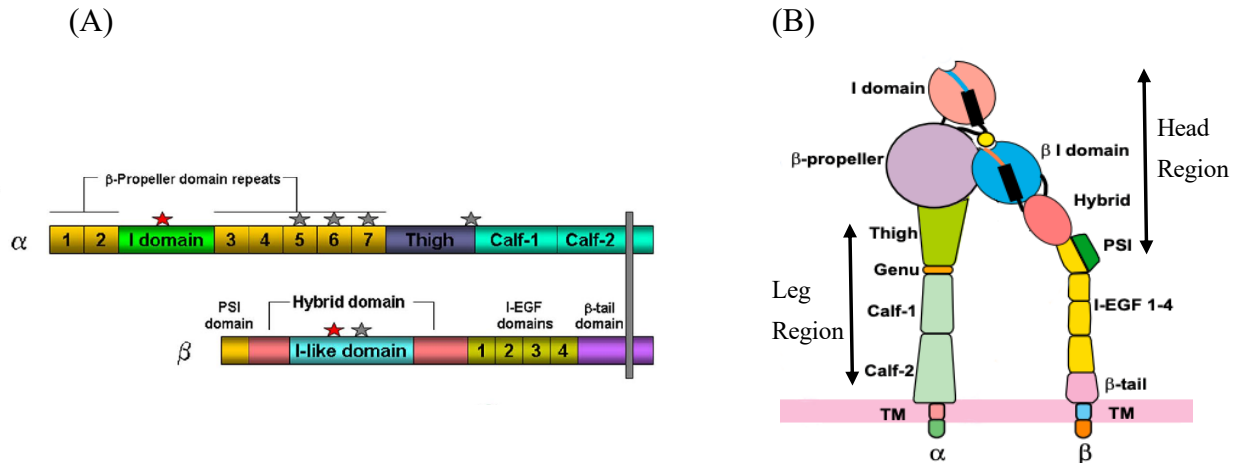


Figure 3: Integrin Structure and Domain Organization.

(A) Represent the integrins primary structure and domain organization, including Metal cation binding sites (Mg^{2+} as red star and Ca^{2+} as grey star). *Figure adapted from (Stefanidakis and Koivunen, 2006)*

(B) Represent schematic structure of the Integrin $\alpha\beta$ heterodimer shown in the extended open conformation. The α I-domain domain is inserted between β -propeller repeats 2 and 3 and is involved in ligand binding. The α I-domain, β -propeller, β I-domain, thigh, and hybrid domains forms the headpiece while the calf1 and calf2 domains of the α subunit and the EGF domains and the β -tail domain in the β subunit forms the leg region. *Figure is adapted from (Xie et al., 2010)*

The β -subunit consists of eight extracellular subdomains with flexible and complex linkers: a β I-domain, hybrid domain, a plexin-semaphorin-integrin (PSI) domain, four cysteine-rich epidermal growth factor (EGF)-like domains, and the β -tail domain (Figure 3B). The β I-domain is structurally homologous to the α I-domains. Thus, the β I-domain is responsible for ligand binding in the integrin heterodimers, which lack the α I-domain. In addition to the MIDAS region, the β I-domain also has the ADMIDAS (adjacent MIDAS), which binds an inhibitory Ca^{2+} ion. Structural studies of the α I β 3 also revealed a second Ca^{2+} binding site known as the synergistic metal ion binding site (SyMBS) (Xiao et al., 2004; Zhu et al., 2008). The orientation between the β I- and hybrid domains is critical in integrin conformational change.

The β -propeller and thigh domains of the α subunit and the β I-domain, together with PSI domains of the β -subunit form the head region of the integrin structure. Meanwhile, the Calf1 and Calf2 domains of the α -subunit and the EGF domains and the β -tail domain in the β subunit form the leg region (Figure 3A).

In both the β I-domain and the α I-domain, there are distinct closed and open conformational states that involve movement of the α 7 helix. For instance, in the α I-less integrins, the transition from the closed to an open state occurs when the β I α 7-helix moves downwards toward the hybrid domain (Xiao et al., 2004). Initially, same mechanism was also proposed for the the α I-domain, yet recent intact α Xb2 structures showed unexpected unwinding and reshaping of the α 7-helix. Nonetheless, metal ion dependent ligand-binding is linked to the structural motions of the α 7-helix. In the case of the α I domain, the α 7-helix acts like an “internal ligand” and binds to the β I-domain, an event I call in my thesis “crosstalk” because it involves also allosteric signal relay between two integrin subunits.

The crosstalk between the α I-domain and the β I-domain results in a 70° swing-out of the hybrid domain from the α subunit. This movement along with 70 Å shift of rigidly connected PSI domain located at knee region of β subunit, in turn, transitions integrins from a “closed” to an “open” conformation. Therefore, the connecting motion of the α 7 helix is an important activation step since it has been shown to induce a global conformation change of the intact integrin (Sen et al., 2018; Sen et al., 2013).

1.6.2. The membrane spanning or transmembrane helices

The transmembrane (TM) region of integrins consist of about 30 amino acid residues, which exist in either a homodimer or heterodimer form (Lau et al., 2008a; Lau et al., 2008b). Evidence

from current studies have shown that the heterodimeric form is favored when experiments or simulations are performed in the presence of ectodomains. These single transmembrane α -helices are formed from α -helical coiled coils and usually involved in intermolecular interactions when the integrin is in its resting state (Lietha and Izard, 2020). The results from experiments using EM, disulfide cross-linking, and FRET of labeled cytoplasmic tails have revealed that the association of α and β transmembrane segments of the integrin results in a resting receptor (Adair and Yeager, 2002; Kim et al., 2003; Luo et al., 2004; Wegener and Campbell, 2008). Several studies have confirmed the critical role played by the α/β transmembrane-cytoplasmic domains (TMCDs) in controlling the ability of integrins to bind extracellular ligands (inside-out signaling) and to cluster and form focal adhesions (outside-in signaling) (Yang et al., 2009).

1.6.3. The cytoplasmic tail

The cytoplasmic tails of integrins are typically unstructured and short, usually consisting of 10–70 amino acid residues. Although the cytoplasmic domain of integrins is smaller than the extracellular domains, they play an important role in integrin functions including regulating the integrin activation state (Hynes, 2002). Extensive research has shown that the α or β cytoplasmic tails are the sites of post-translational modifications, which serve as regulator mechanism for integrin interaction and linkage to adaptor proteins, kindlin and talin (Burrige and Chrzanowska-Wodnicka, 1996; Calderwood et al., 2002; Critchley et al., 1999; Zamir and Geiger, 2001). Thus, association/dissociation of integrin cytoplasmic domains with each other and other cytoplasmic proteins regulate the structure and function of the extracellular domains. To confirm that the α and β cytoplasmic domains can interact to control the activation states of integrins, the roles of α IIB and β 3 cytoplasmic domains of the platelet integrin, α IIB β 3, were investigated. These studies

revealed that α IIb cytoplasmic domain acts as a negative regulator of activation, where its deletion or restoration produces a constitutively active or inactive integrin, respectively (Burrige and Chrzanowska-Wodnicka, 1996; Calderwood et al., 2002; Critchley et al., 1999; Hynes, 2002).

1.7 Integrin activation and conformational changes

The ligand-binding activity of integrins is regulated by conformational changes (Takagi and Springer, 2002). Electron microscopy (EM) studies have revealed that integrins adopt three overall conformational states: bent with closed headpiece, extended with closed headpiece, and extended with an open headpiece as shown in Figure 4 (Nishida et al., 2006). The bent and extended closed conformations have been proposed as the low ligand affinity states. In contrast, the extended conformation with headpiece opening has been proposed as the high ligand affinity conformation (Springer and Dustin, 2012). However, I predict each integrin might have different ligand affinity; briefly, further affinity measurements of each conformational state are urgently needed. The extracellular domain extension allows the ligand binding headpiece to extend away from the cell surface, yielding in solvent exposure of interfaces between the headpiece and lower legs. The extended conformation with headpiece opening results in rearrangement in the MIDAS region of the β I-domain, causing the β I- α 7 helix piston to interact with the hybrid domain and leading to the swing-out of the hybrid domain away from the α -subunit (Luo et al., 2007; Takagi et al., 2002).

The uniqueness of integrin receptor family relative to other cell surface receptors is due to their ability in conveying a cell signaling bidirectionally. “Outside-in” signaling is the process where integrins mediate biochemical signals from extracellular matrix into the cells. Here, ligands bind to the low-affinity state of integrins, which induces conformational rearrangement to form an extended, open conformation (Takagi et al., 2002).

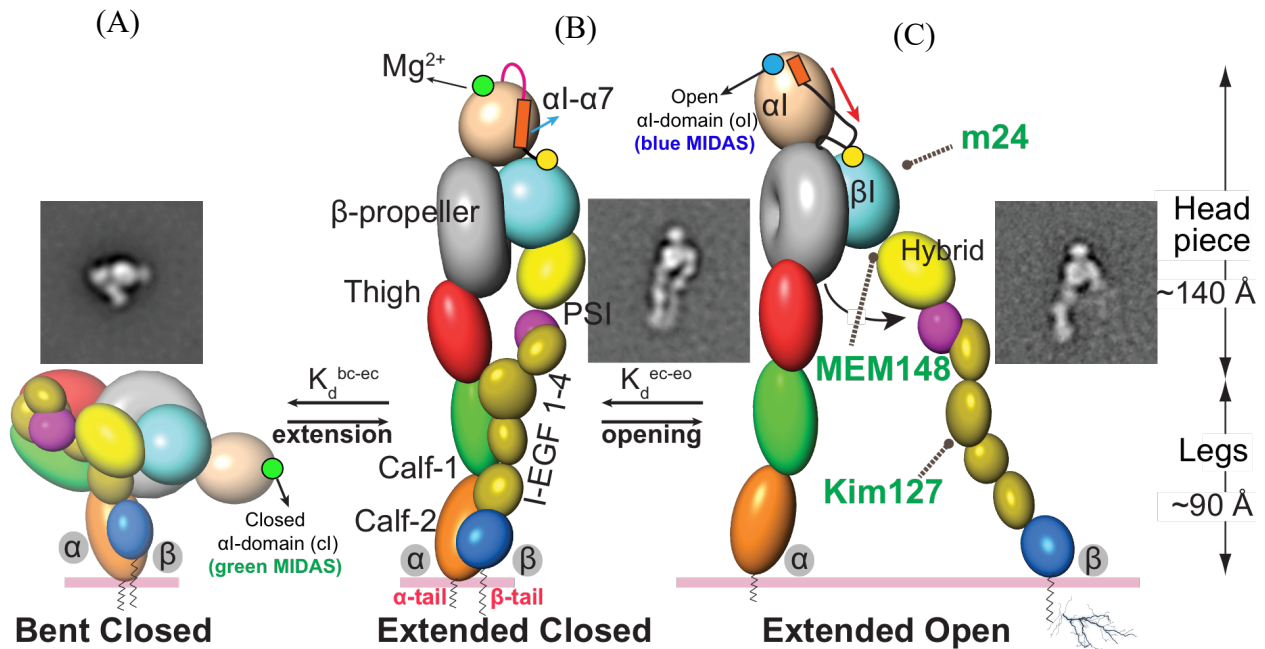


Figure 4: Schematic of different integrin conformations.

Three overall conformation of α I integrins. (A) the bent/closed and (B) extended/closed states have low affinity for an integrin ligand, but (C) the extended/open is the high affinity state.

Adapted from (Manandhar et al., 2017)

This ligand-stabilized extended, open conformation results in prolonged separation of the α - and β - subunit legs and transmembrane region such that the signal is transduced into the cytoplasmic domains. On the contrary, the process of “inside-out” signaling activates integrins from the low-affinity, bent state to the high-affinity, extended state via stimuli received from cell surface receptors like B-cell receptors and chemokine receptors, thereby relaying intracellular signals. Inside-out activation is considered to be initiated by separation of the two subunits at their cytoplasmic and transmembrane regions that result in the integrin extension and headpiece opening events—concerted two-steps that increase ligand affinity (Takagi et al., 2001; Vinogradova et al., 2002).

1.8.1 Integrin α D β 2: chromosomal location and expression

Integrin α D β 2 (CD11d/Cd18) is the most recently discovered member of the leukocyte integrin subfamily. The CD11d protein is encoded by the *ITGAD* gene, which is localized to chromosome 16, band p11(Wong et al., 1996). CD11d is mainly expressed on subsets of myelomonocytic cells and tissue-specialized cells, including macrophage foam cells and splenic red pulp macrophages (Noti, 2002). The strong expression of CD11d on macrophage foam cells and splenic red pulp macrophages indicate the possible role of this protein in the atherosclerotic process. The pattern of expression of integrin CD11d compared to the other β 2 integrins is very unique. For instance, the protein has been shown to be poorly expressed on circulating leukocytes. It has been reported to be expressed on human eosinophils suggesting that it may play a role in the adhesion of eosinophils to VCAM-1 during chronic inflammation (Grayson et al., 1998). Recent studies have also identified high CD11d expression on natural killer (NK) cells, B cells, and subsets of $\gamma\delta$ T cells (Siegers et al., 2017).

1.8.2. The roles/importance of α D β 2

The accumulation of macrophages during chronic inflammation development leads to the onset of numerous devastating diseases such as atherosclerosis, obesity, diabetes, and arthritis. α D β 2 has been shown to be an important inflammatory effector molecule in these pathologies. For instance, α D β 2 play vital roles in the migration and modulation of macrophage adhesiveness where downregulation of α D β 2 expression leads to monocyte migration while α D β 2 upregulation on differential macrophages may facilitate their retention at inflammation sites (Aziz et al., 2017; Yakubenko et al., 2008). Recent studies have demonstrated that a moderate density of α M β 2- and

α D β 2-transfected cells support migration, but high expression of any of these integrins significantly impedes cell motility.

In an experiment to determine white adipose tissue inflammation markers and characterize adiposity and metabolic phenotypes, CD11d mRNA was identified to be the most strongly elevated marker related to inflammation in rodent white adipose tissue and also in obese human white adipose tissue (Thomas et al., 2011).

Differential expression of α D β 2 play distinct roles in acute and chronic inflammatory responses and therefore implicated in various diseases. For instance, in *Plasmodium berghei*, α D β 2 is an important inflammatory effector molecule, which mediates experimental malaria-associated acute respiratory distress syndrome (MA-ARDS). Low levels of α D β 2 alters lung inflammation and acute lung injury in a mouse model of *P. berghei* induced MA-ARDS (de Azevedo-Quintanilha et al., 2016). Also, genetic deletion of α D in mice has been found to affect survival and systemic cytokine levels in mice infected with *P. berghei* without altering parasitemia or anemia (Miyazaki et al., 2008). Moreover, it has been reported that lack of α D β 2 expression in the thymus results in inaccurate T cell development, which then causes reduction in T-cell response to staphylococcal enterotoxins (SE) stimulation (Wu et al., 2004). However, overexpression of α D β 2 on macrophages promote macrophage retention in vascular lesions and is observed within atherosclerotic plaques (Aziz et al., 2017). It is also reported that α D β 2 expression is upregulated by oxidized low density lipoprotein and acetylated-low density lipoprotein (LDL and AcLDL) (Yakubenko et al., 2008).

The significant involvement of α D β 2 in the immune system, and related implications in multiple inflammatory induced diseases, show that this receptor is a promising target for anti-inflammatory therapies. It is very important to structurally and biochemically characterize integrin

α D in relation to receptor–ligand interactions, which can provide a better understanding of the α D integrin activation mechanism. Therefore, in this study, I seek to determine the crystal structure of the α DI-domain in the presence and absence of specific metal ions (M^{2+} -ions) and also characterized how these metals alter the α DI-domain-cation structure using biochemical and biophysical approaches.

1.8.3 Ligands of α D β 2

The ability of integrins to recognize and bind multiple ligands aids in integrin functional diversity. Several types of work on integrins have confirmed the α I-domain as the ligand-binding domain, which mediates the interaction of the α I integrins with their cognate ligands. Integrin α D β 2 is a multi-ligand macrophage receptor with recognition specificity similar to the major myeloid cell-specific integrins, α M β 2 and α X β 2 (Yakubenko et al., 2006). α D shows 60% and 58% amino acid identity to α M and α X respectively. This suggests a high extent of structural homology between the I-domains of α D, α M and α X. However, unlike α M β 2 and α X β 2, α D β 2 selectively binds ICAM-3 and VCAM-1 but does not appear to bind ICAM-1 (Van der Vieren et al., 1999). α D β 2 is reported to bind to different extracellular matrix proteins such as fibrinogen, fibronectin, and vitronectin (Yakubenko et al., 2008; Yakubenko et al., 2006). As stated earlier, integrins α X β 2, α M β 2, and α D β 2 have been shown to exhibit similar recognition specificity and also bind several proteins in the extracellular matrix (Arnaout, 2016; Yakubenko et al., 2008). This could indicate that α D β 2 might perform analogous functions to both α X β 2 and α M β 2. α M and α X I-domain are reported to differentially bind the complement fragment, iC3b, which makes them complement receptors (Gaither et al., 1987; Hinglais et al., 1989; Xu et al., 2017). In this thesis, the interaction of α D β 2 with iC3b was tested; we postulate that α D β 2 may also be a

complement receptor.

The complement system involving numerous plasma proteins is a crucial mechanism, which is activated directly by pathogen recognition or indirectly by pathogen-bound antibody. The resulting cascade of reactions builds an effective host defense against initial infections (Kumar and Cotran, 2007; Xu et al., 2017). The alternative pathway of complement activation, which is important in the innate immunity, involves a central role of a multidomain plasma protein called C3. An early triggered-enzyme cascade generates the protease-C3 convertase that cleaves C3 to yield C3a, a peptide mediator of inflammation, and C3b, the key molecule. which acts as an opsonin in the complement system by binding to pathogens. After sequential cleavage, degradation of the C3b forms the 173 kDa inactivated C3b (iC3b) fragment that links complement receptors and signaling (Papanastasiou et al., 2017; Ricklin et al., 2010). The interaction of iC3b and the complement receptor results in phagocytosis of the iC3b opsonized particles (Xu et al., 2017).

1.9. Divergence, structural features and conformational changes of the α I domains.

The α I-domain is an inserted (I) domain in the α -subunit between two loops on the upper surface of the β -propeller (Figure 5). Evolutional studies have shown that, the β I-domain has always been an integral part of all integrins but the α I-domain diverged relatively late in early chordates. The appearance of integrins with α I-domain in chordates may have contributed to the extensive changes in body plan and systemic development of the early chordates (Johnson and Chouhan, 2014). For these chordates, this inserted domain moved the integrin external ligand binding site away from the β -propeller-- β I-domain interfacial cleft (Chouhan et al., 2014; Johnson and Chouhan, 2014; Lee et al., 1995).

In humans, nine of the eighteen α subunits have the α I-domain present. Orthologues extend across several species including mammals, birds, reptiles, amphibians and bony fish (Johnson and Chouhan, 2014). As indicated in section 1.6.1, in the α I-domain containing integrins, the α I-domain plays a central role in ligand binding and integrin activation while the β I-domain and the β -propeller play regulatory roles (McCleverty and Liddington, 2003; Park et al., 2020).

In my doctoral training, I studied the isolated α I-domain, which brings critical questions of whether it is physiologically relevant to study the isolated/recombinantly expressed α I-domain. For instance, isolated, surface-expressed leukocyte α I-domains fused to an artificial transmembrane helix have regularly been used for adhesion and functional studies and have been shown to undergo structural changes (Lu et al., 2001a; Shimaoka et al., 2001; Shimaoka et al., 2002; Shimaoka et al., 2003b). The studies on the development of small molecule integrin antagonists have been heavily focused on α I-domains (not intact integrin). This is because the α I-domain is the key molecular switch in integrin activation. Recent studies performed on recombinant α I-domains isolated from the intact integrin show that these inserted I domains respond allosterically. It has also been established that human leukocyte integrin α I-domains are glycan-free and have no post-translational modifications (Bajic et al., 2013; Sen and Springer, 2016). Structural and functional studies on α I-domains have therefore been widely accepted to represent what is occurring on the intact integrins, and isolated α I-domains have been heavily used as a platform for drug screening (Kollmann et al., 2014; Shimaoka et al., 2003a).

donates an aspartate residue (Luo et al., 2007). Mutating any of these residues blocks ligand-binding (Gullberg, 2014). Structural studies of α I-domains in the presence and absence of ligand, and with mutations that stabilize distinct affinity states, have revealed three global conformations termed closed, intermediate, and open states (Luo et al., 2007). Subsequent studies have also suggested that the closed and intermediate states represent the inactive α I-domain while the open state represent the active α I-domain (Shimaoka et al., 2003b; Vorup-Jensen et al., 2003).

As stated above, MIDAS residues and several water molecules contribute oxygen atoms to the primary and secondary coordination spheres that surround the Mg^{2+} at the MIDAS. In the closed state of the α I-domain, the threonine residue in the primary coordination sphere moves to the secondary coordination sphere while one of the aspartic acid residues moves from the secondary to the primary sphere (Figure 6A). This backbone and side chain rearrangements are accompanied by a 2.3 Å “sideways” movement of the MIDAS M^{+2} -ion away from the threonine towards the aspartic acid residue on the opposite side of the coordination sphere (Luo et al., 2007).

In the open state, the two serine residues and the threonine residue are located in the primary coordination sphere while the two aspartic acid residues are located in the secondary coordination sphere (Figure 6B). The binding of a ligand to the α I-domain MIDAS causes the rearrangement of the metal coordinating residues at the MIDAS. This therefore allows the invariant glutamic acid residue to bind to the coordinated metal ion at MIDAS of β I domain due to unwinding of the α I α 7-helix (Alonso et al., 2002; McCleverty and Liddington, 2003).

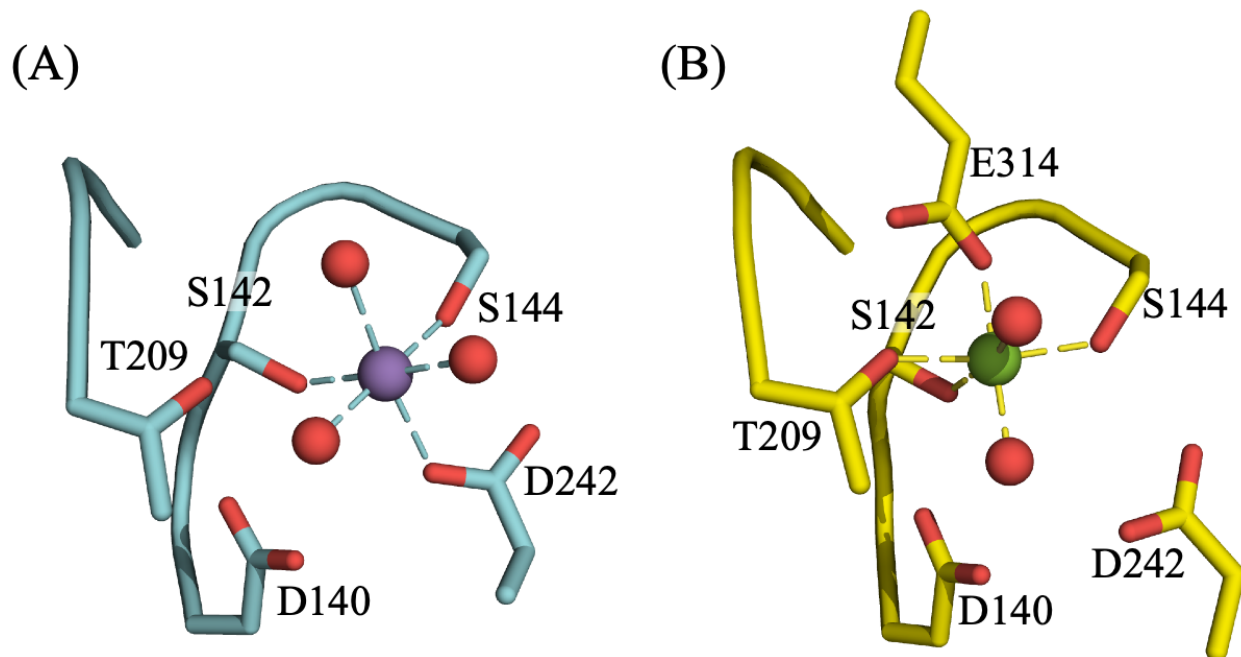


Figure 6. Structural rearrangement of the α M I domain MIDAS. (A) Structure of the closed α M I-domain MIDAS. (B) Structure of the open α I domain MIDAS. Glu-314 from a neighboring α M I-domain coordinates with the MIDAS magnesium. Purple and green spheres are Mn^{2+} and Mg^{2+} ions, respectively, and red spheres are coordinating water-molecule oxygens. [From PDB ID codes 1JLM and 1IDO] Adapted from (Luo *et al.*, 2007).

The transition from closed to open conformation is allosterically coupled to a large piston-like downward motion of the α I α 7-helix at the opposite pole of the domain (McCleverty and Liddington, 2003). Several studies on the isolated α I-domains showed that the α I α 7-helix moves as a unit 10 Å in the C-terminal, an axial direction between the closed and open conformations. This transition between closed and open conformations, which in turn regulates integrin ligand binding is very important for the whole or intact integrin protein (Alonso *et al.*, 2002; Chen *et al.*, 2010b; Huth *et al.*, 2000; Jin *et al.*, 2004).

1.9.2 Cation binding to integrins

Ligand-binding to integrins requires the presence of metal ions (M^{2+} -ions) bound to the MIDAS located in both the αI and βI domains. It has been reported that the metal ions (M^{2+} -ions) such as Ca^{2+} , Mg^{2+} , and Mn^{2+} are not only a pre-requisite of binding of integrin ligands but can also influence the integrin activation state and integrin-mediated cell adhesion including enhancement, suppression and modification of ligand binding activity (Altieri, 1991; Dransfield and Hogg, 1989; Griggs et al., 1998; Hall and Slack, 2019). For example, Mn^{2+} has been established to induce conformational changes to the integrins $\alpha L\beta 2$ and $\alpha M\beta 2$ whereby activate the adhesion between integrins and their cognate ligands (Altieri, 1991; Dransfield and Hogg, 1989). However, Ca^{2+} -binding has been shown to inhibit $\alpha L\beta 2$ mediated adhesion to ligands but not $\alpha M\beta 2$. These results suggest that Mn^{2+} and Ca^{2+} complexes of integrin αI -domain may represent high and low-affinity ligand binding states respectively (Griggs et al., 1998). The X-ray crystal structure of Cd^{2+} bound αM I-domain has also been determined (Baldwin et al., 1998).

There are still many questions on the role and effects of metal ions to the αI -domain: how do specific cations contribute to conformational changes in leukocyte integrin activation, and which metals induce the active conformation of the αI -domain? Can the binding of these M^{2+} -ions help reveal limitedly visited conformational states of integrins? How does binding of different metal ions affect the rearrangement of the MIDAS residues of the integrin αI -domain? This study seeks to answer some of these questions by implementing a hybrid approach to define metal-binding to our model protein, the αD I-domain. I believe this research may help understand the interrelationship between thermodynamics and biochemical properties of the MIDAS-metal cation assembly. Understanding integrin structure-function relationship will also provide more insight

for understanding of the design and development of novel anti-inflammatory inhibitors for curtailing autoimmune pathologies (Manandhar et al., 2017).

In this dissertation, we determined the crystal structure of the α D I-domain in the presence of M^{2+} -ions; Ca^{2+} , Mn^{2+} , Mg^{2+} , Cd^{2+} , Zn^{2+} , and Co^{2+} . We examined the characteristics of these cation binding to the structure of the α D I-domain. We also demonstrated the effect of each divalent cation (Ca^{2+} , Mn^{2+} , Mg^{2+} , Cd^{2+} , Zn^{2+} , and Co^{2+}) on the stability, thermodynamics and conformation of the α D I-domain. Additionally, we showed in the presence of Mg^{2+} , the α D β 2 binds to the complement protein iC3b suggesting α D β 2 to be part of the complement system.

2. MATERIALS AND EXPERIMENTAL PROCEDURES

All chemicals used in this work were of molecular biology grade, if not stated otherwise. Kits and equipment were used according to the manufacturer's manuals or with modified protocols as described in this work. All the buffers and precipitants and solutions used in this work have been described in the appendix. The cell assay experiments of this work were performed by Zeinab Moussa.

2.1 The α D I-domain expression

The recombinant integrin α D I-domain gene used for this study corresponds to amino acid residues Gly128 to Val318 of the intact CD11d protein. This CD11d gene fragment was subcloned into the pET28a expression vector with an N-terminal 6His affinity tag and transformed into *Escherichia coli* BL21(DE3) Rosetta cells. All the Luria–Bertani (LB) media, terrific broth media, and LB-agar plates contained 50 μ g/mL of kanamycin and 100 μ g/mL chloramphenicol. The terrific broth was prepared with tryptone (12 g/L), yeast extract (24 g/L), glycerol (4 ml/L), 0.17 M KH_2PO_4 and 0.72 M K_2HPO_4 . 50 μ L of BL21 (DE3) *E. coli* competent cells were thawed on ice. 2 μ l of pET28a-*CD11d* plasmid DNA was added to the cells and incubated on ice for 30 minutes. The mixture was heat shocked for 60 s at 42 °C and left on ice for 2 min. 300 μ l of LB media was added into the mixture and the tube was shaken at 250 rpm for 60 min at 37 °C. 100 μ L of the mixture was spread onto a LB-agar plate and incubated overnight at 37 °C. A single colony of the transformed BL21 (DE3) cells containing pET28a-*CD11d* was used to inoculate 5 mL starter culture of LB media. The culture was incubated overnight at 37 °C with shaking at 250 rpm. The starter culture was used to inoculate 1 L terrific broth and grown at 37 °C with vigorous shaking until OD_{600} nm of 0.5–0.7 was reached. The temperature of the cells was reduced to 15 °C, then protein production was induced by adding isopropyl-1-thio- β -D-galactopyranoside

(IPTG) to a final concentration of 100 μ M. The cells were then incubated overnight (14–16 h) with vigorous shaking at 15 °C. Cell pellets were then harvested by centrifugation at 3500 rpm for 30 min. The cell pellets were stored at –80 °C.

2.2 Purification of integrin α D I-domain

The cell pellets were resuspended in lysis buffer (20 mM Tris-HCl, pH 8.0, 200 mM NaCl and 10% glycerol) and lysed by passing the cell suspension through a Avestin Emulsiflex C3 homogenizer at 15,000 psi (3–5 times). The homogenate was incubated in the cold room (4 °C) with gentle rocking for 20 min after adding 1X Phenylmethanesulfonylfluoride (PMSF) and 1mM DNase, followed by centrifugation at 10,000 rpm in polycarbonate centrifuge tubes for 45 min at 4 °C.

The resulting supernatant was filtered and loaded onto a Ni-Sepharose HisTrap HP column (GE-Healthcare). After washing the column with the binding buffer (20 mM Tris, pH 8.0, 40 mM imidazole, 300 mM NaCl, 10% glycerol), the proteins retained by the column was eluted with a linear gradient of 0-500 mM imidazole employing the fast-performance liquid chromatography (FPLC). Eluted fractions were analyzed for the presence and purity of the α D I-domain protein using SDS-PAGE. The gel was stained with Coomassie Brilliant blue R-250 and destained for 2–4 h. Fractions, which gave clear and intense bands at 24 kDa on the SDS-Gel were pooled, concentrated, and further purified on a Superdex 75 (S75) gel filtration column (Pharmacia) with 20 mM Tris, pH 7.4, 150 mM NaCl as elution buffer. The HiLoad 16/60 S75 prep grade column used for all the size exclusion chromatography was equilibrated with 120 mL of the same elution buffer. The eluted fractions obtained from this purification process were also analyzed by SDS-PAGE. Again, fractions from the size exclusion purification, which gave clear bands at 24 kDa were pooled, concentrated, and digested overnight with human rhinovirus 3C protease at a ratio of

1:30 protease: protein for 16 h at 4 °C to separate the hexameric Histidine affinity tag and the α D I-domain protein. After overnight digestion, the protein mixture was passed through the HisTrap column to remove the α D I-domain protein of interest as a flow through. Finally, the flow through was concentrated and then loaded onto a Superdex-75 gel filtration column in 20 mM Tris, pH 7.4, 150 mM NaCl. The purified protein was then concentrated for crystallization using an Amicon ultra centrifugal filter unit with a 10 K molecular mass cutoff (Amicon^R). A Coomassie blue stained SDS-PAGE was used to evaluate the final purity of the α D I-domain with a total yield 5–10 mg/L of cell culture and about 95% purity. The protein concentration was measured by its absorbance at 280 nm and using the extinction coefficient of 7450 M⁻¹·cm⁻¹. All SEC buffers were prepared with water that further purified using Chelex-100 resin (Bio-Rad catalog#1421253), filtered at 0.22 μ M, and then thoroughly degassed.

2.3 Crystallization

2.3.1 Screening

The main crystallization method employed was the vapor diffusion technique including both the hanging drop and sitting drop vapor diffusion (Figure 7A). The initial crystallization screening was done in the ARI Intelli-plate 96-well plates using a Phoenix crystallization robot (Art Robbins Instruments). Hampton Research screens HR2-130, HR2-144 and ProPlex MD1-42 (Appendix Tables A1, A2 and A3) were used as the initial screens for crystallization using the sitting drop vapor diffusion method. The reservoir was filled with 50 μ L of the screening reagents while the crystallization drop was mixed with 0.4 μ L of protein and 0.4 μ L of screening reagents. The ARI Intelli-plates used has three wells in each of the 96 compartments of the plate preset for the crystallization drop. This setup allows three unique protein solutions/concentrations to be screened simultaneously. In this experiment, a control solution (only buffer) and two different

concentrations (<30 mg/ml and >50 mg/ml) of the α D I-domain were used. The plate was sealed with a crystal-clear package sealing (Manco. Inc.) and stored at 4 °C or the ambient temperature. The crystallization drops were examined under a microscope (10–100X magnification) immediately after setting up the screen and each day for the first week.

2.3.2 Optimization

The conditions that produced any form of crystals, including microcrystals, needles (1D Growth) and plates (2D Growth), from the Hampton and ProPlex screens were further optimized. Optimization involved varying temperature, protein concentration, concentrations of the screening reagents, and addition of metal ions (M^{2+}) in screening reagents. Here, the 24 well plates (Hampton Research) and the hanging drop diffusion method were used. The reservoir was filled with 1000 μ L of the newly prepared screening solution and the crystallization drop contained a mixture of equal volumes (2 μ L) of the purified α D I-domain (30 mg/mL to 60 mg/mL) and the reservoir solution. The crystallization drop was placed on a 22 mm siliconized thick glass square cover slides (Hampton Research) and placed over the reservoir with the drop facing downwards (Figure 7A). Since each cover slide can accommodate up to four smaller drops, protein concentrations were varied for one reservoir. In all cases a control drop containing reservoir solution and the buffer was included. The plates were prepared and stored at 4 °C after careful examination under the microscope. How the protein reacts upon addition of the precipitants as well as all the conditions and changes in the crystallization drops were recorded. The following crystallization conditions, which produced three-dimensional single crystals were selected for the final optimization (Table A4). The crystallization solutions optimized include: Polyethylene glycol, PEG 4000 (10-18% wt/vol), 0.1 M sodium cacodylate; 0.1 M Tris, pH 8.5, 10-15% PEG 3350; 0.1M HEPES, pH 7.5, 12-25% PEG 3350; and 1.5 M malic acid. It took 7-14 days to grow the α D I-domain crystals to

their final size. Single crystals were then picked and cryoprotected in a reservoir solution supplemented with 30% glycerol in 5% glycerol increments as cryoprotectant before liquid nitrogen vitrification. Some of the crystals were cryoprotected using 30% PEG 3350 in the increment of 5%.

Co-crystallization was done by including 1 mM or 5 mM MgCl_2 or other M^{2+} -ions (Zn^{2+} , Mn^{2+} , Cd^{2+} , Co^{2+} , Ca^{2+} , Ni^{2+} , and Cu^{2+}) in the crystallization reagent and or crystallization drop. The crystallization reagents for the co-crystallization contained 0.1 M HEPES, pH 7.5, 12-25% PEG 3350 and a metal-ion (M^{2+}). After 7-14 days single crystals were picked and cryoprotected in a reservoir solution containing 25% PEG3350 in the increment of 5% and 0.5 mM or 1 mM M^{2+} before liquid nitrogen vitrification.

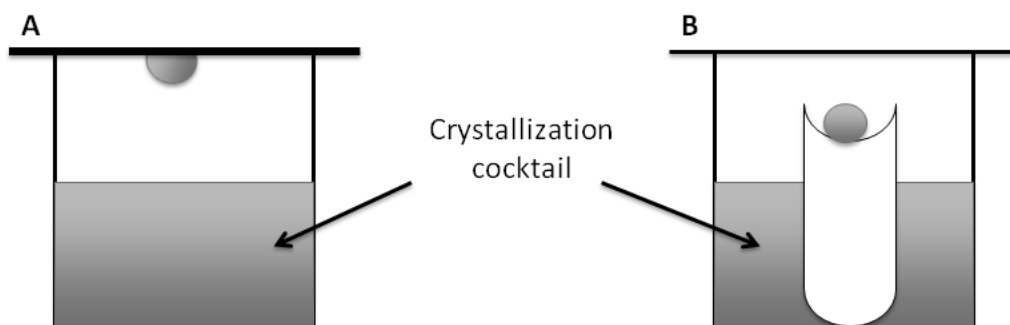


Figure 7: Illustration of vapor diffusion methods of crystallization. The crystallization drops consist of the crystallization cocktail and the same volume of the protein solution. (A): The crystallization drops hang over the reservoir on a siliconized cover glass. (B): The crystallization drop "sits" on a platform.

2.4 X-ray diffraction and structural determination

2.4.1 X-ray diffraction data collection

The crystals were prepared for X-ray diffraction by shock freezing them in liquid nitrogen immediately after they were individually scooped out of the crystallization plates using a loop. Diffraction data was collected at a wavelength of 0.97 Å or at the fluorescence peak of the metal ions on the APS beamline 31-ID-D of the Advanced Photon Source (APS), Argonne National Laboratory, Lemont, Illinois. The X-ray diffraction data was collected by oscillating the mounted crystal for a 0.2 degree during one exposure and then proceeding to the next part of the reciprocal sphere until all the required data were acquired.

2.4.2 Indexing and integration of X-Ray data

The X-ray diffraction data collected at APS beamline ID-23 were preliminary processed with iMosflm (Battye et al., 2011) program to assess the quality of the crystal while data were still recorded. Other programs were used to either confirm the quality of each crystal diffraction data collected. The XDS program (Kabsch, 1993) together with the XDSCUI (Diederichs, 2010; Kabsch, 2010) package were used for indexing, integrating, and scaling of the diffraction data. The POINTLESS program from the CCP4 package (Project, 1994) was used to identify space group possibilities from unmerged data. The XDSCONV program, which is natively part of the XDSCUI package, was used to generate the mtz files for structure determination.

2.4.3 Structure determination

In protein crystallography, the so called “phase problem” occurs when only the amplitude of the diffraction pattern spots are measured but the information of their phases is lost in a diffraction experiment. To be able to reconstruct the electron density distribution in the unit cell, it is very

important to obtain the phases. Several techniques available for phase determination includes: Direct methods, Multiple Isomorphous Replacement (MIR), Multiple Anomalous Dispersion (MAD), and Molecular Replacement (MR) (Cowtan, 2001; Ilari and Savino, 2008). The easiest approach in solving the phase problem is the molecular replacement method when the protein under study is similar to another protein whose structure is already known. Based on amino acid sequence alignments, integrin α D I-domain had about 58% amino acid sequence identity with the integrin α X I-domain. Thus, the α D I-domain protein structure was solved by PHASER molecular replacement (McCoy, 2007) using the α X α I-domain as template (Sen et al., 2013).

2.4.4 Model building and refinement

The molecular replacement solution was refined against the diffraction data in *PHENIX* (Adams et al., 2010), while using *Coot* (Emsley and Cowtan, 2004) to fit the protein residues in the electron density map. Prior to refinement, the reflections were randomly divided into a test set or ($R_{\text{free}} \sim 5\%$) and a working set ($R_{\text{work}} \sim 95\%$). An initial model was obtained by refining each domain as a rigid body followed by torsion angle simulated annealing. Other initial refinement strategies used included: both reciprocal and real space, TLS parameters, and individual B-factors. Non-crystallographic symmetry restraints (NCS-restraints) were not included in the refinement of the crystal structure obtained from PEG 3350 precipitant because there is only one molecule per asymmetric unit. Metal ion coordination and ligand restraints were generated using *ReadySet* implemented in *PHENIX*, which uses electronic Ligand Builder and Optimization Workbench (*eLBOW*) to generate ligand restraints (Moriarty et al., 2009). Water molecules were added automatically and manually to the electron density map during the rebuilding process with *Coot*. The rebuilding and refinement processes were repeated several times (Chen et al., 2010a; Davis et al., 2004).

2.4.5 Structure validation and figure preparation

The validation of the refined protein structure was performed with MolProbity (Davis et al., 2004) and the final refinement statistics table was compiled in *PHENIX*. The TopDraw (Bond, 2003) program was used to obtain the topographical representation of the α D I-domain polypeptide folding while the rest of the protein figures were prepared with the PYMOL program (DeLano, 2002). Secondary structure annotation was based on the DSSP program output (Kabsch and Sander, 1983).

2.5 Differential Scanning Fluorimetry (DSF)

The binding affinity and stability effect of Mg^{2+} , Mn^{2+} , Ca^{2+} , Cd^{2+} , Co^{2+} , and Zn^{2+} , cations to the α D I-domain was determined by performing a thermal shift assay using differential scanning fluorimetry (DSF). Using a 96-well Polymerase Chain Reaction (PCR) plate, a fixed volume (10 μ L) of a master reaction mix including the α D I-domain, a buffer (20 mM HEPES, pH 7.4, 150 mM NaCl) and 20x SYPRO orange dye for fluorescence detection was added to each well. The buffer used for the last step of size exclusion purification and the rest of the experiments was prepared in metal-free water. Different stock concentrations of the M^{2+} -ions (Mg^{2+} , Mn^{2+} , Ca^{2+} , Cd^{2+} , Co^{2+} , and Zn^{2+}) were prepared, and subsequently added to each well. Each well contained 5 μ g of protein. For each cation experiment, four replicates were performed. The reaction mixture with the α D I-domain, SYPRO orange dye and buffer in the absence of cations was the positive control of the experiment. Negative control included a protein mix without SYPRO orange dye.

The fluorescence was measured at regular intervals with the temperature gradient of 0.1 $^{\circ}$ C per 15 s over a temperature range spanning from 15 $^{\circ}$ C to 95 $^{\circ}$ C in the CFX96 real-time PCR instrument (Bio-Rad). Furthermore, to ensure that the ionic strength did not affect the melting

temperature of the protein, the thermal unfolding of the α X I-domain was monitored at increasing concentrations of NaCl.

2.6 Isothermal Titration Calorimetry (ITC)

The cell filling syringe for MircoCal ITC (Hamilton) and the Micro Calorimeter PEAQ-ITC (Malvern Panalytical Inc.) were used for this experiment. The thermodynamic parameters for the binding of these M^{2+} -ions (Mg^{2+} , Mn^{2+} , Ca^{2+} , and Zn^{2+}) to the α D I-domain were determined. 100 μ M α D I-domain was loaded into the Micro Calorimeter PEAQ-ITC with a cell volume of 200 μ L in a buffer containing 20 mM Tris or HEPES, 150 mM NaCl, pH 7.4. For each α D I-domain put in the cell, about 75 μ L of individual M^{2+} -ions at different concentrations prepared in identical buffer were injected for 19 or 25 cycles in initial volume of 0.5 μ L and 1.0 μ L in the rest of the titration with continuous stirring of 750 rpm at 25 °C (Table 1). Binding enthalpy (ΔH^0) (kcal/mol) versus the molar ratio of cation to the α D I-domain was generated from each injection. The thermodynamic parameters including M^{2+} affinities and energetics were then calculated. All buffers were prepared with CHELEX-100 purified water, filtered at 0.22 μ m, and then thoroughly degassed.

Table 1. Concentration of syringe and cell contents in each α D I-domain- M^{2+} -ion titration

Metal	[M^{2+}] in syringe (mM)	[α D] in cell (μ M)
Mg^{2+}	7.5	100
Mn^{2+}	1.25	120
Ca^{2+}	20.0	100
Zn^{2+}	7.5	120

2.7 E-IgM-iC3b Rosetting assay

Sheep erythrocytes were sensitized with IgM(E-IgM) and with C5-deficient human complement (E-IgM-iC3b) as previously established (Bilsland et al., 1994). Briefly, sheep erythrocytes (Colorado Serum Company) were washed once with PBS (pH7.4), then incubated with anti-Forsman IgM monoclonal antibody (M1/87) for 1 h at room temperature. Complex was incubated with C5- deficient human serum at 37 °C for 1 h. E-IgM-iC3b and E-IgM as control were assessed for binding to α D β 2 HEK293T transfectants. After 48 h of transfection, cells in a 24-well plate were washed once with HBS and incubated with 50 μ L of 10 μ g/mL of used IgG, 1 mM Mn²⁺/0.2 mM Ca²⁺ and 1 mM Mg²⁺/1 mM Ca²⁺ for 30 min at room temperature. E-IgM-iC3b (250 μ L) was then added and plate was incubated for 1.5 h at 37 °C. Unbound erythrocytes were removed by gentle washing (3x) with PBS. Rosettes (>10 erythrocytes/HEK293T cell) were scored by microscopy.

2.8 Epitope exposure

To probe the conformation of α D β 2 on cell surface, 293T α D β 2 transfectants were incubated with conformation specific monoclonal antibodies (KIM 127, MEM148, M24), 500 ng/million cell on ice for 30 min followed by 30 min incubation with secondary FITC conjugated antibody on ice. Mean fluorescence intensity (MFI) was measured in the presence of 1 mM MgCl₂/ CaCl₂ or 1 mM MnCl₂ and normalized to the level of expression of the integrin on cell surface as detected by CBR-LFA1/7 mAb.

2.9 Flat bottom adhesion assay

Fibrinogen was used to coat flat-bottom 96-well plates at 10 μ g/mL for HEK 293T α D β 2 transfectants. After coating, wells were blocked with 1% BSA. Cells were labelled with 2',7'-bis-

(2-carboxyethyl)-5-(and-6)-carboxyfluorescein, acetoxymethyl ester (BCECF-AM) (4 $\mu\text{g}/\text{mL}$) in L15 media, extensively washed, resuspended in HBS (20 mM HEPES pH 7.4, 140 mM NaCl, 5 mM KCl, 5.5 mM glucose, 0.5% BSA) on ice with increasing concentration of Simvastatin to 2×10^6 cells/mL, and aliquoted (50 μL) into coated plates. Activation of HEK293 $\alpha\text{D}\beta 2$ transfectants was by incubating the plate in presence of Mn^{2+} for 1 h at 37°C . Unbound cells were washed off manually with HBS using a multichannel pipette, until binding to BSA-coated surfaces of stimulated cells reached 5% of input. Cells activated by Mn^{2+} were washed with HBS supplemented with 1 mM Mn^{2+} . The percentage of adherent cells was calculated from fluorescence measurements before and after washes using Biotek plate reader; (Ex 485 nm/Em 538 nm). Adhesion to BSA-coated control wells was subtracted from adhesion to Fibrinogen coated wells. The experiment was repeated for different M^{2+} -ions (Mg^{2+} , Co^{2+} , Zn^{2+} , Ni^{2+} , Cd^{2+} , and Cu^{2+}).

3. RESULTS

The recombinant integrin α D I-domain is a 237 amino acid protein with a theoretical pI of 6.90 and 26.04 kDa molecular weight when uncleaved. Upon cleavage of the N-terminal tags, the protein is 195 amino acids long with a theoretical pI of 6.65 and molecular weight of 21.49 kDa. The protein does not contain any tryptophan residues. The computed extinction coefficient is $7450 \text{ M}^{-1} \text{ cm}^{-1}$ at 280 nm.

3.1 Expression and purification of the α D I-domain

To determine the atomic structure and properties of the α DI-domain, we first had to find best conditions for the expression and purification of this protein. Expression of the N-6His α D I-domain was started from freshly transformed *E. coli* cells. When transformed into BL21 (DE3) *E. coli* cells, modified pet28a α DI-domain plasmid expressed soluble proteins at 15 °C with induction (100 μ M IPTG) in terrific broth media.

After the affinity purification (Figure 8A), the proteins were analyzed by SDS-PAGE, which confirmed the α D I-domain with an N-terminal hexameric Histag at around 25 kDa (Figure 8B). Fractions which gave clear intense bands at 25 kDa on the SDS-Gel (Figure 8B) were pooled, concentrated, and further purified on a HiLoad superdex 75 (s75) gel filtration column (Figure 9A, B).

Further purification with gel filtration confirmed the successful cleavage of the N-terminal 6His affinity tag from the α D I-domain (Figure 10A). The α D I-domain was largely monomeric by gel filtration. The purified protein was determined to be at least 99% pure (Figure 10B)

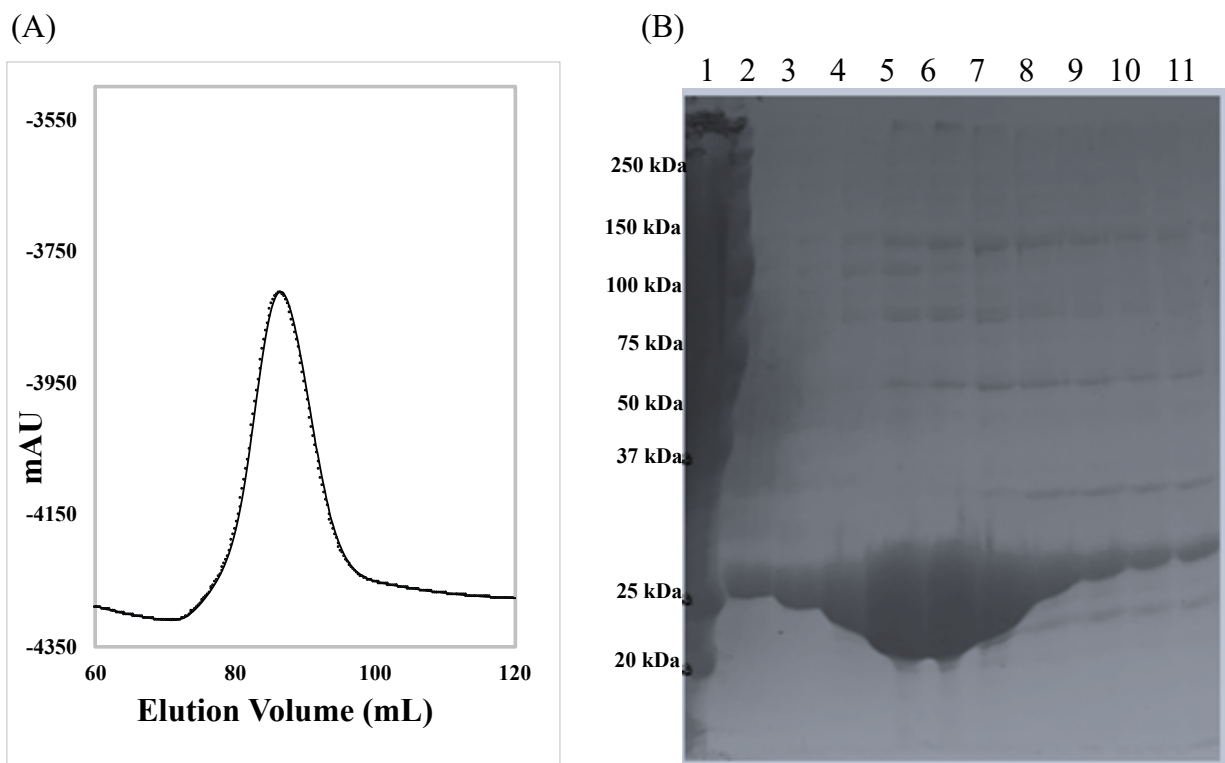


Figure 8: FPLC purification of the α D I-domain protein by affinity chromatography and the SDS-PAGE analysis. (A) shows the FPLC purification of the α D I-domain using the HisTrap FF 5ml affinity column at 4 °C and a flow rate of 3 ml/min. The protein was eluted with linear gradient of 0-500 mM imidazole in 20 mM Tris, pH 8.0, 300 mM NaCl, 10% glycerol. (B) shows the SDS-PAGE of protein molecular marker (lane 1) and fractions from HisTag/affinity chromatography (Lane 2-11)

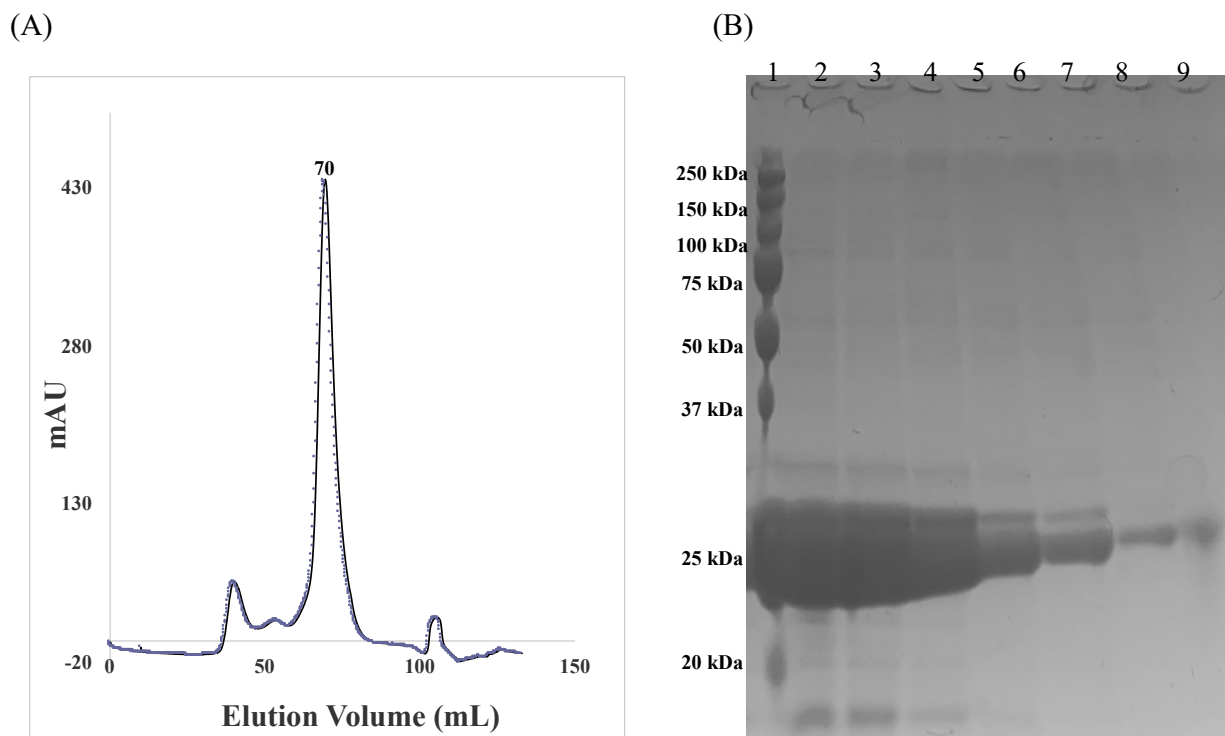


Figure 9: FPLC purification of the α D I-domain protein by gel filtration chromatography and the SDS-PAGE analysis. (A) shows the FPLC purification of the α D I-domain the HiLoad 16-60 S75 column at 4 °C and a flow rate of 1 mL/min. The protein was eluted at elution volume of 69.89 mL using the chelex prepared buffer: 20 mM HEPES, pH 7.4, 150 mM NaCl. (B) shows the SDS-PAGE of protein molecular marker (lane 1) and fractions from size exclusion column chromatography (Lane 2-8)

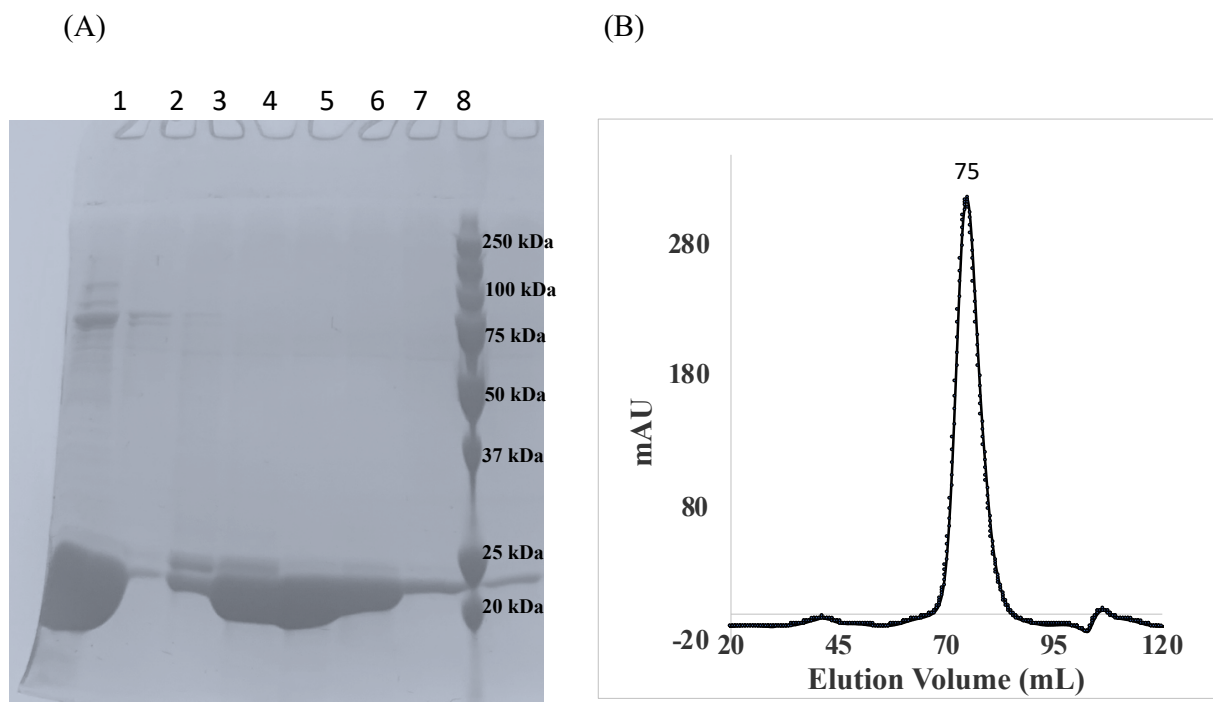


Figure 10: Gel Filtration purification of digested α D I-domain protein by FPLC and the SDS-PAGE analysis. (A) shows the SDS-PAGE of digested protein and fractions from gel filtration chromatography. Lane 1: Histag flow through after 3C protease digestion; Lane 2-7: fractions collected during SEC elution; Lane 8: protein molecular marker. (B) shows the FPLC purification of the digested α D I-domain using the HiLoad 1660 S75 column at 4 °C and a flow rate of 1 ml/min. The protein was eluted at elution volume of 74.86 ml.

3.2 Crystal structure of the α D I-domain integrin protein

3.2.1 Crystallization of α D I-domain

Crystallization is considered as the rate-limiting step in X-ray crystallography studies of macromolecules such as proteins. This is because the success of structure determination by X-ray crystallography depends completely on obtaining diffraction-quality crystals. Usually, the objective is to supersaturate the protein and initiate nucleation and crystal growth. However, it should be noted that nucleation or crystal growth may occur depending on the level of

supersaturation. The three levels of supersaturation are the precipitation zone (the zone of high supersaturation where proteins precipitate), the labile zone (the zone of moderate supersaturation where nucleation occurs), and the metastable zone (the zone of slight supersaturation where crystals that don't nucleate grow). The difficulty in obtaining quality crystals for diffraction makes crystallization one of the narrowest bottlenecks in modern macromolecular crystallography. As expected, the search for initial and optimized crystallization conditions for the protein described in this study also took a great deal of effort. The initial crystallization screening was done with the Phoenix crystallization robot using the sitting drop vapor diffusion method while optimization was done manually using the hanging drop vapor diffusion method.

In the crystallization of the α D I-domain, the first indications of crystal formation were observed in Hampton Crystal screens: HT (HR2-130), Index (HR2-144), and Molecular Dimensions ProPlex (MD1-38). The crystallization screening results from the Hampton Research crystal screens are summarized in Table 2 (HT-HR2-130), Table 3 (Index- HR2-144) and shown in Figure 11 (HT-HR2-130) and Figure 12 (Index- HR2-144). The crystallization screening results from the Molecular Dimensions screen ProPlex MD1-38 are summarized in Table 4 and illustrated in Figure 13. In the crystal screen HT-HR2-130, the few successful conditions included PEG 4000 as the precipitant and sodium citrate tribasic dihydrate as the buffer (Table 2). The most successful conditions were observed in the Index- HR2-144 screen where PEG 3350 was the main precipitant with diverse buffer ranges including Bis-Tris, Tris, and HEPES.

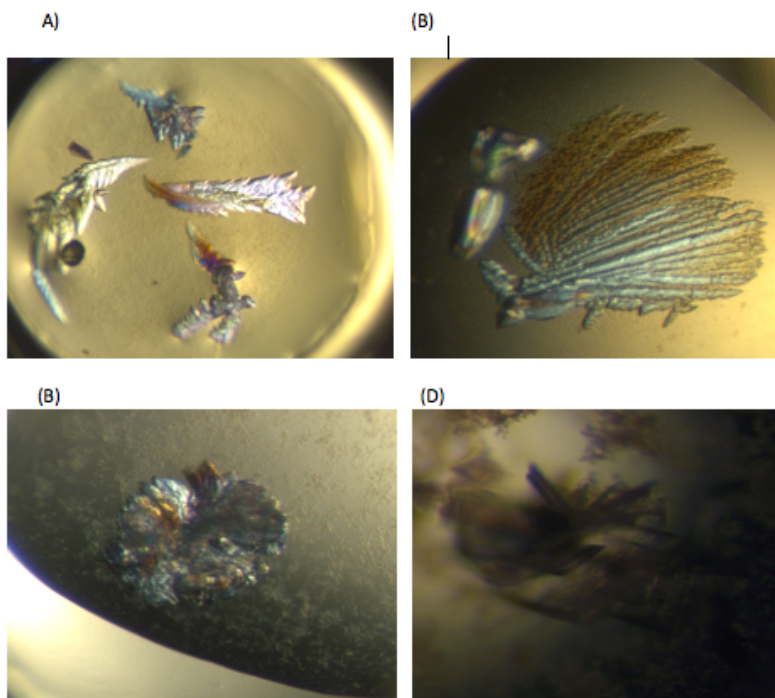


Figure 11: First crystals of α D I-domain obtained using Hampton Research's HT-HR2-130 crystal screen reagents during the initial screening by sitting drop diffusion method. Each crystallization drop consisted of 0.4 μ l of 58 mg/ml of highly purified α D I-domain protein and 0.4 μ l of crystallization reagents. The reagents were (A) 0.1 M HEPES sodium pH 7.5, 1.4 M sodium citrate tribasic dehydrate; (B) 0.2 M ammonium acetate, 0.1 M sodium citrate tribasic dihydrate pH 5.6, 30% w/v PEG 4,000; (C) 1.6 M ammonium sulfate, 0.1 M MES monohydrate pH 6.5, 10% v/v 1,4-Dioxane; (D) 0.1 M HEPES sodium pH 7.5, 2% v/v PEG 4000, 2.0 M ammonium sulfate.

Other chemical reagents like DL-malic acid and ammonium citrate tribasic were successful at growing large three-dimensional and/or symmetrical crystals (Figure 12). For the ProPlex MD1-38 crystal screen, single crystals were obtained in conditions containing PEG 4000 as the precipitant and sodium cacodylate or Tris as the buffer (Figure 13A, B, C). Also, needles or cluster crystals were obtained in conditions containing PEG 6000 as the precipitant and Tris as the buffer (Figure 13D).

Table 2. Hampton Research HT-HR2-130 screen reagents that were selected for optimization and the description of the crystalline material they produced

Reagent formulation	Description of the crystals grown during screening
0.2 M ammonium acetate, 0.1 M sodium citrate tribasic dihydrate pH 5.6, 30% w/v polyethylene glycol 4,000	Plate- and rod-like crystals
0.1 M HEPES sodium pH 7.5, 1.4 M sodium citrate tribasic dihydrate	Plate- and rod-like crystals as well as three-dimensional crystals
1.6 M ammonium sulfate, 0.1 M MES monohydrate pH 6.5, 10% v/v 1,4-Dioxane	Needle cluster (1D Growth)
0.1 M HEPES sodium pH 7.5, 2% v/v polyethylene glycol 4000, 2.0 M ammonium sulfate	Precipitate/phase

Table 3. Hampton Research Index-HR2-144 screen reagents that were selected for optimization and the description of the crystalline material they produced

Reagent formulation	Description of the crystals grown during screening
0.1 M HEPES pH 7.5, 1.4 M sodium citrate tribasic dihydrate	Two-dimensional crystal clusters
1.8 M ammonium citrate tribasic pH 7.0	Single three-dimensional crystals
2.1 M DL-malic acid pH 7.0	Three-dimensional crystal clusters
0.1 M BIS-TRIS pH 6.5, 25% w/v Polyethylene glycol 3,350	Single three-dimensional crystals
0.1 M HEPES pH 7.5, 25% w/v polyethylene glycol 3,350	Single three-dimensional crystals
0.1 M Tris pH 8.5, 25% w/v polyethylene glycol 3,350	Needle cluster (1D Growth)
0.1 M BIS-TRIS pH 6.5, 20% w/v Polyethylene glycol monomethyl ether 5,000	Single three-dimensional crystals
0.2 M Sodium chloride, 0.1 M Tris pH 8.5, 25% w/v polyethylene glycol 3,350	Needle cluster (1D Growth)
0.2 M ammonium acetate, 0.1 M BIS-TRIS pH 6.5, 25% w/v polyethylene glycol 3,350	Needle cluster (1D Growth)
0.2 M ammonium acetate, 0.1 M HEPES pH 7.5, 25% w/v polyethylene glycol 3,350	Needle cluster (1D Growth)
0.2 M ammonium acetate, 0.1 M Tris pH 8.5, 25% w/v polyethylene glycol 3,350	Needle cluster (1D Growth)
0.2 M sodium malonate pH 7.0, 20% w/v polyethylene glycol 3,350	Needle cluster (1D Growth)
0.2 M sodium formate, 20% w/v polyethylene glycol 3,350	Needle cluster (1D Growth)
0.15 M DL-malic acid pH 7.0, 20% w/v polyethylene glycol 3,350	Needle cluster (1D Growth)

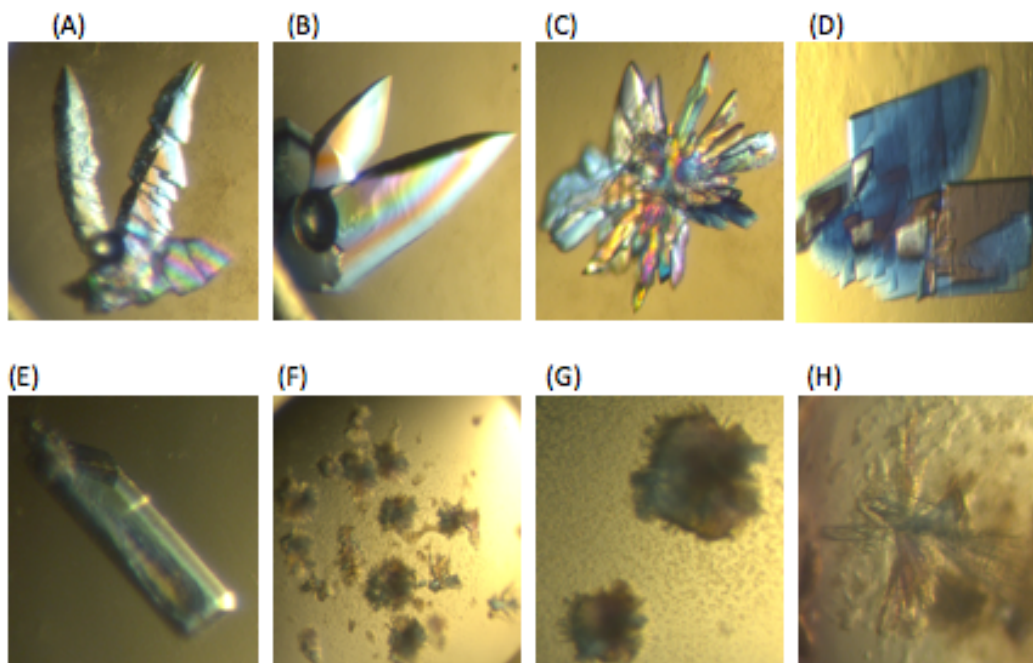


Figure 12: Crystals of the α D I-domain obtained using Hampton Research's HT-HR2-144 crystal screen reagents during the initial screening by sitting drop diffusion method. Each crystallization drop consisted of 0.4 μ l of 58 mg/mL of highly purified α D I-domain protein and 0.4 μ l of crystallization reagents. The reagents were (A) 0.1 M HEPES sodium pH 7.5, 1.4 M sodium citrate tribasic dehydrate; (B) 1.8 M ammonium citrate tribasic pH7.0 (C) 2.1M DL malic acid pH 7.0; (D) 0.1 M Bis-Tris pH6.5, 25% PEG 3350; (E) 0.1 M HEPES pH 7.5, 25% PEG 3350; (F) 0.1 M Tris pH 8.5, 25% PEG 3350; (G) ammonium acetate 0.1 M Bis-Tris pH 8.5, 25% PEG 3350; (H) 0.2 M sodium malonate pH 7.0, 20% PEG 3350.

Table 4. Molecular Dimensions screen ProPlex (MD1-38) reagents that were selected for optimization and the description of the crystalline material they produced

Reagent formulation	Description of the crystals grown during screening
0.1 M Tris pH 8.0 20% w/v polyethylene glycol 4,000	Single three-dimensional crystals
0.1 M sodium cacodylate pH 5.5 25% w/v Polyethylene glycol 4,000	Single three-dimensional crystals
0.1 M sodium cacodylate pH 6.5 25% w/v polyethylene glycol 4,000	Single three-dimensional crystals
0.1 M Tris pH 8.5 15% w/v polyethylene glycol 6,000	Needle cluster (1D Growth)
0.1 M Tris pH 8.5 20% w/v polyethylene glycol 6,000	Needle cluster and plate-like (two-dimensional) crystals

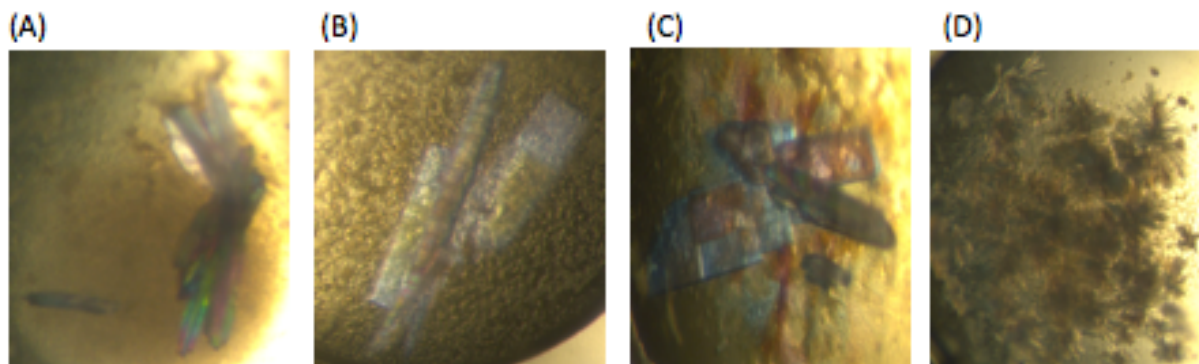


Figure 13: Crystals of the α D I-domain obtained using Molecular Dimensions screen ProPlex (MD1-38) crystal screen reagents during the initial screening by sitting drop diffusion method. Each crystallization drop consisted of 0.4 μ l of 58 mg/ml of highly purified α D I-domain protein and 0.4 μ l of crystallization reagents. The reagents were (A) 0.1 M Tris pH 8.0, 20% PEG 4000; (B) 0.1 M sodium cacodylate pH 5.5, 25% PEG 4000; (C) 0.1 M sodium cacodylate pH 6.5, 25% PEG 4000; (D) 0.1 M Tris pH 8.5, 15% PEG 6000.

The crystallization conditions were optimized by mostly varying the concentration or percent of the precipitating agents (PEG 3350 and PEG 4000). The conditions that produced crystals from optimizing Hampton Research screens were 1.5-2.1 M DL-malic acid (pH 7.0); 0.1 M Bis-Tris (pH 6.5) 10-18% w/v PEG 3350; 0.1 M HEPES (pH 7.5) 12.5-25% w/v PEG 3350, and 0.1 M Tris (pH 8.5) 10-18% w/v PEG 3350 at 4 °C. Some of the crystals were multicolored and multilayered, irregularly shaped, and were easily broken during harvesting (Figure 14). Others grew as clear/multicolored long rods, rod clusters, twinned and three-dimensional crystals (Figure 15). Long and multicolored proteins were obtained from ProPlex MD1-38 conditions containing 0.1 M sodium cacodylate (pH 6.5), 10-16% PEG 4000 (Figure 16). Finally, clear and different shapes of crystals in various sizes were obtained from co-crystallization of the α D I-domain in 0.1 M HEPES buffer supplemented with different concentration of selected meta ions (Mg^{2+} , Mn^{2+} , Ca^{2+} , Cd^{2+} , Co^{2+} , and Zn^{2+}) as shown in Figure 17.

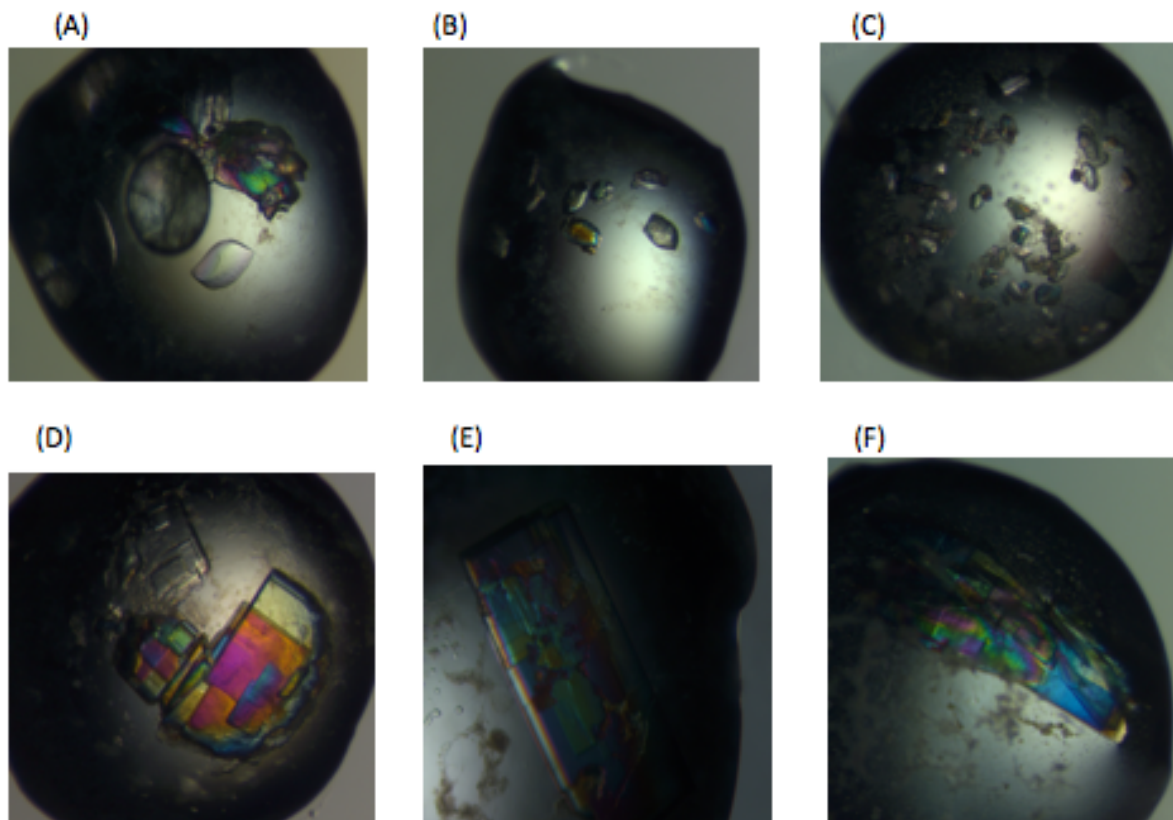


Figure 14: The birefringent and multilayered irregularly shaped crystals of the α D I-domain obtained after optimization of the Hampton Research crystallization conditions. Many of these crystals were easily broken during harvesting and therefore further optimization was needed. The crystal drop contains 2 μ l of 55 mg/ml α D I-domain and 2 μ l of the reservoir solution. All the crystals were grown at 4 $^{\circ}$ C. (A) 2.1 M DL-malic acid pH 7.0, further refining gave crystals, which diffracted X-rays well (B) 0.1 M Bis-Tris (pH 6.5), 15% w/v PEG 3,350. (C) 0.1 M Bis-Tris (pH 6.5), 18% w/v PEG 3,350 (D) 0.1 M HEPES (pH 7.5), 25% w/v PEG 3,350. (E) 0.1 M Tris (pH 8.5), 25% w/v PEG 3,350. (F) 0.1 M HEPES (pH 7.5), 10% w/v PEG 3,350

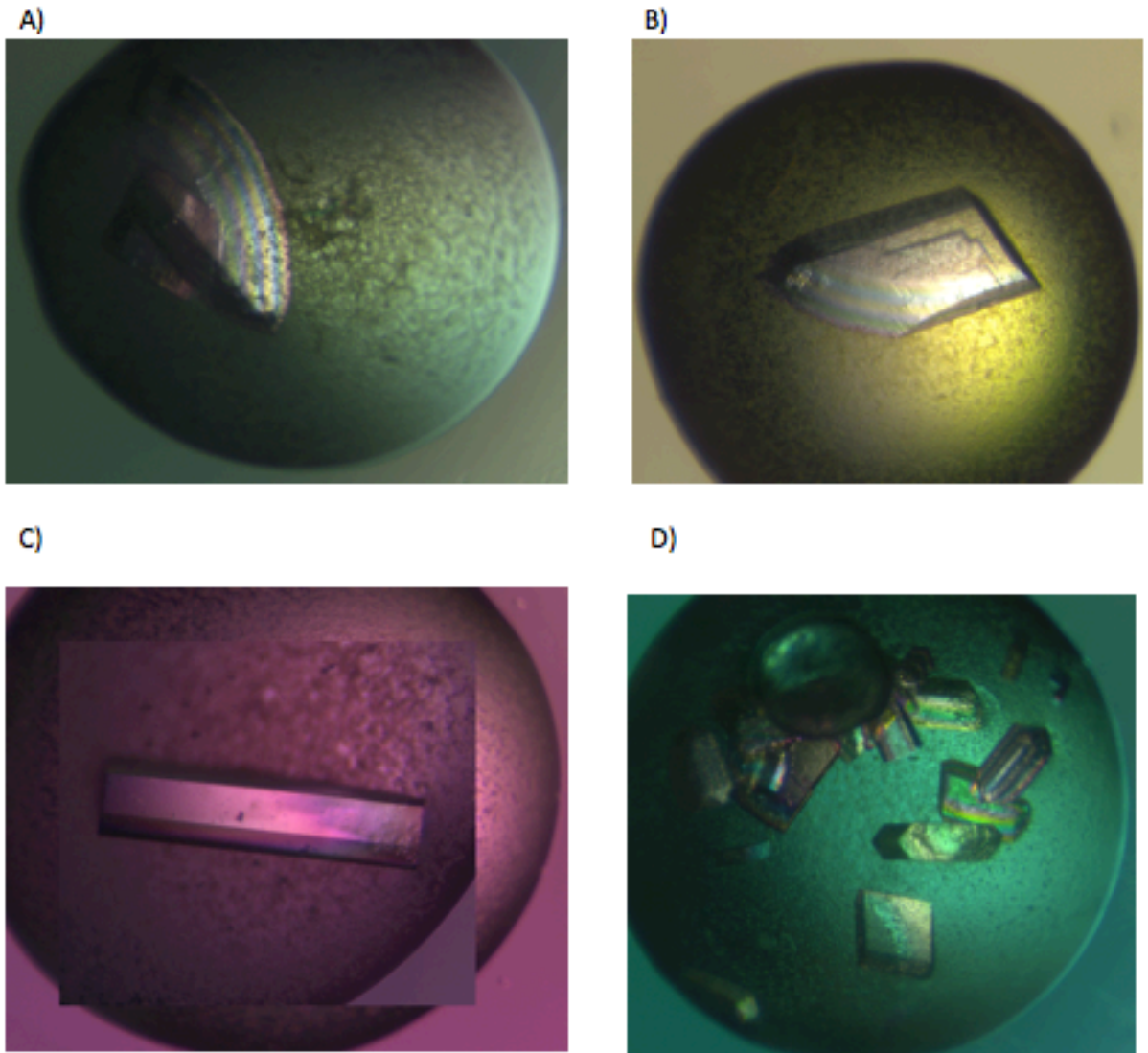


Figure 15: Clear/birefringent long rods, rod clusters, and three-dimensional crystals of the α D I-domain obtained after final optimization of the Hampton Research crystallization conditions using hanging drop diffusion method. These crystals enabled the collection of higher resolution data (up to 1.2 Å). (A) 1.5 M DL-malic acid pH 7.0. (B) 0.1 M HEPES (pH 7.5), 22.5% w/v PEG 3,350. (C) 0.1 M HEPES (pH 7.5), 12.5% w/v PEG 3,350. (D) 0.1 M Tris (pH 8.5), 15% w/v PEG 3,350.

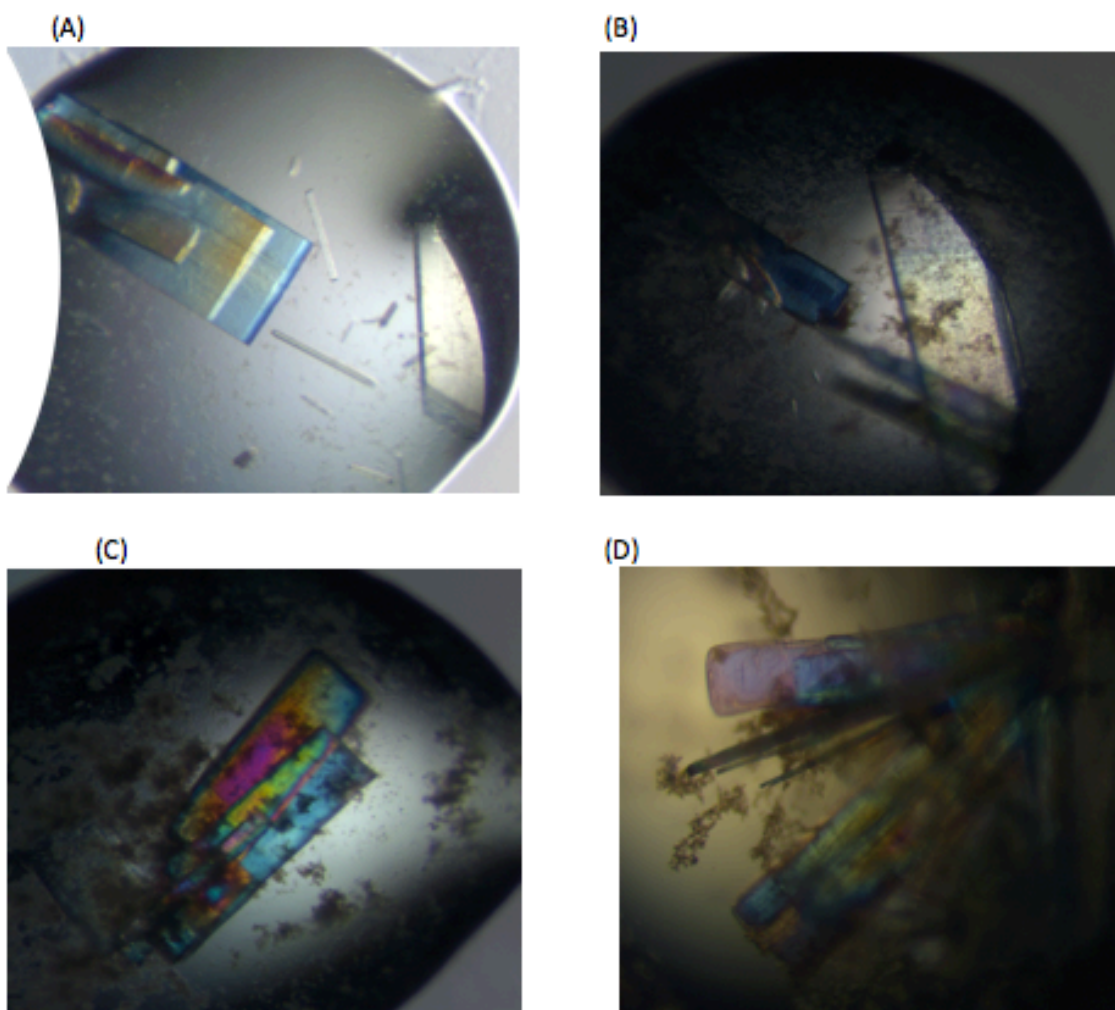
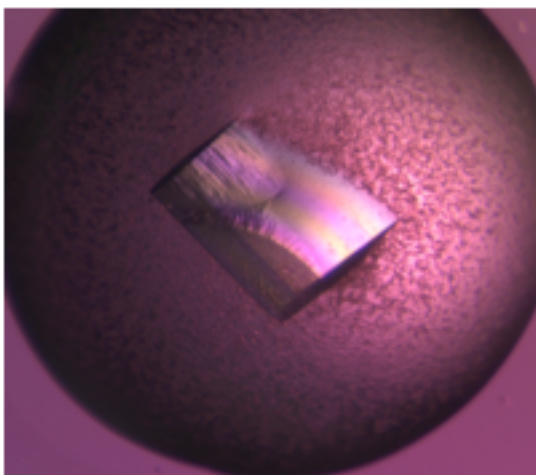
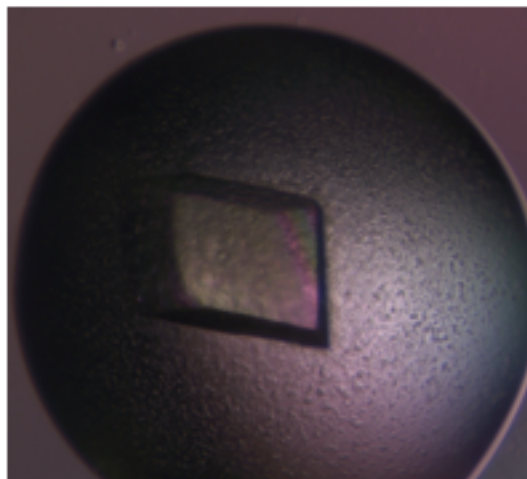


Figure 16: Crystals of the α D I-domain. Protein after refining crystallization conditions with formulation reagents from the Molecular Dimensions screen. These crystals diffracted X-rays well (A) The reservoir solution comprised of 0.1 M sodium cacodylate (pH 6.5), 10% PEG 4,000. Higher resolution data was collected (up to 1.2 Å) (B) The reservoir solution comprised of 0.1 M sodium cacodylate (pH 6.5), 12% PEG 4,000. (C) The reservoir solution comprised of 0.1 M sodium cacodylate (pH 6.5), 15% PEG 4,000. (D) The reservoir solution comprised of 0.1 M sodium cacodylate (pH 6.5), 16% PEG 4,000.

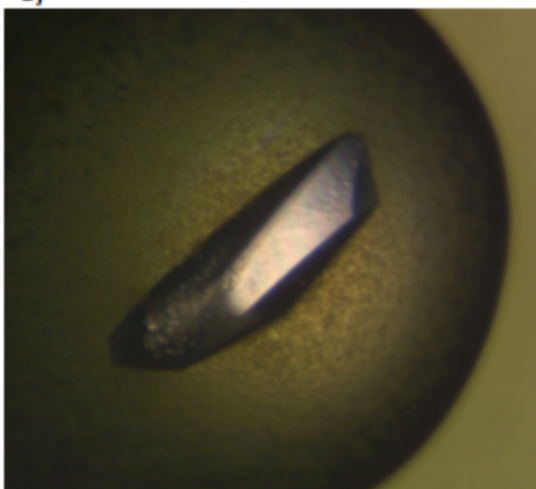
(A)



(B)



(C)



(D)

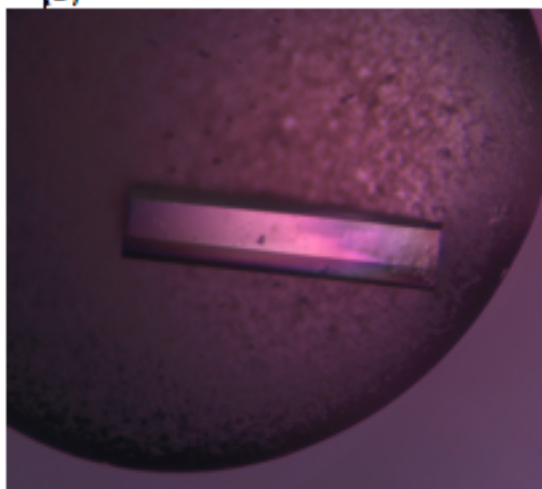


Figure 17: Crystals of the α D I-domain grown in a reservoir containing 0.1 M HEPES buffer and 12.5 % - 25% w/v PEG 3,350 supplemented with different metal cations. The crystal drop comprised of 1 ul or 2 ul of 55 mg/ml α D I-domain and 2 ul of the reservoir solution. All the crystals were grown at 4 ° for about 7 d. (A) The reservoir contained 5 mM MgCl_2 . (B) 5 mM CaCl_2 . (C) 5 mM CdCl_2 . (D) 5 mM MnCl_2 .

3.2.2 Data collection, molecular replacement and structure refinement

The crystals grown in PEG 3350 precipitants (Figure 15B-D) yielded 1.2 Å resolution (Figure 18A) and belonged to the orthorhombic space group $P22_12_1$ (Table 5). On the other hand, the crystals grown in 2.1 M malic acid as precipitants yielded a 1.32 Å resolution (Figure 18B) and belonged to the orthorhombic space group $P 2_12_12_1$ (Table 5). The diffraction data obtained suggests that the reflections recorded during X-ray diffraction data collection were from a single crystal (APPENDIX). The crystals grown in PEG 3350 and DL-malic acid have different cell constants with one and two molecules per asymmetric units respectively (Figure 19). The data collection statistics from both crystal types are summarized in Table 5. PHASER molecular replacement was used to obtain the phases. After fitting the polypeptide residues and several rounds of refinement using PHENIX and COOT programs, the final model of the α D I-domain was successfully determined. In all the structures, all the 192 amino acid residues including the malic acid positioned at the lattice contact were fitted in the electron density (Figure 19B). Structural validation is now up to standards for structure deposition (Table 5). For example, in both crystal types, over 96% of the modeled residues are in the favored region of the Ramachandran, while about 2.6% and 1.0% are in the allowed and disallowed regions, respectively (Figure 20).

Table 5. Data collection and refinement statistics ^a

	PEG3350 Crystal	Malic Acid Crystal
Data collection		
Space group	P22 ₁ 2 ₁	P2 ₁ 2 ₁ 2 ₁
Cell dimensions		
<i>a, b, c</i> (Å)	34.94, 75.78, 90.64	52.58, 62.27, 109.93
α, β, γ (°)	90.00, 90.00, 90.00	90.00, 90.00, 90.00
Resolution Range(Å)	29.07—1.2	26.79—1.32
CC _{1/2} (%) ^b	99.9 (98.9)	99.9 (81.4)
<i>R</i> _{merge} ^c	4.2 (11.1)	4.1 (41.1)
<i>I</i> / σ (<i>I</i>)	26.55 (2.75)	19.23 (1.98)
Completeness (%)	98.3 (87.2)	97.5 (81.93)
Redundancy (%)	5.92 (3.2)	5.62 (2.47)
Refinement		
Resolution (Å)	1.2	1.3
No. reflections (total/unique)	74869 (6577)	83414 (6882)
% <i>R</i> _{work} ^d / <i>R</i> _{free} ^e	16.65/17.68	18.24/19.46
<i>No. atoms</i>		
Protein	1523	3040
Ion	1	9
Water	243	440
<i>B factors (Mean)</i>	<i>16.83</i>	<i>24.90</i>
Protein	15.38	23.52
Ion	12.12	24.36
Water	25.93	34.47
Mol/asym unit	1	2
Ramachandran (%) ^f	(96.86, 3.14, 0.00)	(95.85, 4.15, 0.00)
MolProbity Score	1.04 (98%)	1.50 (
ClashScore	1.31 (98%)	4.43 (92%)
<i>R.m.s deviations</i>		
Bond lengths (Å)	0.005	0.006
Bond angles (°)	0.856	1.046

^aNumbers in parentheses correspond to the outermost resolution shell.

^b CC_{1/2}= Pearson's correlation coefficient between average intensities of random half-datasets for each unique reflection (Karplus, P.A. and Diederichs, K. Linking Crystallographic Model and Data Quality. *Science*. 336, 1030-1033 (2012)).

^c $R_{\text{merge}} = \frac{\sum hkl \sum i |I_i(hkl) - \langle I(hkl) \rangle|}{\sum hkl \sum i I_i(hkl)}$, where $I_i(hkl)$ and $\langle I(hkl) \rangle$ are the *i*th and mean measurement of the intensity of reflection *hkl*.

^d $R_{\text{work}} = \frac{\sum hkl |F_{\text{obs}}(hkl) - F_{\text{calc}}(hkl)|}{\sum hkl F_{\text{obs}}(hkl)}$, where $F_{\text{obs}}(hkl)$ and $F_{\text{calc}}(hkl)$ are the observed and calculated structure factors, respectively. No *I*/ σ cutoff was applied.

^e*R*_{free} is the *R* value obtained for a test set of reflections consisting of a randomly selected ~5% subset of the data set excluded from refinement.

^fResidues in favored, accepted, and outlier regions of the Ramachandran plot as reported by MOLPROBITY.

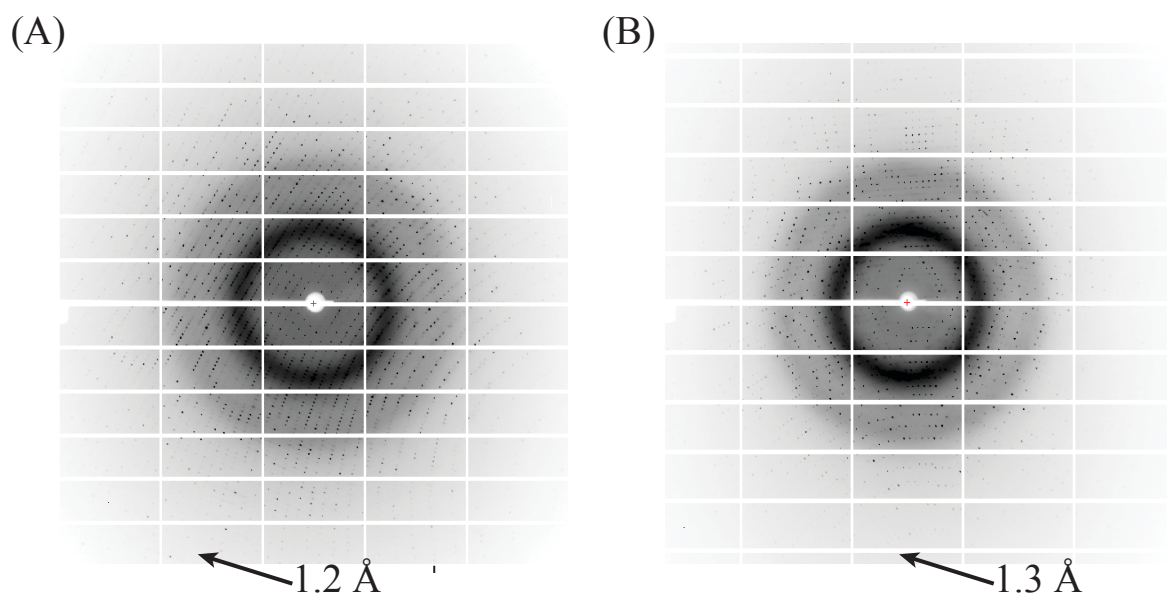


Figure 18: A high-resolution diffraction image of the (A) Mg^{2+} -bound (PEG 3350 precipitant) and (B) Mg^{2+} -free (malic acid precipitant) αD I-domain showing high resolution limits of 1.2 Å and 1.3 Å, respectively.

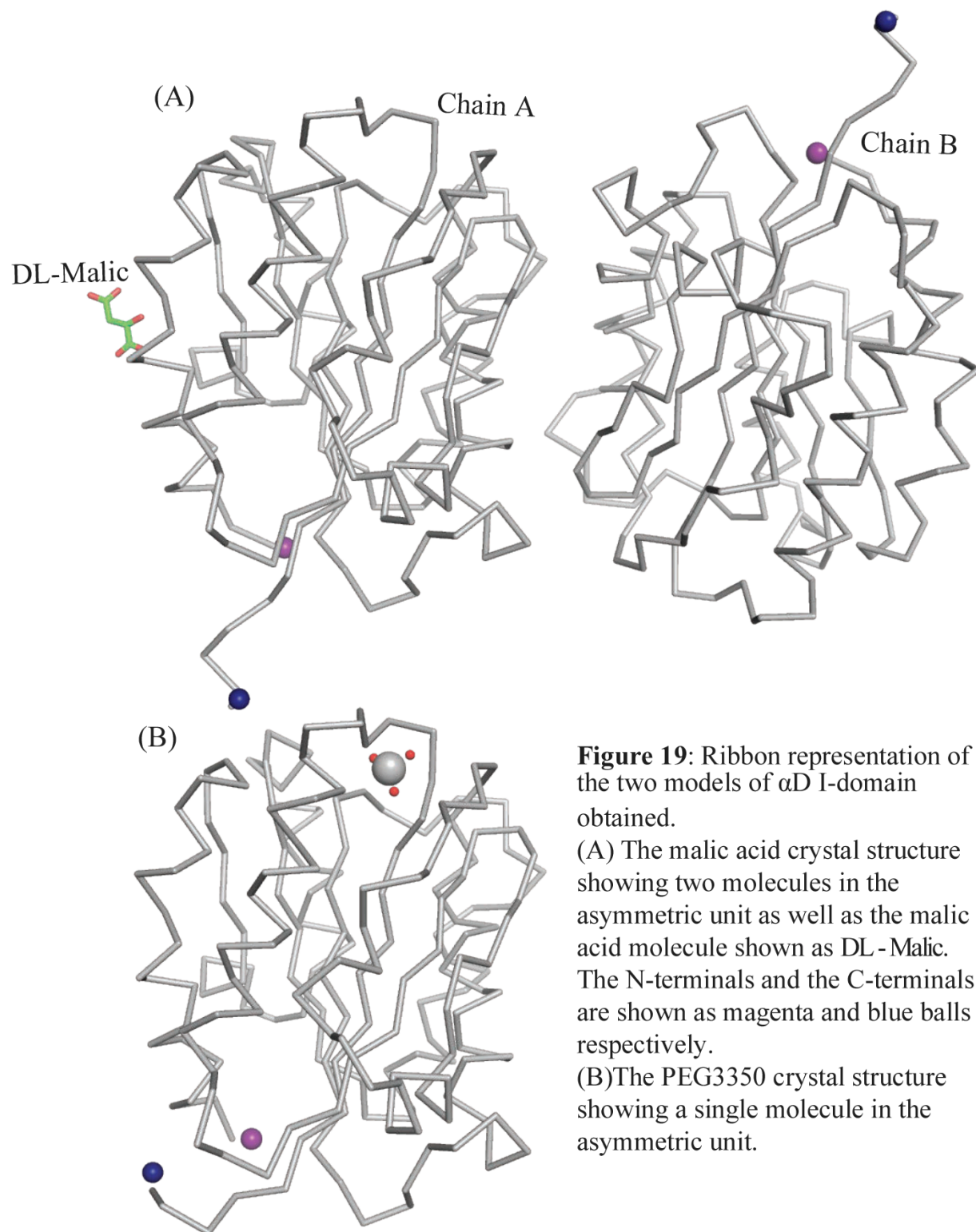


Figure 19: Ribbon representation of the two models of α D I-domain obtained.

(A) The malic acid crystal structure showing two molecules in the asymmetric unit as well as the malic acid molecule shown as DL - Malic. The N-terminals and the C-terminals are shown as magenta and blue balls respectively.

(B) The PEG3350 crystal structure showing a single molecule in the asymmetric unit.

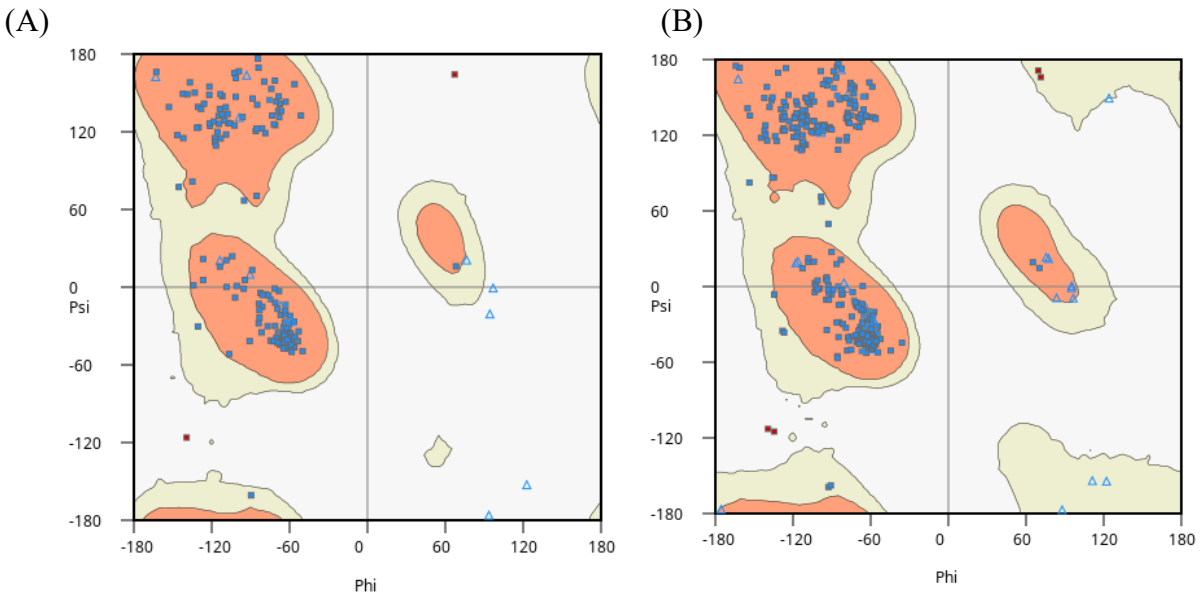


Figure 20: Ramachandran outliers in the refined model of α D I-domain protein.

Ramachandran plot showing the Φ and Ψ angles of individual amino acid residues in (A) PEG 3350 model and (B) malic acid model. In (A), 181 (96.28%), 5 (2.66%) and 2 (1.06%) amino acid residues (Lys 205 and Ser 176) are found in the preferred, allowed and outlier regions respectively. In (B), 369 (96.34%), 10 (2.61%) and 4 (1.04%) amino acid residues (Lys 205 and Ser 176 in chain A; and again Lys 205 and Ser 176 in chain B) are found in the preferred, allowed and outlier regions, respectively. In both crystal structures, the outliers are represented in red color.

3.3 X-Ray structure of the α D I-domain

The primary determined structure of the α D I-domain protein consists of about 192 amino acid residues with a calculated isoelectric point (pI) of 6.59. The molecular weight of the polypeptide from the amino acid sequence is approximately 22 kDa. The hydropathy index plot (Figure 21) of α D I-domain sequence reveals a relative hydrophobicity of segments of the protein. The Kyte and Doolittle hydropathicity scaling method of amino acids score individual amino acids on a scale of -2.5 to 2.5 , where values below 0 indicate hydrophilic regions on the protein sequence while peaks above 0 indicate hydrophobic regions of the protein sequence. The negative grand average of hydropathy (GRAVY) of -0.108 indicate the α D I-domain sequence consists of a few more hydrophilic residues than hydrophobic residues.

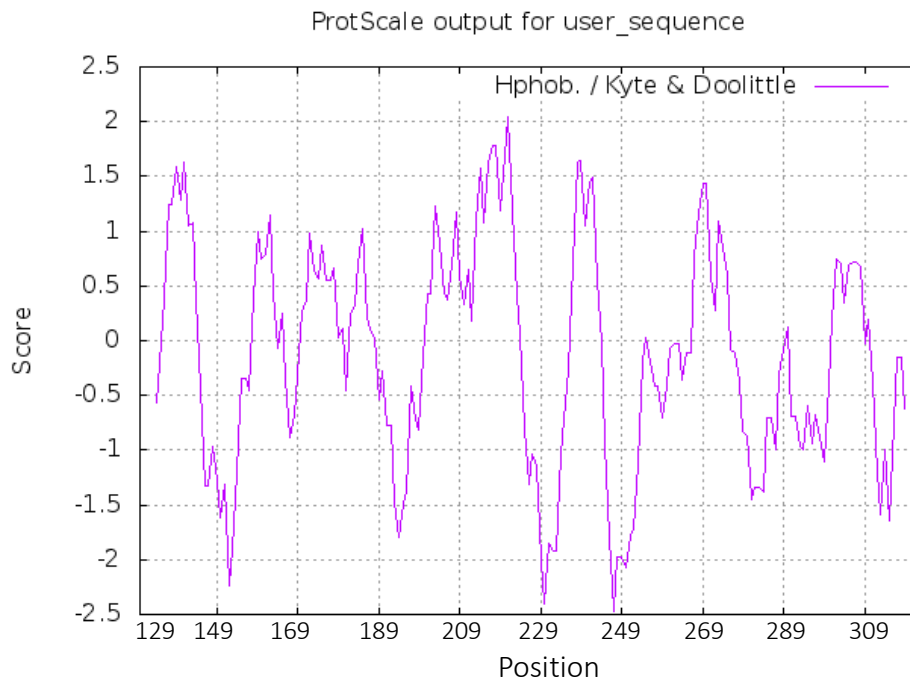


Figure 21: The hydropathy index plot of α D I-domain protein sequence using the Kyte and Doolittle hydropathicity scaling method of amino acids (Kyte and Doolittle, 1982). Values below 0 indicate hydrophilic regions on the protein sequence of α D I-domain while peaks above 0 indicate hydrophobic regions of the protein sequence.

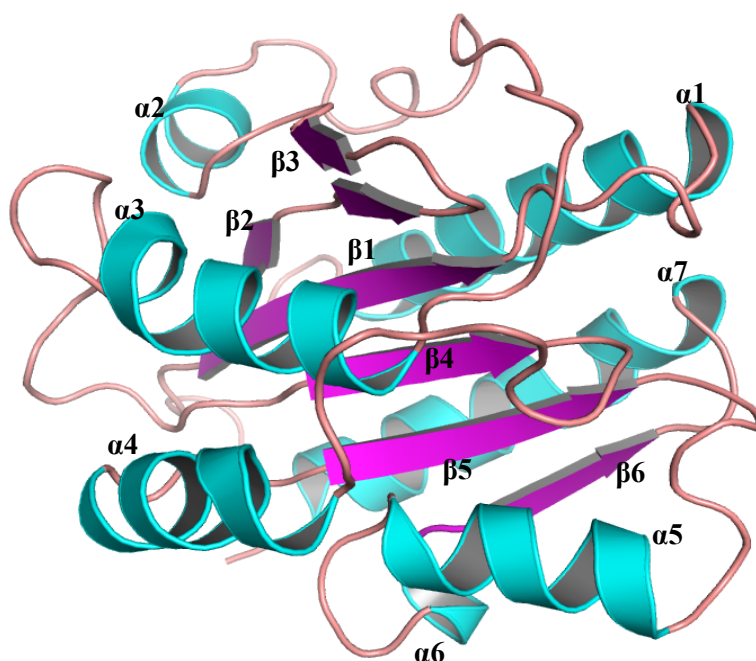


Figure 22: Annotated cartoon diagram of the refined model structure of the α D I-domain protein showing the secondary structure composition. α -helices are colored cyan, b-strands are magenta, and loop/turns are wheat. Figures were generated using the program PYMOL (DeLano, 2002).

The secondary structure of the α D I-domain showed five parallel and one short antiparallel β -strands that is surrounded by seven alpha helices, adopting a classic Rossman fold (Figure 22). The α D I-domain contains a single metal-binding site (MIDAS). This MIDAS contains Mg^{2+} located on the surface of the α I-domain at the top of the beta sheet. The Mg^{2+} forms polar contacts with the hydroxyl oxygen atoms of three residues and three water molecules. The side chain of seven residues coordinate the metal ion with the α DI-MIDAS either directly or via hydrogen bonding. Notably, the side chains of S141, S143 and D241 directly coordinate the metal ion while D139, T208, I144, and G242 coordinates the metal ion through hydrogen bonding (Figure 23B).

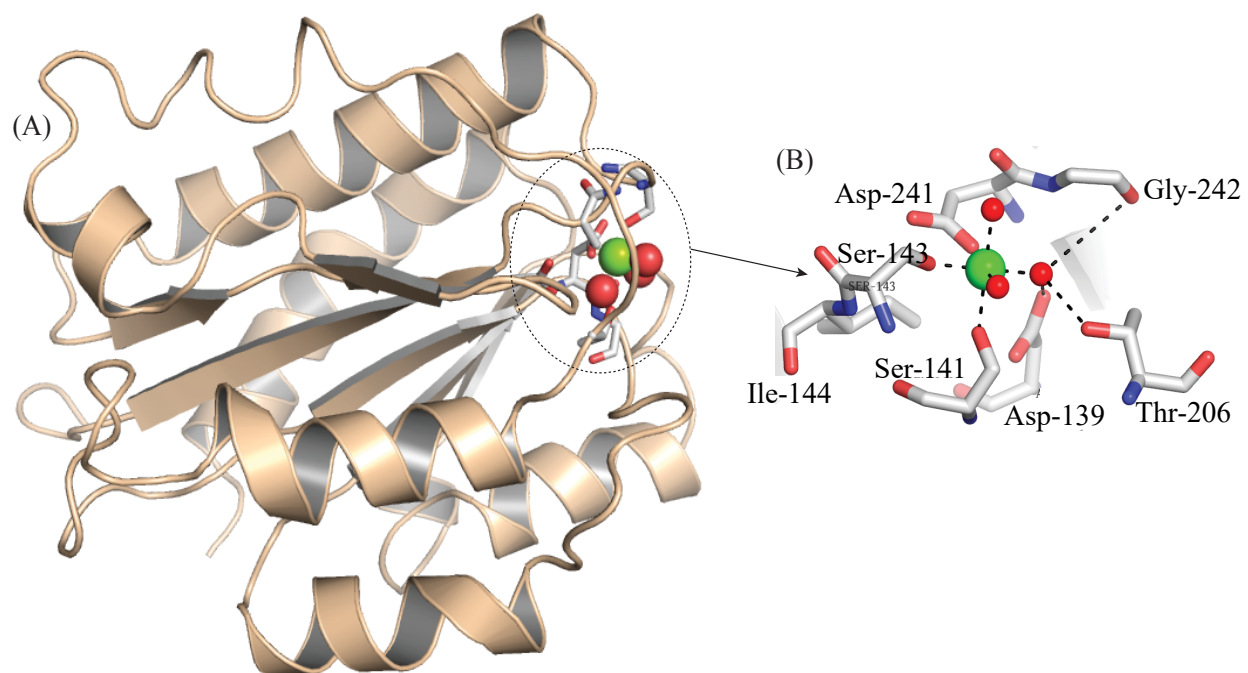


Figure 23: Representation of the MIDAS region of the α D I-domain.

(A) The binding site (MIDAS region) of the α D I-domain, which is circled is located on the surface of the protein. (B) The Mg^{2+} -ion shown as green sphere is coordinated by three water molecules (red spheres) and seven amino acid residues as explained above. The coordination bonds are shown by black dashes

3.4 Difference between M^{2+} -free and M^{2+} containing α D I-domain Structures

As indicated earlier, the PEG 3350 precipitant crystal model contains Mg^{2+} while the malic acid crystal model is Mg^{2+} -free. To compare any structural difference between the two crystal structures, we superimposed the α D I-domain structures (with and without Mg^{2+}). The overall structural difference between two structures is marginal but more pronounced for the allosteric secondary structures— $\alpha 1$, $\alpha 6$, and $\alpha 7$ -helices (Figure 24B). In all α I-domain integrins, the $\alpha 7$ -helix is directly involved in the activation and also during conformational changes. Comparison of the MIDAS of the two structures has shown that when free of Mg^{2+} ion, the MIDAS is occupied by

two water molecules and adopts the closed state geometry (Figure. 24B-green structure). Upon Mg^{2+} -binding, there is a geometric reconfiguration of the MIDAS residues. The binding of Mg^{2+} causes the amino acid residue D241 rotamer to pivot, and as a result links D241 to Mg^{2+} through ionic coordination (Figure 24B-cyan). This may lead to the subsequent extension of the $\alpha 7$ -helix and finally ligand binding. There is also an introduction of an extra water molecule, which subsequently coordinate the Mg^{2+} metal to other MIDAS residues (D139 and T208) through hydrogen bonding.

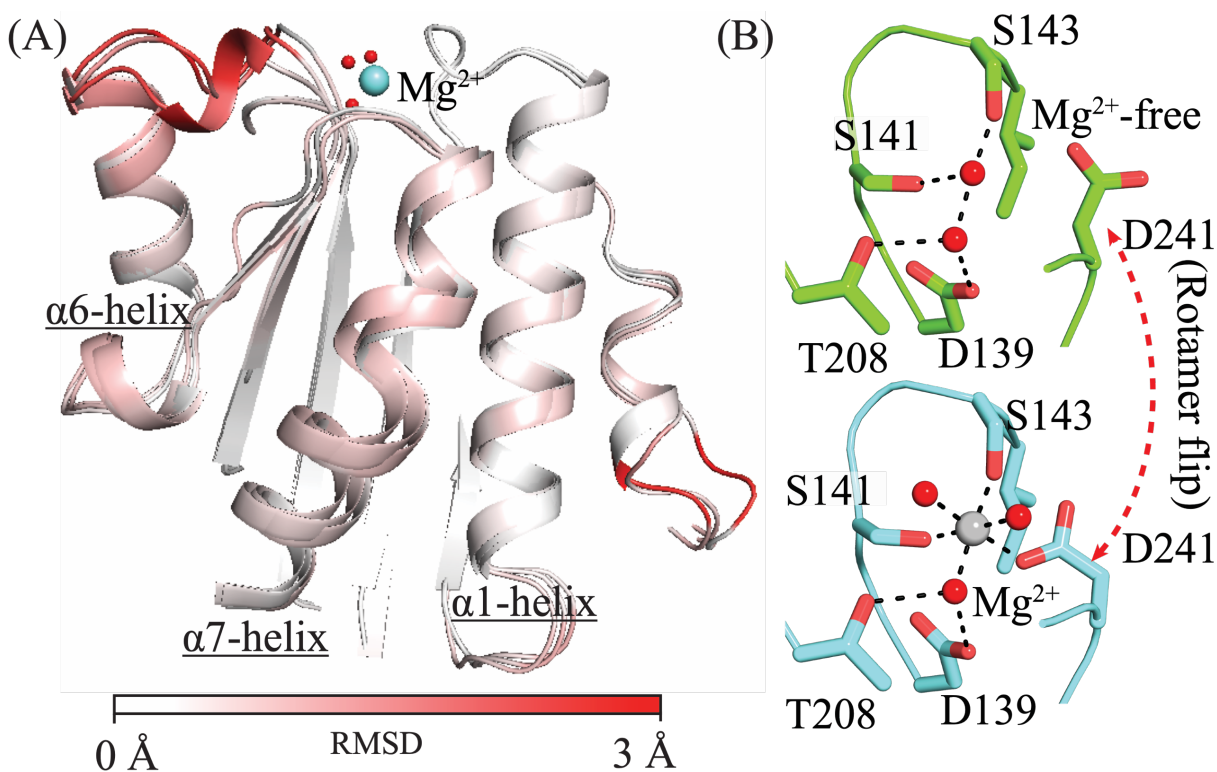


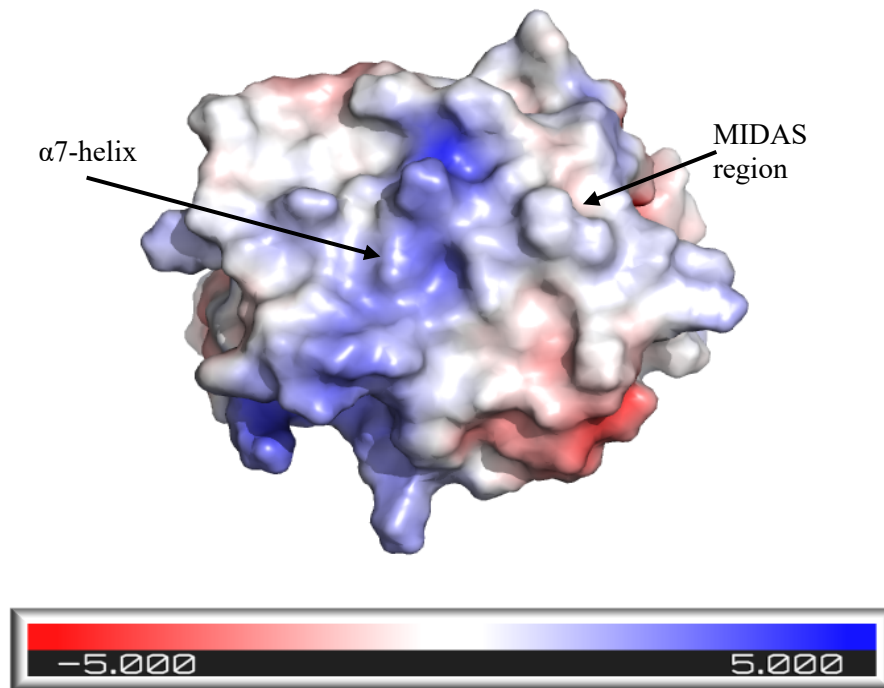
Figure 24: (A) Structural changes between two crystal lattices with and without Mg^{2+} -ion. The mapped structures were colored based on RMSD, prominently showing pronounced secondary structure motions in the helix-triad. (B) Geometric reconfiguration of MIDAS upon Mg^{2+} -ion binding.

3.5 Surface charge of the α D I-domain crystal structure

The electrostatic charge or charge distribution on the surface of proteins contribute to what binds to the protein and how it is binding. We used APBS (Baker et al., 2001; Lerner and Carlson, 2006) as a plugin and calculated the electrostatic distribution and mapped it to the α D I-domain surface. On the surface of α D I-domain, both positively and negatively charged regions are observed (Figure 25). The overall or total surface charge as calculated by the PYMOL program was -1 . As indicated earlier, the isoelectric point (pI) of the α D I-domain protein is 6.59. Theoretically, the electrostatic surface charge was estimated around pH 7.0, which is above the pI and, thus, may account for the negative net charge calculated by Pymol.

Notably, the MIDAS region, which consists of two aspartate residues (negatively charged) (Figure 24B) is shown to have a negatively charged surface. This may contribute to the binding of metal ions at the MIDAS region. Also, on the surface of α D I-domain positively charged residues can be predominantly observed at the α 7-helix region.

Figure 25: Electrostatic surface charge representation of integrin α D I-domain in kilo-electron volts per mole. The molecule is rendered as a surface that is colored according to the electrostatic potential. As the color legend indicates, the red color (negative potential) arises from excess of negative charges near the surface and the blue color (positive potential) occurs when the surface is positively charged. The white regions correspond to the fairly neutral potentials.



3.6 Comparison of the α I-domains

Integrin α D I-domain is the most recently identified member of the β 2 (leukocyte) integrin family. So far, the three-dimensional structures—containing metal ions— of the isolated α L (Qu and Leahy, 1995) and α M I-domains (Lee et al., 1995), and the α X I-domain (Vorup-Jensen et al., 2003) on the ectodomain have been determined.

All the known structures of the α I-domain of β 2 integrins indicate common or similar structural properties as discussed in section 1.9. Our solved α D I-domain structure shares the same fold (Rossman fold) with all members of the β 2 integrin family. Amino acid sequence alignments of members of this integrin family shows that there are several highly conserved residues. α D I-domain shares about 60% sequence identity with α M I-domain and α X I-domain but shares only about 34% sequence identity with α L I-domain (Figure 26 and Table 6).

The conserved amino acid residues in all four members of the $\beta 2$ integrin α I-domain include one aspartate (D) residue, two serine (S) residues, two glycine (G) residues and an isoleucine (I) residue located at the MIDAS on the surface of the I-domain at the top of the beta sheets (Figure 27). These residues form the DGSGSI conserved sequence with the exception of α L I-domain where second glycine and the isoleucine residues are replaced with methionine (M) and leucine (L) (Figures 26, 27). The environment that these residues create is very important for Mg^{2+} and ligand binding and their residence time. Indeed, the α L I-domain has different cation affinity and more selective ligand preference in comparison to the other three leukocyte α I-domains.

The overall structural difference among these four α I-domains is prominently observed at the helix-triad ($\alpha 1$, $\alpha 6$, and $\alpha 7$ -helices). The tendency or frequency of an amino acid occurring in alpha-helices is known as the helix propensity. Analysis of the “helix-triad” module in α D, α X, α M, and α L I-domains showed significant variability in their helical propensity, suggesting that differential local dynamics and conformational variability exist in this helix-triad (Figure 28). Comparison of the electrostatic charge surfaces (Figure 29) and the isoelectric points (pI) of all four α I-domains (Table 6) showed significant differences.

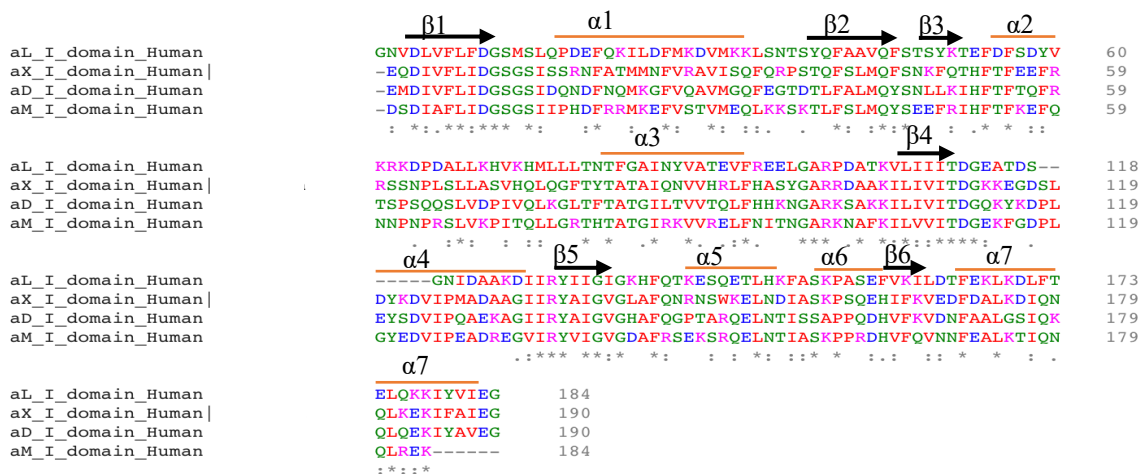


Figure 26: Sequence alignments of the $\beta 2$ integrin family. Conserved residues in all sequences are indicated by “*” and other identical residues are marked with “:” and “.”. secondary structure elements are indicated above the sequences.

Table 6. Sequence identity, pI and estimated surface charge comparison between the αD I-domain and its homologous $\beta 2$ integrin family members. The total surface charge for each protein was computed in PYMOL.

Protein	pI	Total surface charge	Sequence identity (%) to αD I-domain	Overlapped residues	Compared to
αL I-domain	5.61	-4.0	34	63	αD I-domain
αM I-domain	9.33	+4.0	61	112	αD I-domain
αX I-domain	7.24	+1.0	58	110	αD I-domain
αD I-domain	6.59	-1.0	100	190	αD I-domain

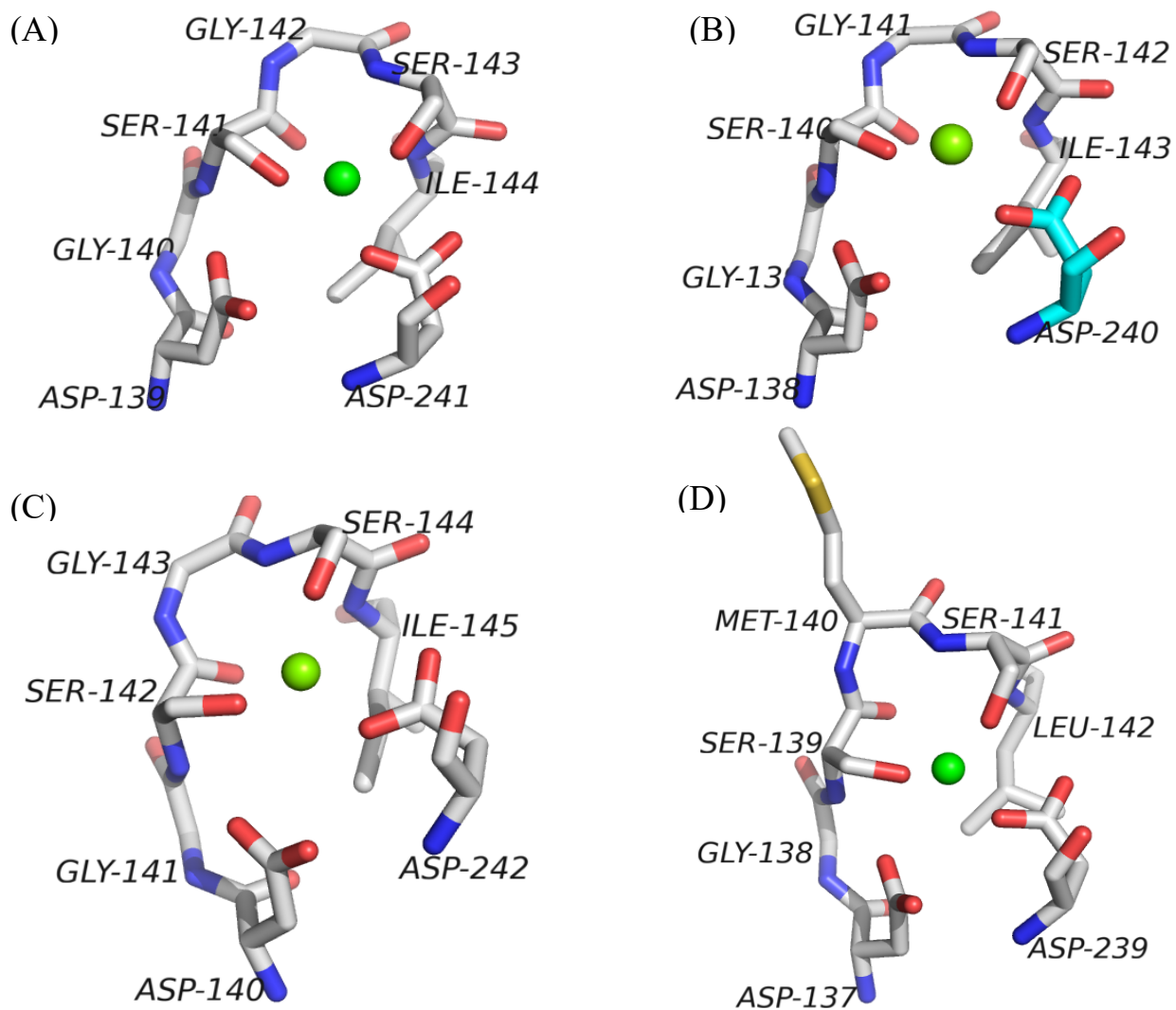


Figure 27: Illustration of the MIDAS residues (conserved residues) of the α D I-domain and homologous structures. (A) the α D I-domain, (B) the α X I-domain, (C) the α M I-domain, and (D) the α L I-domain. Magnesium found in the MIDAS is shown as sphere and colored green.

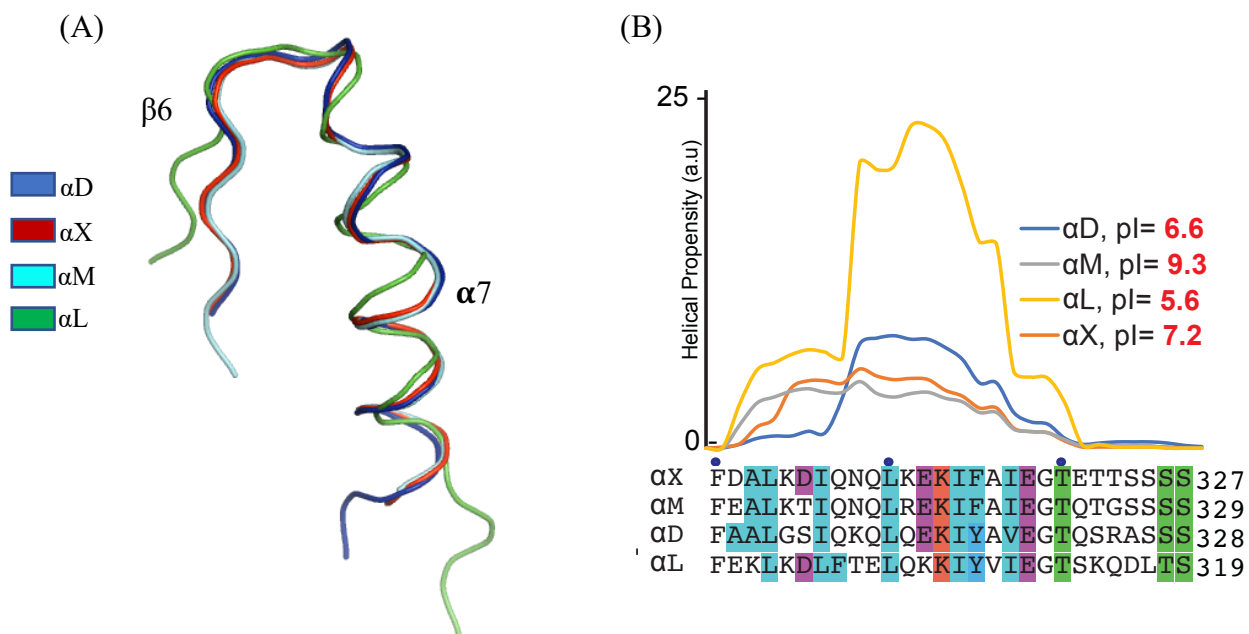


Figure 28: (A) Differences in helical propensity of the $\alpha 7$ -helices of members of the $\beta 2$ integrin αI -domain. Inserted is the isoelectric point (pI) values for each protein. The amino acid sequence for the $\alpha 7$ -helices is also shown below the plot. (B) Comparison of the C-terminal $\beta 6$ -strand and $\alpha 6$ - $\alpha 7$ helix. The backbone segments shown are αD , residues 291-318; αX , residues 290-320 of 1N3Y (Vorup-Jensen et al., 2003); αM , residues 295-318 of 1JML (Kuhlman et al., 2001); and αL , residues 283-310 of 1LFA (Qu and Leahy, 1995).

A quick computation of the total surface charges for each of the structures in PYMOL showed that αD and αL have negative total surface charges, -1 and -4 , respectively, while αX and αM gave positive total formal charge sum of $+1$ and $+4$, respectively (Figure 29, Table 6). The total surface charge at the MIDAS region for all four structures was computed to be -2 . This could suggest why the positive charged metal-ions (M^{2+}) are attracted to the MIDAS. However, the total surface charge at the helix-triad was different for all four structures (Table 6).

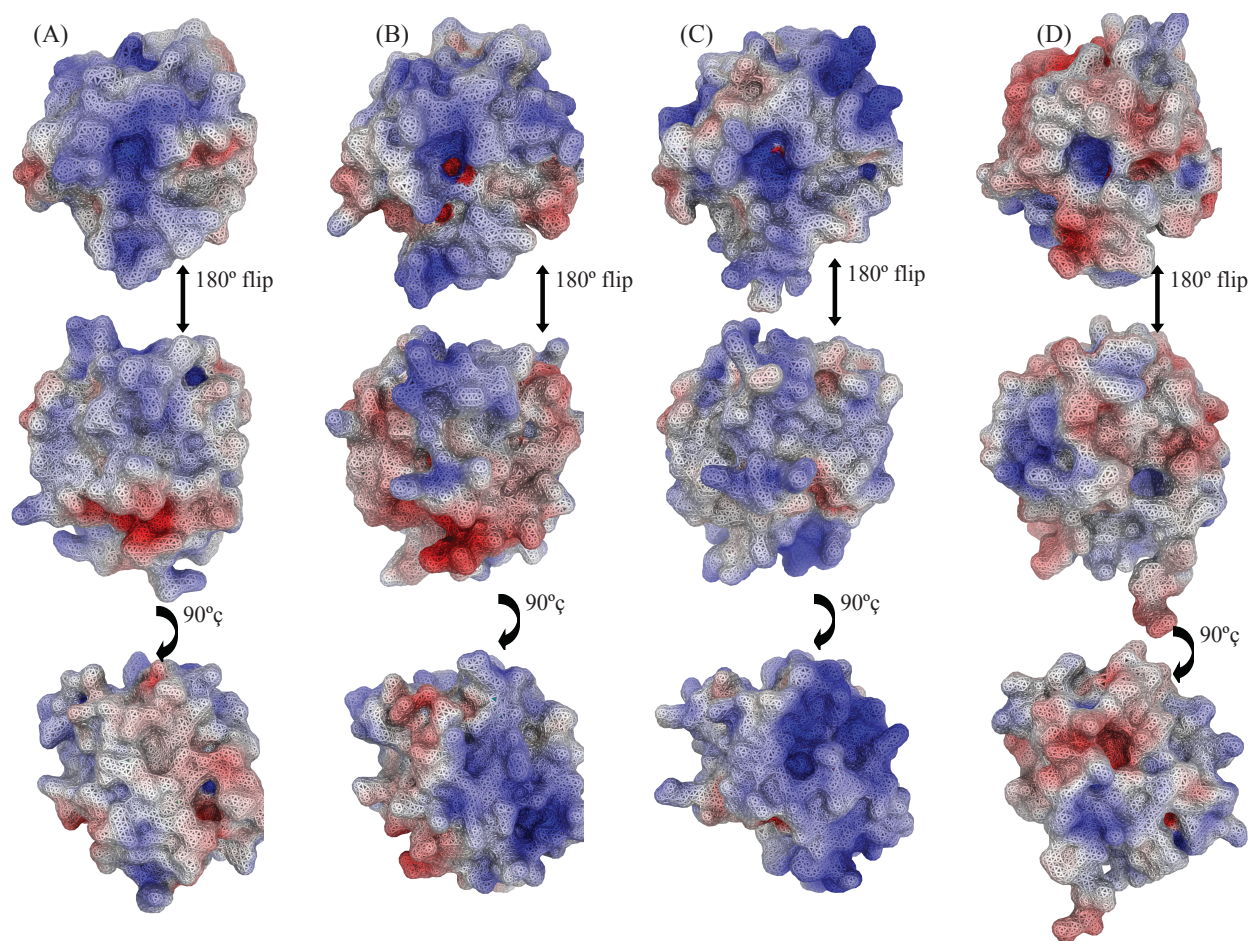


Figure 29: Differences in the electrostatic surface charges was obtained by PYMOL. (A) α D I-domain, (B) α X I-domain, (C) α M I-domain, and (D) α L I-domain. The structures were oriented to view the MIDAS (top); 180° vertical rotation (flip) to for sideview 1 (middle) and 90° clockwise rotation for sideview 2 (bottom). The electron potential charges (electrostatic surface charges) are in kilo-electron volts per mole

3.7 Characterization of α D I-domain, the ligand binding domain of leukocyte integrin α D β 2, affinity to divalent cations

3.7.1 Introduction

The ability of integrins to recognize and bind multiple ligands aids in integrin functional diversity. The ligand-binding activity of leukocyte integrins is regulated by conformational changes in the extracellular domains (Dransfield et al., 1992). The integrin–ligand interactions are dependent on the presence of divalent cations, such as Mg^{2+} ion, which is coordinated by residues in MIDAS of the α I domain and plays a key role in coupling between MIDAS and α I α 7-helix (Springer and Wang, 2004). Although divalent metal coordination geometry is well-studied at structural levels in many integrins (Day et al., 2002; Dransfield et al., 1992; Leitinger et al., 2000), the basis for which specific M^{2+} -ions augment integrin ligand recognition is poorly understood. In this study, in addition to the structural changes induced by selected metals, we used ‘in-solution’ affinity techniques such as isothermal titration calorimetry (ITC) and differential scanning fluorimetry (DSF) to characterize how metal ions (Mg^{2+} , Mn^{2+} , Ca^{2+} , Cd^{2+} , Co^{2+} , and Zn^{2+}) alter the stability of the α D I-domain and how they differ in their binding to MIDAS. The role and catalytic binding effects of individual metal ions are often distinct at their binding sites. For instance, while Mg^{2+} uniformly facilitates integrin ligand binding, Ca^{2+} generally inhibits it. Also, Mn^{2+} has been identified to universally enhance integrin interactions with their cognate ligands (Day et al., 2002).

As revealed in most α I-integrins, we hypothesize that the isolated α D I-domain will exhibit divalent cation-dependent ligand binding. We predict that metal ions will alter the stability of the α D-I domain fold in solution. Therefore, we expect a change in α D-I stability with a corresponding incremental increase in M^{2+} -ion concentration. To test this hypothesis, we performed a thermal

shift assay using differential scanning fluorimetry (DSF) to probe the α D I-domain stability profile of each divalent cation in varying concentrations.

Differential scanning fluorimetry (DSF) is a thermal melt experiment, which monitors protein unfolding in the presence of variety of ligands. The temperature at which, the α D I-domain unfolds, was measured by substantial increase in fluorescent intensity of a merocyanine dye, SYPRO orange (the excitation maximum is 472 nm, and the emission maximum is 570 nm). SYPRO orange has affinity with hydrophobic residues, which are exposed as the protein unfolds (Niesen et al., 2007) (Figure 30). The experiment was done using a real-time PCR instrument. Even though melting temperature is alternatively used to access protein stability, simple determination of the midpoint of the fully folded protein to unfolded state (T_m) is not a conclusive determination of protein stability. However, we employed this facile technique to determine the change in enthalpy of thermal unfolding of the α D I-domain at varying concentrations of different metal ions (Ca^{2+} , Mg^{2+} , Mn^{2+} , Cd^{2+} , Co^{2+} , and Zn^{2+}).

To determine the detailed insight into the binding energetics of the α D I-domain at the constant temperature, we performed isothermal titration calorimetry (ITC). ITC measures the heat change that occurs when two substances interact at constant temperature (Freire et al., 1990). ITC may help in describing the mechanism of protein-protein and/or protein-ligand interaction at the molecular level, through detailed characterization of the affinity, number of binding sites, and binding thermodynamics.

Each injection of a cation to the α D I-domain resulted in a heat pulse that was integrated with respect to time and normalized to generate a titration-fit curve. The titration curve represents the change in enthalpy (ΔH) versus the molar ratio of the cation to the α D I-domain (Figure 11). The resulting isotherm was fitted to a binding model to obtain the affinity of each cation to the α D I-

domain which is represented by dissociation constant (K_d) of binding (Velázquez-Campoy et al., 2004).

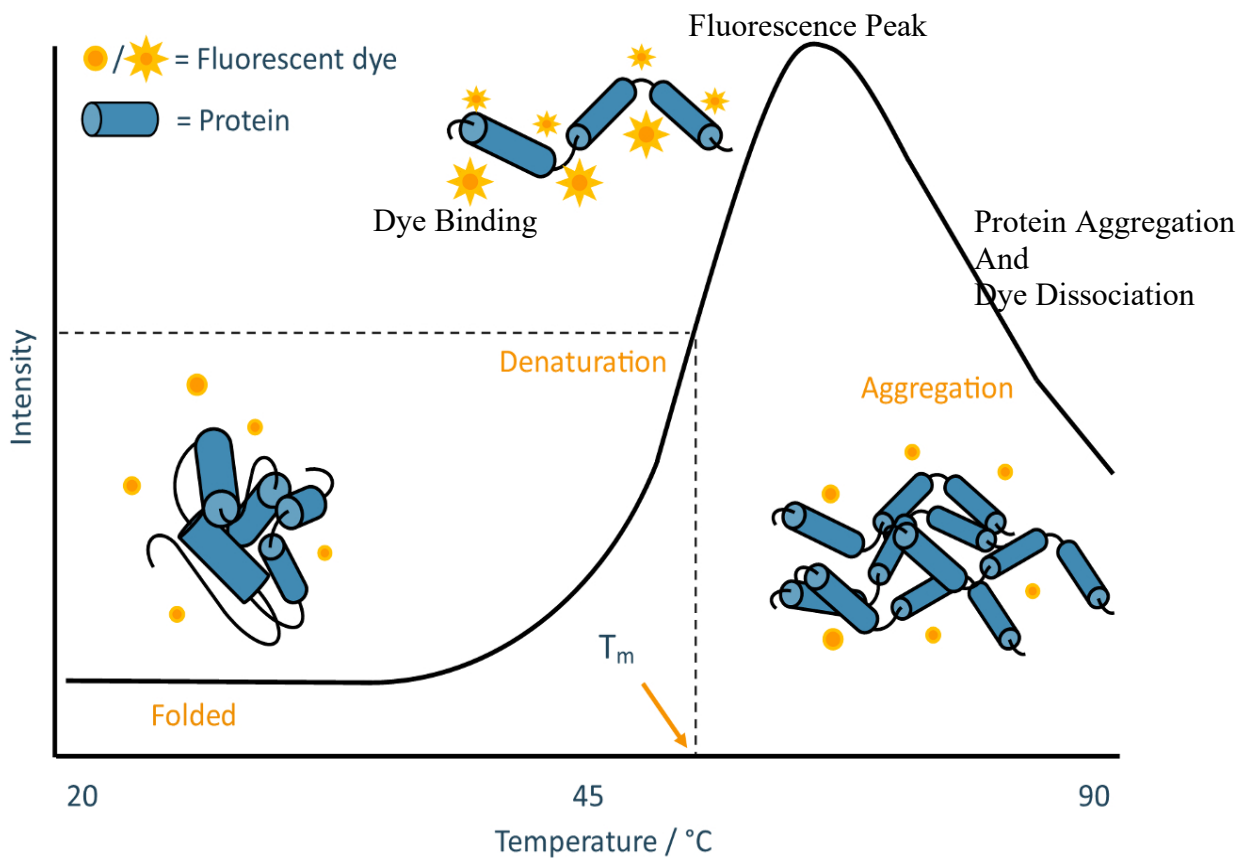


Figure 30: Schematic representation of thermal shift assay using DSF showing increase in fluorescence intensity due to dye binding to the hydrophobic residues of unfolded protein upon thermal denaturation. Adapted from (Bruce et al., 2019)

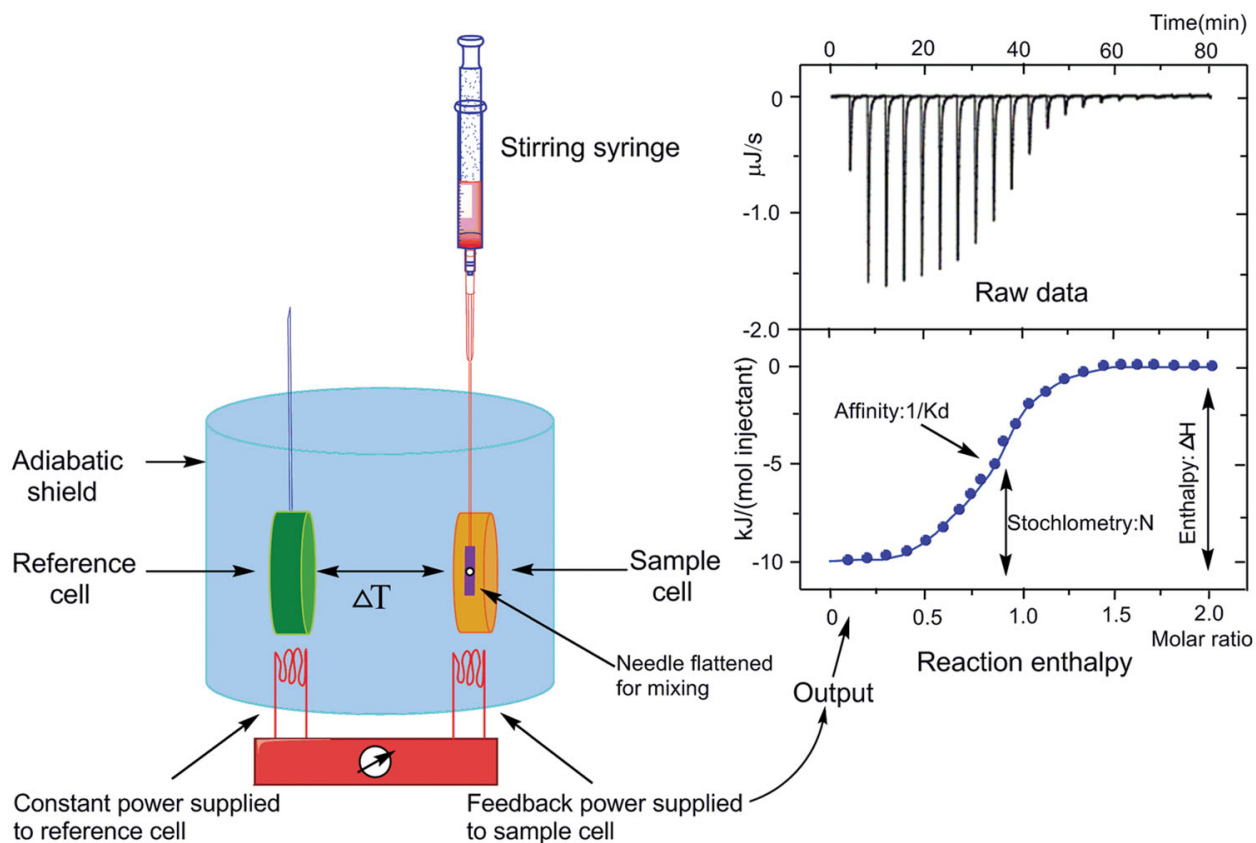


Figure 31: Representation of basic principle of ITC technology and experimental curves. Raw data shows the heat signature of ligand and analyte binding resulting from each injection of the ligand while the reaction enthalpy shows the titration curve generated from integration of heat signature with respect to time and fitted to a binding model (Adapted from Song (Song et al., 2015)).

Results

3.7.2 The α D I-domain stability is affected by M^{2+} -ion-binding

Mg^{2+} which is physiologically present at the MIDAS of leukocyte integrins is very important for the α I-domain activity (Emsley et al., 2000; Zhang and Chen, 2012). To determine whether the binding of cation alters the stability of the α D I-domain, we observed the thermal unfolding of the α D I-domain in the presence of a SYPRO orange dye at varying concentrations of different metal ions using DSF (Figure 31). For the α D I-domain binding to Mg^{2+} at increasing concentration ranging from 0–500 mM, the melting temperature of the α D I-domain protein elevated from 39.7 °C to 51.6 °C (Figure 33C). However, with increase in Zn^{2+} concentration, the melting temperature of the α D I-domain protein reduced from 41.8 °C to 29.6 °C. The initial, final and change in melting temperature (T_m) for each M^{2+} - α D I-domain binding is reported in Table 7. A gradual increase in the T_m was observed as the MIDAS was increasingly occupied by each M^{2+} except Zn^{2+} (Figure 33A, C, E, 34A, C, E). It should be noted that in all M^{2+} - α D I-domain interactions, the T_m plateaued at around 100 mM after reaching saturation except Mg^{2+} , which demonstrated a continuous increase in T_m even after 1000 mM (Figures 33C). This means that the α D I-domain- Mg^{2+} interaction did not reach saturation. In all, the binding of Mg^{2+} increased the stability of the α D I-domain protein most while Ca^{2+} binding had the least stability effect on the α D I-domain with ΔT_m of approximately 12 °C and 6 °C, respectively. As stated earlier, the binding of Zn^{2+} drastically destabilize the α D I-domain even at the least $[Zn^{2+}]$ of approximately 1 μ M. The α D I-domain interaction with Mg^{2+} , Mn^{2+} , Ca^{2+} , and Co^{2+} displayed a better fit for bi-phasic transition (red-line) compared to mono-phasic fit (blue line). Conversely, the interaction of Cd^{2+} , and Zn^{2+} with α D I-domain showed a mono-phasic binding profile only.

To confirm that the Hofmeister or lyotropic effect via increasing the ionic strength did not contribute to the increase in the T_m of the α D I-domain, we monitored the α D I-domain thermal unfolding at increasing sodium chloride concentrations (0–500 mM). As shown in Figure 32, the T_m of the α D I-domain remained consistent, which suggest that the alterations in the α D I-domain thermal stability observed was solely due to the divalent cation binding.

Table 7. The melting temperatures obtained for the α D I-domain- M^{2+} -ion binding experiment via DSF

M^{2+} -ion	Initial T_m (°C)	Final T_m (°C)	ΔT_m (°C)	Midpoint T_m (°C)
Mg^{2+}	39.7	51.6	11.90	45.41
Mn^{2+}	39.7	46.2	6.50	46.31
Cd^{2+}	41.1	47.3	6.20	44.23
Ca^{2+}	39.6	45.5	5.90	42.66
Co^{2+}	41.2	47.8	6.60	44.57
Zn^{2+}	41.8	29.6	-12.2	34.25

We further analyzed the DSF data using the Van't Hoff equation and plot (Figure 33B, D, F and Figure 34B, D, F), which informs about the temperature dependence of the equilibrium binding constant. Here, we examined the Van't Hoff-linear dependence of T_m ($1/T_m$) to the ligand concentration ($\ln[M^{2+}]$) using the Equation (1) below (Shrake and Ross, 1988).

$$\Delta H_{\text{Van't Hoff}} = nRT \ln[M^{2+}]_0 + c \quad (1)$$

where $\Delta H_{\text{Van't Hoff}}$ is the temperature-independent enthalpy of the α D I-domain unfolding event, R is the gas constant, T is the temperature (Kelvin), n is the number of binding sites, and c is constant.

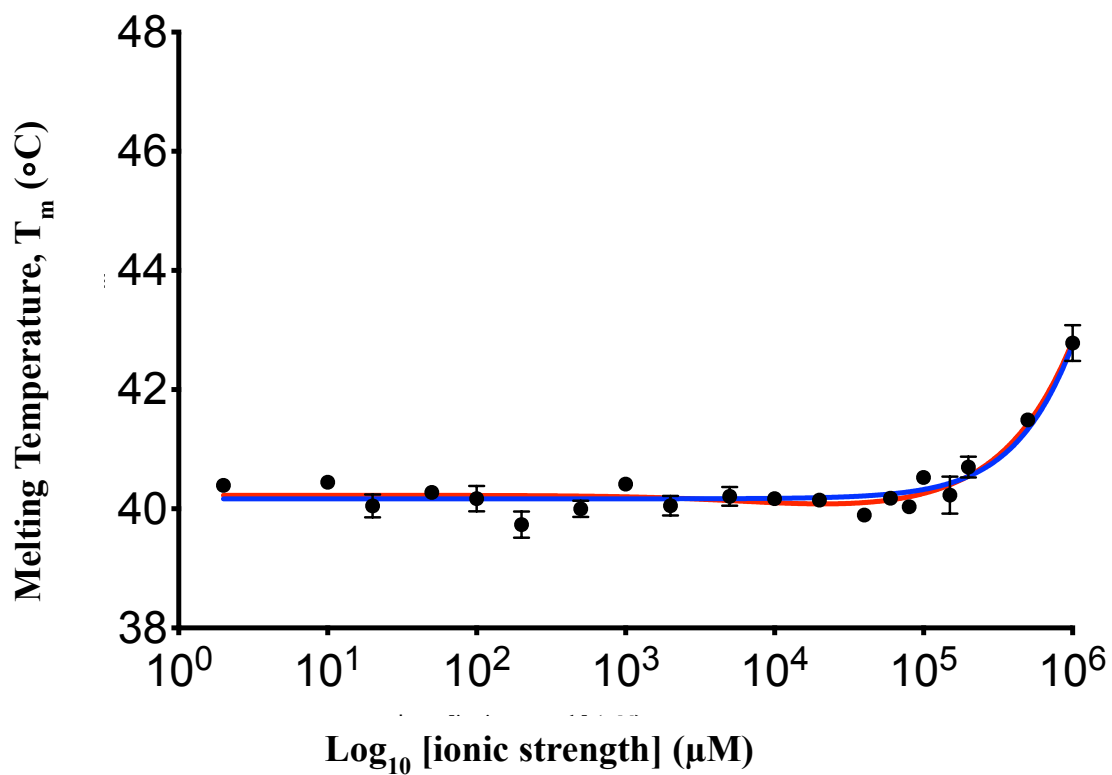


Figure 32: the Hofmeister or lyotropic effect via increasing the ionic strength did not contribute to the increase in the T_m of the α D I-domain. The T_m of the α D I-domain did not change with an increasing concentration of sodium chloride.

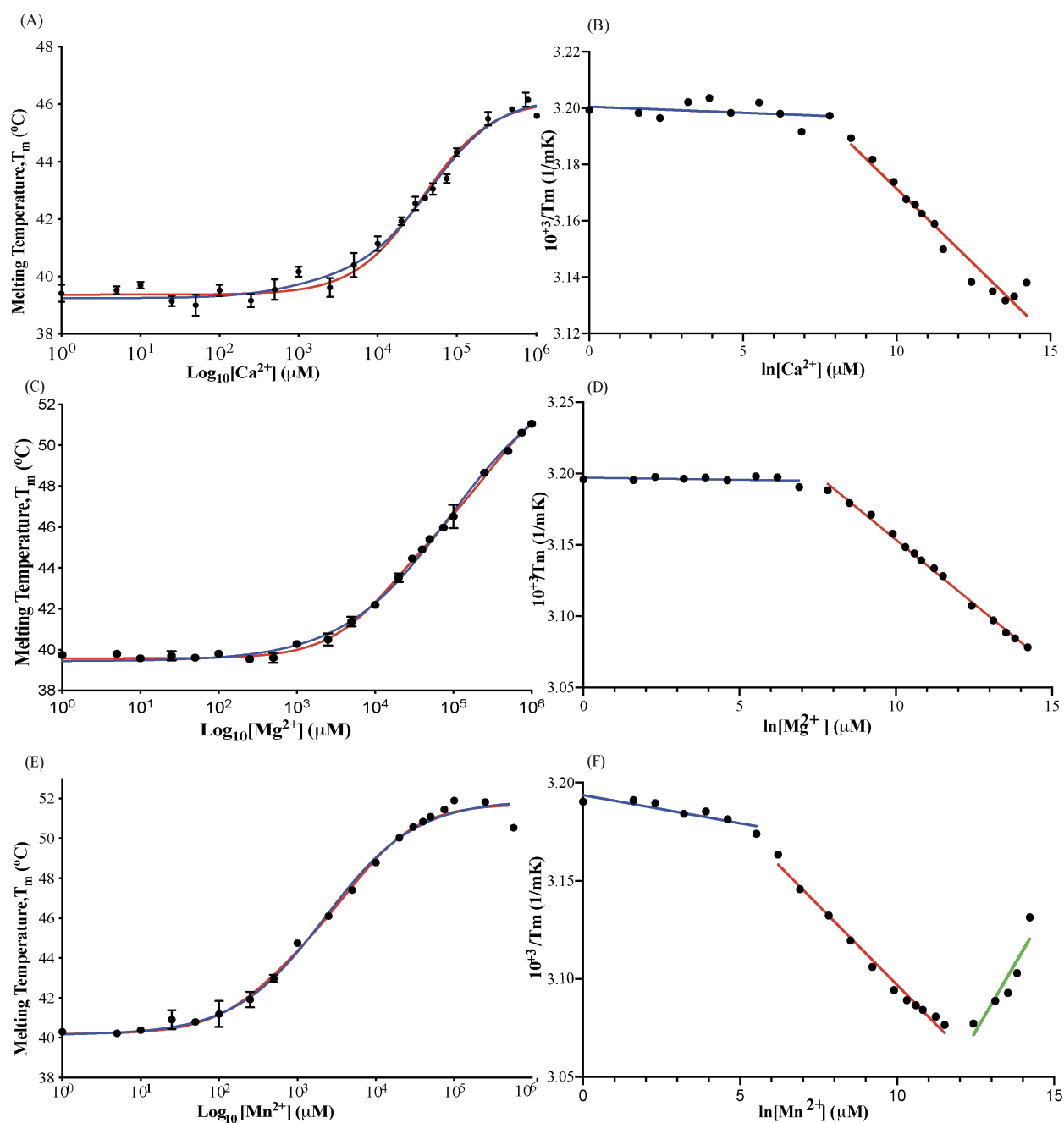


Figure 33: M^{2+} -binding affect the stability of the αD I-domain and is associated with the structural alteration of the αD I-domain after MIDAS saturation. Differential T_m change in response to M^{2+} concentration from DSF denaturation were plotted and fitted to monophasic (blue line) or biphasic transition (red line); (A) Ca^{2+} (B) Mg^{2+} (C) Mn^{2+} . Plots of Van't Hoff linear dependence derived from the differential scanning fluorimetry for the αD I-domain in increasing concentration of (D) Ca^{2+} , (E) Mg^{2+} , and (F) Mn^{2+} are shown.

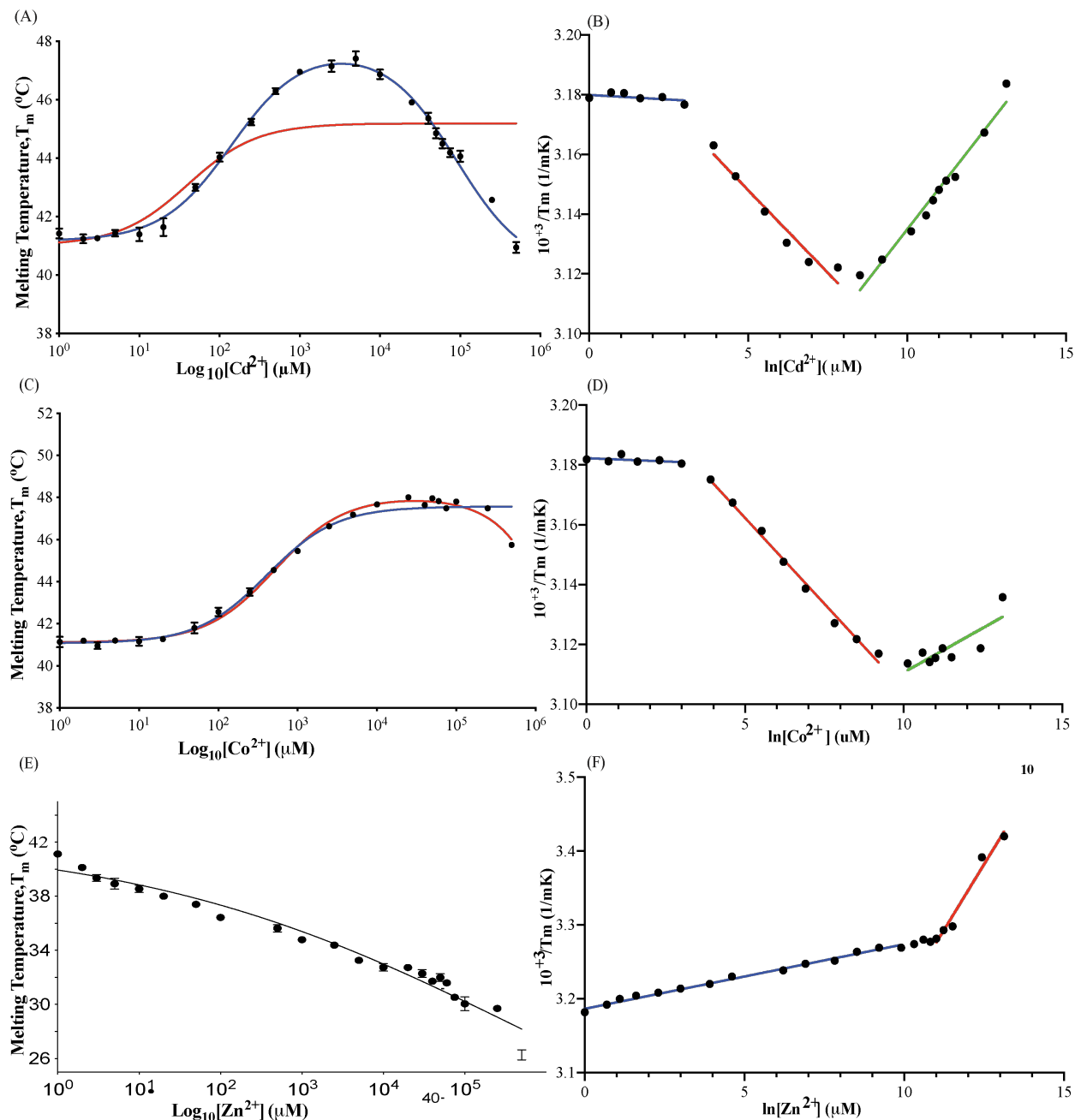


Figure 34: M^{2+} -binding affect the stability of the αD I-domain and is associated with the structural alteration of the αD I-domain after MIDAS saturation. Differential T_m change in response to M^{2+} concentration from DSF denaturation were plotted and fitted to monophasic (blue line) or biphasic transition (red line); (A) Cd^{2+} , (B) Co^{2+} , and (C) Zn^{2+} are shown. Plots of Van't Hoff linear dependence derived from the differential scanning fluorimetry for the αD I-domain in increasing concentration of (D) Cd^{2+} , (E) Co^{2+} , and (F) Zn^{2+} are also shown.

3.7.3 Thermodynamics of divalent cation affinity to the α D I-domain

We examined the binding effects and affinity of six metal ions, Mg^{2+} , Mn^{2+} , Ca^{2+} , and Zn^{2+} , to the MIDAS of the α D I-domain, using isothermal calorimetry titration. To check that the ITC system is working well, the final SEC purification buffer was titrated against the same buffer. Additionally, as a negative control, the metals were titrated to the SEC buffer to ensure that this titration does not bring forth significant change in enthalpy. Figure 35-inserts show each individual injection heat, normalized by the amount of M^{2+} injected, as a function of the molar ratio of the α D I-domain in the ITC sample cell. Calorimetry titration curves were further fitted to a binding model ($n=1$) via the automated MicroCal PEAQ-ITC analysis software, yielding the dissociation constant (K_D) and enthalpy ($\Delta H^0_{\text{binding}}$) (Figure 35A-D). The binding affinities of the M^{2+} -ions to the α D I-domain are highest for Zn^{2+} at 25.12 μM , and weakest for Ca^{2+} at 1600 μM (Table 8). The affinity difference obtained confirms the suggestion that each metal cation may perform specific and different roles in integrin-ligand interaction. For instance, Ca^{2+} -domain α D I-domain interaction was mainly driven by entropy while the binding of Mn^{2+} was predominantly driven by enthalpy. Binding of Mg^{2+} to α D I-domain was driven equally by both enthalpy and entropy. The thermodynamics parameters—Gibbs free energy (ΔG), enthalpy (ΔH), entropy (ΔS) and dissociation constant (K_D)—of M^{2+} -ions affinity to the α D I-domain as determined by ITC are reported in Table 8.

Table 8: Values of thermodynamics parameters—Gibbs free energy (ΔG), enthalpy (ΔH), entropy (ΔS) of M^{2+} -ions affinity to the αD I-domain. The number of binding site (n) used for fitting was 1.

αD I-domain	M^{2+}	ΔG (kcal/mol)	ΔH (kcal/mol)	$-T\Delta S$ (kcal/mol)	K_D (μM)
	Mg^{2+}	-4.72	-1.79	-2.94	347 ± 17.8
	Mn^{2+}	-6.186	-6.483	0.298	29.23 ± 3.85
	Ca^{2+}	-3.82	-2.19	-1.62	1600 ± 104
	Zn^{2+}	-6.446	-1.290	-5.156	25.12 ± 2.14

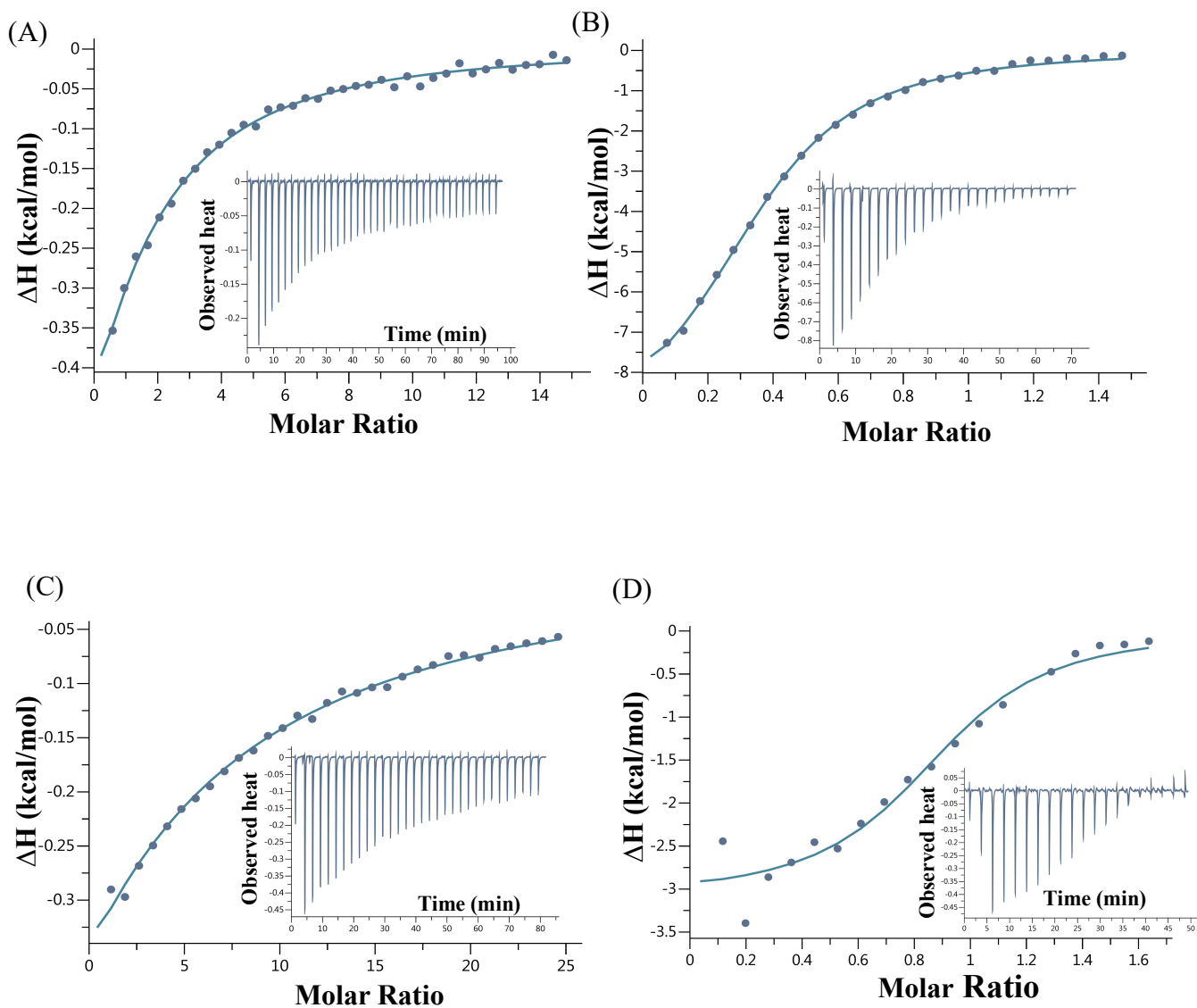


Figure 35: The ITC plots represent the change in the enthalpy during metal ion titration (A) Mg^{2+} , (B) Mn^{2+} , (C) Ca^{2+} , and (D) Zn^{2+} , –to the αD I-domain. The plots were fitted using $n=1$

3.8 Functional characterization of α D β 2 with the β 2-specific mAbs and M^{2+} ions

3.8.1 Binding of α D β 2 to E-IgM-iC3b (Cell based assay by Zeinab Moussa)

Although several reports have shown that α D β 2 binds to similar ligands of complement receptors CR3 and CR4 (e.g., fibrinogen), human α D β 2, when expressed recombinantly on cell surfaces, has never been shown to bind complement molecule iC3b. To assess the affinity of α D β 2 to iC3b, therefore identifying α D β 2 as a part of the complement system, rosetting assay with HEK293 cells was conducted by a colleague in our laboratory (Zeinab Moussa). In this rosetting assay, human CR3 and CR4, well-characterized iC3b integrin receptors, were used as positive binding controls. The rosetting assay showed strong rosette formation by CR3 in Mg^{2+}/Ca^{2+} (basal condition), which was further enhanced in Mn^{2+} condition, the universal activating ion of all integrins (Figure 36A). On the contrary, CR4 (human α X β 2), showed weak rosetting in Mg^{2+}/Ca^{2+} (basal condition) and its strong rosette could be detected in Mn^{2+} (Figure 36A). Human α D β 2 binds to iC3b-opsonized erythrocytes weakly in Mg^{2+} and strongly in Mn^{2+} , similarly to CR4 but not CR3. Next, we tested the expression and affinity of the interspecies hybrid chicken β 2/human α D complex. The hybrid C β 2/h α D was expressed as efficiently as the h α D β 2 and did bind iC3b-opsonized erythrocytes in the Mg^{2+}/Ca^{2+} (basal condition) (Figure 36B).

3.8.2 Functional characterization of α D β 2 with the β 2-specific mAbs

We also examined the adhesiveness of integrin α D β 2 in different conformation stabilizing or reporting antibodies (mAb). Activating monoclonal antibody CBR-LFA1/2 binds to the EGF-3 of the β 2-subunit (residues L534, F536, R541, H543, and F546) and induces integrin extension (Kim et al., 2003; Lu et al., 2001b). Additionally, MEM148 and m24 monoclonal antibodies, which both probe the integrin head piece opening bind to the hybrid domain (residues H370, Q373, P374) and

the β 2-subunit (residues R122 and E174), respectively (Tang et al., 2005). TS1/18 mAb is an allosteric inhibitor that binds to an epitope on the β 2 I-domain (residues R133 and Q332) and locks β 2 I-domain into the closed conformation (Lu et al., 2001b). In this current study, α D β 2 complexed with MEM148, CBR-LFA1/2 and both at the same time showed a significant progressive increase in rosetting and binding E-IgM-iC3b while Mn^{2+} -induced α D β 2 affinity was highest (Figure 36C, D). Nonetheless, with increasing concentration of TS1/18, Mn^{2+} -induced affinity of α D β 2 is progressively diminished in a dose dependent manner, giving an IC_{50} of 2.1 μ g/mL (Figure 36B).

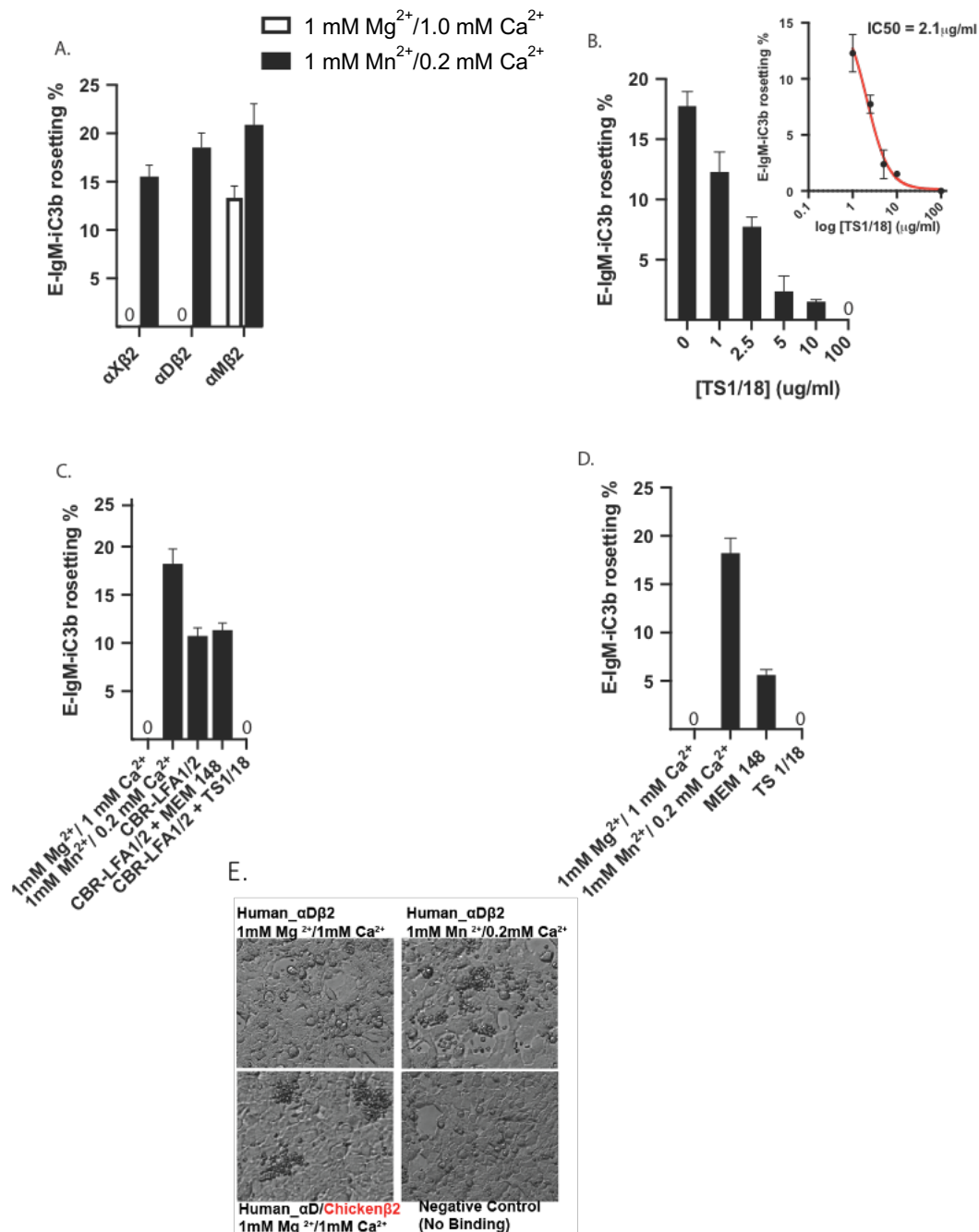


Figure 36: E-IgM-iC3b binding assay and rosetting micrographs. (A) Human β2-containing CR3, CR4, and αDβ2 binding to iC3b-opsonized sheep erythrocytes (B) inhibitory effect of TS1/18 was probed in a dose dependent manner and showing IC₅₀ of 2.1 μg/ml (C, D) effect of conformation-stabilizing mAbs on the αDβ2 affinity. (E) Representative micrographs showing E-IgM-iC3b rosetting

3.8.3 Differential effect of M^{2+} -ions in $\alpha D\beta 2$ ligand binding

Earlier studies with Mg^{2+} , Ca^{2+} , and Mn^{2+} ions have shown distinct effects on the overall integrin function, including its propensity to bind ligand—suggesting roles of M^{2+} -ions in allosteric regulation of integrin structural changes. Also, given that our ITC experiment with the isolated αD I-domain showed that different Mn^{2+} ions have different effects on the stability and affinity of the integrin protein, we tested whether Mg^{2+} , Ca^{2+} , Mn^{2+} , Cd^{2+} , Ni^{2+} , Cu^{2+} , Zn^{2+} , and Co^{2+} showed any affinity regulation in $\alpha D\beta 2$ ligand (fibrinogen) binding. As shown in Figure 37, Cd^{2+} , Ni^{2+} , Co^{2+} in three different concentrations, and Zn^{2+} progressively enhanced $\alpha D\beta 2$ affinity to fibrinogen. Due to low solubility at pH 7.4, only 100 μM concentration of Cu^{2+} was used in our assays.

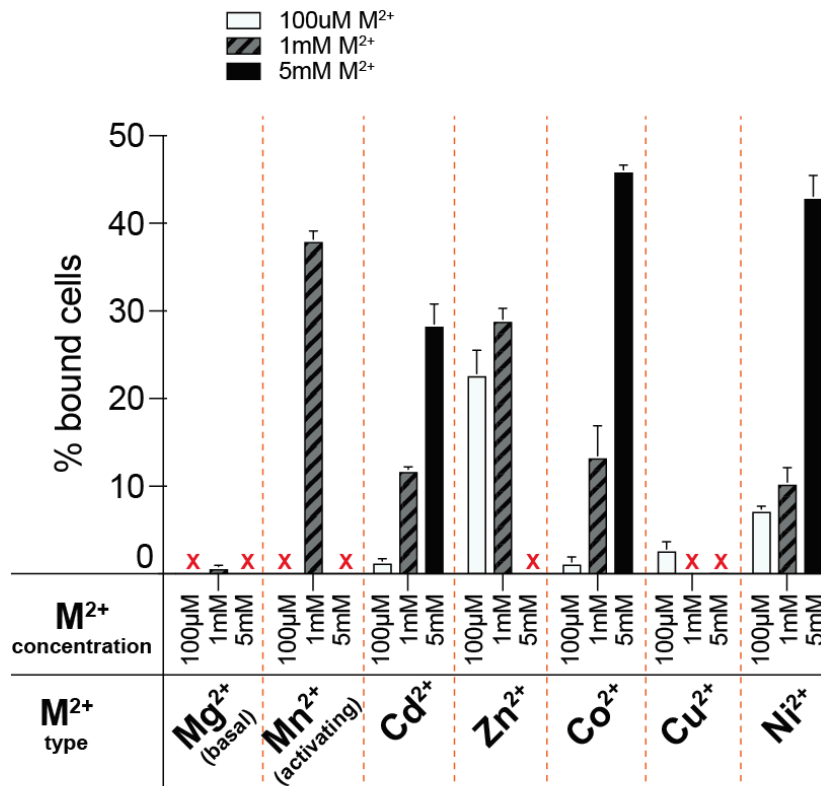


Figure 37: Differential effect of different M^{2+} -ions in three different concentrations are probed in our fibrinogen binding assays

4. DISCUSSION

The β 2-integrin family members share the same β -subunit (CD18) and differ by their α -chains, which include CD11d (α D β 2), CD11c (α X β 2, CR4), CD11b (α M β 2, Mac-1, CR3), and CD11a (α L β 2, LFA-1). All four members of the β 2-integrin family play vital roles in immunity and mediate leukocyte functions such as adhesion, migration, and phagocytosis. As a result of their critical role in leukocyte function, β 2-integrin deficiency or functional defects cause an immunodeficiency syndrome called the leukocyte adhesion deficiency type-I(LAD-I) (Fagerholm et al., 2019; Fischer et al., 1988). α D β 2, the most recently discovered member of the β 2-integrin subfamily, has low to moderate expression in circulating leukocytes and its expression is upregulated on inflammatory macrophages upon cellular activation. For example, α D β 2 is the most robustly and abundantly expressed receptor in women who suffer from diet-induced obesity (DIO) (also sharing the same biology in rodent model) (Thomas et al., 2011). Such pivotal roles of α D β 2 discussed in Chapter 1, suggest that α D β 2 could be an important drug target for α D β 2-dominant macrophage pathologies. However, among all four members of the β 2-integrin, α D β 2 has not been extensively characterized in humans yet. The objective of my work was to address the gap in knowledge between α D β 2 and its homologous β 2-integrins with regards to their structural features and biochemical/functional properties such as ligand affinity and binding effects of metal cations.

Herein, we isolated, purified, and characterized the α D I-domain, the major ligand binding site of this protein. Successful growth of large three-dimensional crystals was achieved using the hanging drop vapor diffusion technique. Screening of over 300 commercial reagents helped identified several conditions, some of which grew X-ray diffracting crystals upon optimization. Initial crystallization screening with protein concentration below 40 mg/mL did not yield any

crystals. This suggests that very high protein concentration was key in obtaining supersaturated α D I-domain solution. In this study, using the same crystallization conditions, the best crystals were obtained at protein concentrations above 50 mg/mL. Compared to the crystallization of other members of the β 2-integrins (α X-1N3Y, α M-1IDO, and α L-1LFA), which were all crystallized at protein concentration around 20 mg/mL, crystallization of the α D I-domain requires very high protein concentration. On the contrary, the α D I-domain and α L I-domain crystals grew to their final sizes between 3-7 d while that of α X and α M took about 2-3 weeks (Lee et al., 1995; Qu and Leahy, 1995; Vorup-Jensen et al., 2003).

Co-crystallization of proteins with metals ions and other ligands has been reported to yield better crystallization results than crystallization of the proteins alone. The metal ions or ligands are expected to stabilize the protein and the stable form tends to crystallize better than the free, non-stable form (McPherson, 2004). In this study, co-crystallization of α D I-domain with selected metal ions (M^{2+} -ions) produced better morphology and appearance (Figure 17). Based on the two crystal structures solved in this study (PEG3350 crystal and Malic acid crystal), co-crystallization of α D I-domain with magnesium generated a better-quality structure with a resolution of 1.2 Å (Table 5). This result may confirm the assertion that Mg^{2+} ion (and other metal ions) stabilizes the protein. To generate Ca^{2+} -bound crystals, I set up extensive amount of trials, all of which failed. In the literature, binding of the Ca^{2+} to the α M I-domain and our recent binding studies on Ca^{2+} - α X I-domain affinity independently showed that Ca^{2+} binding is dominantly driven by entropy—most probably increased structural entropy (Ajroud et al., 2004). Therefore, I predict that my crystallization trials failed due to Ca^{2+} -dependent enhanced structural heterogeneity.

As stated in Section 3.3, the α D I-domain structure adopts the G protein like α/β Rossmann fold distinguished by alternating amphipathic α -helices and hydrophobic β -strands. As observed

in all α I-domains of β 2-integrins, five parallel and one short antiparallel beta-strands from a central sheet that is surrounded by seven alpha helices (Lee et al., 1995).

Although the overall structures of the three-known leukocyte α I-domains (α L, α M, and α X) are similar to that of α D I-domain, there are few differences in critical regions, which may affect the ligand binding of each protein. For instance, in the ligand binding region around the MIDAS and the α I α 7-helix, there are differences in residue-charges and hydrophilicities between the α D I-domain and other α I-domains (Figure 26 and 27), which may have contributed to the differences in the electrostatic field generation on the α I-domain surfaces (Figure 29A-D). Furthermore, there are two substitutions of non-polar residues at the conserved MIDAS region for α L I-domain. Met-140 and Leu-142 in α L were changed to Gly 142 and Ile-144 in α D I-domain (Figure 27). These alternate replacement of charged residues with hydrophobic residues may have important implications concerning the ligand-binding specifications of α D β 2, α M β 2 and α X β 2 (Table 9), therefore future chimeric studies would be central to further elucidate how these differences contribute critical difference in ligand selectivity of these α I domains on the same protein scaffold.

Table 9. Significant variations in the amino acid residues around the MIDAS region of α D I-domain and its closest homologues

α I-domain	Amino acid residues around the MIDAS region
α D I-domain	Met-132, Lys-205, Leu-207, Phe-209, Gln-243, Tyr-245 and His-272
α M I-domain	Ser-144, Leu-206, Arg-208, His-210, Glu-244, Phe-246 and Asp-273
α X I-domain	Gln-131, Gln-204, Phe-206, Tyr-208, Lys-242, Glu-244 and Leu-271

Also, in the structures of α D, α X and α M I-domains, the C-terminal α I α 7-helix is shown to be well packed, forming a close association with the body of the domain through hydrophobic residue contacts (Figure 28B). However, in the α L I-domain, the α I α 7-helix has very low propensity (Figure 28B), and number of NOEs used as constrain in NMR structure calculation for the α L I-domain has significantly reduced (Legge et al., 2000). Simply, these characteristics of the α L I-domain may endow its α I α 7-helix highly flexible nature. (Figure 28A, B). Furthermore, the helical propensity of the α 7-helix varies significantly among all four α I-domains (Figure 28A, B). This suggests that differential local dynamics and conformational variability exist in the C-terminal especially at the α 7-helix, which will, partially if not fully, contribute ligand-binding dynamics at the MIDAS site. The difference in the isoelectric points (pI) of all the four α I-domains (Figure 28B-inserts) may also contribute to the different molecular steering of ligands as well. Collectively, these variations in the α I-domains could create the difference in their ligand-specificities due to different conformational dynamics, and concomitantly results in different functions on the same leukocyte cell type.

Integrins are known metalloproteins, which means that they function in the presence of metal ions to modulate their physiological functions including ligand affinity and conformations (Hall and Slack, 2019). In this crystallographic study, it has been established that the introduction of M^{2+} -ions affects the geometric arrangement of the MIDAS residues. Our two crystal structures with and without Mg^{2+} has shown that when free of Mg^{2+} ion, MIDAS is occupied by two water molecules and adopts the closed state geometry. Introduction of Mg^{2+} resulted in a limited structural change in the MIDAS including gain of an extra water coordination and rearrangement of the two invariant MIDAS aspartate residues (D139 and D241). As described earlier, the D241 rotamer pivots upon Mg^{2+} -binding, which links D241 to Mg^{2+} through ionic coordination.

Subsequently, the D139 rotamer also pivots upon Mg^{2+} -binding causing a link between Mg^{2+} and D139 through invariant water coordination, which helps stabilize the carboxylates of residue D139. This MIDAS geometric reconfiguration observed in all α I-domains may contribute priming α I-domain for rapid activation on the leukocyte surface.

Recent study in our lab showed that divalent cation binding on the α X I-domain structure resulted in a change in its global stability. In this current study, the change in thermal stability of the α D I-domain in varying concentration of Mg^{2+} , Mn^{2+} , Ca^{2+} , Cd^{2+} , Co^{2+} , and Zn^{2+} was assessed using DSF. The results were very consistent with our initial experiment with the α X I-domain (not shown); M^{2+} -binding significantly affected the stability of the α D I-domain structure. The different effects observed for each metal ion can be attributed to the alteration of the α D I-domain structure with a different saturation profile. In our DSF study, the α D I-domain stability is linked to its temperature dependent Gibbs free energy of unfolding, ΔG_u , which decreases with increasing temperature until equilibrium is reached where the concentrations of folded and unfolded proteins are equal (Niesen et al., 2007). Briefly, gradual increment of Mg^{2+} , Mn^{2+} , Ca^{2+} , Cd^{2+} , and Co^{2+} concentration caused an increase in the T_m (Figure 33A, C, E and Figure 34A, C, E) suggesting that each of these metal cations have significant stabilizing effect on the α D I-domain structure. It should be noted that the stabilizing effect of these M^{2+} -ions upon binding to the α D I-domain is proportional to the concentration and affinity of the M^{2+} -ions (Matulis et al., 2005; Senisterra et al., 2006). Interestingly, the binding of Zn^{2+} ion to the α D I-domain (Figure 34F) destabilizes the protein drastically. This means Zn^{2+} may negatively affect the α D I-domain ligand binding due to influencing 3D-fold of the α I domain. Indeed, high-dose Zn^{2+} showed an impaired leukocyte function in cell-based studies (Chandra, 1984). The Hofmeister or lyotropic effect, via increasing the ionic strength, nonetheless did not alter the thermal stability of α D I-domain (Figure 32),

suggesting the observed thermal stability alterations to be an exclusive consequence of the M^{2+} -MIDAS assembly.

Normally, temperature independent Van't Hoff enthalpy plots show linear relations between $\ln[\text{ligand}]$ and $1/T_m$, and the number of linear sections reveals multiphasic transitions (Shrake and Ross, 1988). In this work, temperature independent Van't Hoff enthalpy plots calculated from DSF thermogram interpolations displayed two linear Mg^{2+} , and Ca^{2+} concentration ranges for αD I-domain (Figure 33B, D) while Mn^{2+} (Figure 33F), and Cd^{2+} , and Co^{2+} displayed three linear plots (Figure 34B, D). This data suggests that at least two distinct conformational states, if not more, co-exist in solution, with M^{2+} altering the conformational equilibrium constant or the relative concentration of these states.

We also extracted the thermodynamic parameters of M^{2+} -ion binding events in αD I-domain. The M^{2+} -ion- αD I-domain affinities probed in this study were in μM range and thus weak in measurable range in the order of $Zn^{2+} > Mn^{2+} > Mg^{2+} > Ca^{2+}$. These measurements coincide with the absolute binding free energy calculations for Mn^{2+} , Mg^{2+} , and Ca^{2+} binding to the αL I-domain (Sebastian et al., 2006) and the experimental measurements for αL , αX , and αM I-domains (Baldwin et al., 1998; Vorup-Jensen et al., 2007b). In all the titration experiments, systemic alteration of divalent cation affinity was observed and with significant variability in entropy contribution (Table 8). These observations may be attributed in part to the different electronegativity of the individual metal ions, although they all have charge of +2. Also, the high electronegativity of Cd^{2+} and Mn^{2+} , 1.69 and 1.5 Pauling units, means the ionic tethering of these cations to the MIDAS is potentially very effective. Although, the affinity of Mg^{2+} was driven by both enthalpy and entropy, its ionic tethering to the MIDAS is relatively effective compared to Cd^{2+} and Mn^{2+} due to its relatively high electronegativity (Pauling unit of 1.31).

Interestingly, the detected binding enthalpy of the Ca^{2+} to MIDAS in our titrations and previous studies (Ajroud et al., 2004; Vorup-Jensen et al., 2007b) is marginal, and Ca^{2+} -affinity is mainly driven by the entropy rather than enthalpy. Due to the low electronegativity of Ca^{2+} (Pauling unit of 1), its ionic tethering to MIDAS by the electrostatic Ca^{2+} -steering or molecular diffusion is potentially less effective in comparison to ionic tethering of Mg^{2+} , Mn^{2+} , and Zn^{2+} .

Complement system consists of firmly organized and regulated network of proteins that has essential role in host defense and inflammation. Complement receptors compose an important link between innate and adaptive immune system. Amongst these receptors, $\beta 2$ -integrins, $\alpha\text{M}\beta 2$ (CR3), and $\alpha\text{X}\beta 2$ (CR4) have been the subject of several investigations for a better understand of their function to serve as potential therapeutic targets (DMSc and Kusuya Nishioka, 1998; Xua et al., 2017). In this study, we are reporting a third member of the $\beta 2$ -integrins family, $\alpha\text{D}\beta 2$, as a part of the complement system proven by its binding to the complement system protein, iC3b. $\alpha\text{D}\beta 2$ expressed on HEK293 cell surfaces were shown to bind to IgM-iC3b coated sheep erythrocytes and forms rosettes (Figure 36). Similar to the adhesion characteristics of CR3 and CR4, the adhesiveness of $\alpha\text{D}\beta 2$ to E- IgM-iC3b were differentially modulated by different conformation stabilizing antibodies (Figure 36D, E), which raises the possibility of $\alpha\text{D}\beta 2$ as a fifth complement receptor. However, the exact site of ligand binding of $\alpha\text{D}\beta 2$ to iC3b is still to be determined.

$\alpha\text{D}\beta 2$ has been identified as fibrinogen receptor (Gahmberg et al., 1997; Hyun et al., 2009) which means fibrinogen is a ligand for $\alpha\text{D}\beta 2$. Our αD I-domain- M^{2+} binding experiments with DSF and ITC revealed differential binding effect of these M^{2+} -ions on the isolated αD I-domain. A colleague in our lab (Zeinab Mousa), therefore tested the regulatory effect of these M^{2+} -ions on the affinity of overall $\alpha\text{D}\beta 2$ -fibrinogen binding (Figure 37). The results from this study agree with my ITC result that different M^{2+} -ions distinctly regulate the affinity of $\alpha\text{D}\beta 2$ -ligand

binding. This confirms the suggested role of M^{2+} ions in allosteric regulation of integrin structural changes. That is, M^{2+} -ion differentially shifts the conformational equilibrium and structural dynamics of the α D I-domain between low and high-affinity states in our cell-based assays.

5 CONCLUSION AND FUTURE PROSPECTS

5.1 Conclusion

In the last decade, several studies conducted to probe for potential therapeutic targets for the treatment of autoimmune conditions has been focused on $\beta 2$ integrins. Evidence gathered from these studies place $\beta 2$ integrins at the center of the balance between immune priming and tolerance (Celik et al., 2013; Harris et al., 2013; Jelcic et al., 2015; Krueger et al., 2008). Specifically, $\alpha D\beta 2$, which is the most recently discovered member of the $\beta 2$ -integrin family, plays pivotal roles in autoimmune pathologies including atherosclerosis and obesity (Aziz et al., 2017; Miyazaki et al., 2008; Miyazaki et al., 2014). These facts suggest regulation of the $\alpha D\beta 2$ activation state could emerge as a drug target strategy for the $\alpha D\beta 2$ -dominant macrophage pathologies.

The αI -domain is the major ligand-binding site of $\beta 2$ -integrins and has become one of the main targets to the development of integrin drug-related antagonists. Because αI -domain serves as the key molecular switch in integrin activation, structural and functional studies on αI -domains have been widely accepted to represent what is occurring on the intact integrins (Kollmann et al., 2014; Shimaoka et al., 2003a).

The current study focused on the three-dimensional structure determination of αD I-domain and its functional and biochemical characteristics in the presence of divalent cations. We report the first crystal structure of the αD I-domain, the ligand binding site of integrin $\alpha D\beta 2$. The αD I-domain proteins were crystallized using the hanging drop vapor diffusion method at 4 °C in six different M^{2+} -ions. Crystals grown in PEG3350 (co-crystallized with Mg^{2+}) and malic acid precipitants yielded very high resolutions of 1.2 Å and 1.32 Å, respectively, and the structures were successfully determined using the molecular replacement method. The Mg^{2+} co-crystallized structure had a single molecule located in the asymmetric unit of the crystal while the malic acid

crystal had two molecules per asymmetric unit. The two structures have different cell constants, and the overall structural difference between the two different lattices are concentrated around the helix-triad. In the Mg^{2+} -free αD I-domain structure, the MIDAS is occupied by two water molecules and adopts the close state conformation. However, in the Mg^{2+} -containing αD I-domain structure, an additional water molecule forms hydrogen bond with the Mg^{2+} and causes geometric reconfiguration of the MIDAS residues. Interestingly, our initial analysis of the other structures obtained from co-crystallization with other M^{2+} ions showed no structural difference compared to that of Mg^{2+} . The αD I-domain structure shares similar structural features with the two closest homologous, αX and αM I-domains. Comparison with the αL I-domain reveals two substitutions in the immediate vicinity of MIDAS, Met-140 and Leu-142 in αL for Gly-142 and Ile-144 in αD respectively. Also, M^{2+} -free MIDAS and MIDAS- M^{2+} geometries in other leukocyte αI -domains have similar structural changes (Lee et al., 1995; Qu and Leahy, 1995; Vorup-Jensen et al., 2003). Collectively, these variations in the $\beta 2$ αI -domains are plausible reasons for the difference in their ligand specificities and the hypothesized conformational dynamics.

The successful co-crystallization and structure determination of αD I-domain with other M^{2+} -ions, Cd^{2+} , Mn^{2+} , Zn^{2+} , Ni^{2+} , Co^{2+} , and Cu^{2+} , indicate the αD I-domain-MIDAS, aside from Mg^{2+} -ion can accommodate other metals. In this current study, the thermal stability of αD I-domain is greatly enhanced by increasing concentrations of Mg^{2+} , Cd^{2+} , Mn^{2+} , and Co^{2+} . On the contrary, the αD I-domain stability is drastically reduced by increasing concentration of Zn^{2+} . These findings suggest that M^{2+} -binding affect the stability of the αD I-domain and may be associated with the structural alteration of the αD I-domain after MIDAS saturation—further in solution studies like SAXS are needed to further confirm M^{2+} -effect on the αD I-domain structure. In addition, the affinity difference obtained for each metal in our ITC binding experiment confirms the suggestion

that each metal cation may perform specific and different roles in α D I-domain-ligand interaction. Furthermore, the binding of α D β 2 to fibrinogen in the presence of different metal ions suggest that M^{2+} -ions show distinct effects on the overall integrin function.

α D β 2 has been shown to bind invitro VCAM-1, ICAM-3, vitronectin, and fibrinogen (Yakubenko et al., 2006) but has never been shown to bind complement molecule iC3b. Our cell-based assays show that human α D β 2, when expressed recombinantly, binds to iC3b-opsonized erythrocytes weakly in Mg^{+2} and strongly in Mn^{+2} , similarly to CR4 but not CR3. Characterization of α D β 2 with β 2-specific functional antibodies (activation and inhibition) confirmed the α D β 2-iC3b binding. Overall, these results suggest that α D β 2 regulates its affinity to E-IgM-iC3b as similar to its CR3 and CR4, most potentially through its α D I-domain, appearing as another complement receptor.

5.2 Future prospects

We co-crystallized the α D I-domain in the presence of Mg^{2+} , Ca^{2+} , Mn^{2+} , Co^{2+} , Ni^{2+} , Zn^{2+} , and Cu^{2+} in the PEG condition (Appendix) and collected anomalous diffraction at the absorption edge of each M^{2+} -ion (where f'' is maximum). However, structure determination and refinement have not been finalized. Also, since the malic acid precipitant crystal structure showed a local structural difference in the α 1, α 6, and α 7-helices when compared to the PEG-crystals, it is necessary to repeat the co-crystallization studies with M^{2+} -ions using malic acid precipitant. This may help identify possible structural changes effected by these M^{2+} -ions. Time-resolved small angle X-ray scattering (SAXS) experiments will be conducted to visualize the steps in the dynamic conformational continuum of the α D I-domain induced by different M^{2+} -ions. Hybrid non-equilibrium MD/Monte Carlo (neMD/MC) will be used to assess the ionization states of the MIDAS-titratable residues and characterize the physical properties of the M^{2+} -MIDAS assembly.

The stabilization of α D I-domain against thermal denaturation, and effect of metal cations, will also be confirmed by differential scanning calorimetry (DSC). In addition, we will use calorimetry and quantum mechanics (QM) calculations to characterize the thermochemistry of the M^{2+} - α D I-domain assembly and stability. Finally, molecular dynamic (MD) simulations and fluorescence denaturation will be employed to probe the molecular basis of M^{2+} -dependent ionization alterations in MIDAS.

Chapter II: The integrin α X I-domain: Expression, Purification and Triple Resonance Backbone Assignment

1. INTRODUCTION

α X β 2 and α D β 2 have been shown to exhibit similar recognition specificity and also bind several proteins in the extracellular matrix, which suggests that α D I-domain might perform analogous functions to α X I-domain. Several studies have been conducted to determine the X-ray crystal structures of the isolated α X I-domain including an ectodomain structure of α X β 2 in the closed and metastable states (Sen et al., 2013; Vorup-Jensen et al., 2003). However, these crystal structures only provide the average positions and arrangement of individual atoms of this protein in either metal-ion free state or open state. Furthermore, these structures fail to report on the molecular motions of the α X I-domain in its transition between the closed and open forms. Nuclear magnetic resonance (NMR) spectroscopy is a well-known technique used for studying the structure of biological molecules in solution. Recent SAXS and DSF studies in our lab (Manandhar et al., 2021 unpublished) have shown that the MIDAS and the α I- α 7 helix of the α X I-domain adopt multiple states, residues experiencing structural motions should theoretically move into multiple electronic configurations. Thus, NMR studies of integrin α X I-domain may help understand better the structural dynamics or molecular motions of this protein in solution. In this Chapter, I performed a nuclear magnetic resonance (NMR) experiment to obtain the triple resonance NMR backbone assignment of the α X I-domain integrin as part of a collaboration on “Heterotropic roles of M^{2+} -ions in the establishment of allostery and affinity maturation of integrin α X β 2”, with one of my colleagues in our lab.

1.1 Integrin $\alpha X\beta 2$: chromosomal location and expression

The $\alpha X\beta 2$ integrin is a member of the leukocyte or $\alpha X\beta 2$ -integrin family, which consists of 150 kDa $\alpha X/CD11c$ and 95 kDa $\beta 2/CD18$ integrin subunits. The *ITGAX* gene has 31 exons separated by 30 introns that is located on chromosome 16 and encompasses nearly 28 kbp. However, the *ITGB2* gene has 16 exons separated by 15 introns that is located on chromosome 21 and encompasses about 46 kbp (Stewart et al., 1995). αX protein is dominantly expressed on monocytes and myeloid dendritic cells. Typically, αX expression is predominately on tissue macrophages, mostly on pulmonary alveolar macrophages, and dendritic cells of the splenic white pulp. It is also distributed on natural killer cells, subsets of T and B cells (Arnaout, 2016; Keizer et al., 1987b; Schittenhelm et al., 2017).

1.2 Roles/Importance and effect of $\alpha X\beta 2$ expression

Differential expression of $\alpha X\beta 2$ is implicated in various diseases including inflammation development and antimicrobial responses (Jawhara et al., 2017). The increased expression of $\alpha X\beta 2$ has been widely suggested to contribute to the onset of atherosclerosis, which is pathologically characterized by leukocyte activation, migration across inflamed endothelium, and their deposition on the arterial walls (Wu et al., 2009). Additionally, the overexpression of $\alpha X\beta 2$ on natural killer cells can cause hypocholesteremia. In contrast, reduced expression of $\alpha X\beta 2$ has been implicated in autoimmune encephalomyelitis (Hu et al., 2010). Recent studies on the role of $\alpha X\beta 2$ done in mouse model indicated that $\alpha X\beta 2$ knockout reduced recruitment of monocytes and macrophages into the peritoneum and their ability to adhere to the endothelium (Jawhara et al., 2017). Integrin $\alpha X\beta 2$ is widely employed as a marker of dendritic cells (Metlay et al., 1990). An increasing number of reports have showed that $\alpha X\beta 2$ is overexpressed in memory B cells

suggesting its role in autoimmune diseases (Vorup-Jensen and Jensen, 2018). $\alpha X\beta 2$ differentially binds the complement fragment—iC3b and therefore identified as complement receptor 4 (CR4). The CR4 modulates phagocytosis of particles opsonized with the complement product iC3b. $\alpha X\beta 2$ integrin is therefore involved in the regulation and priming of the immune system by mediating leukocyte extravasation and phagocytosis (Vorup-Jensen and Jensen, 2018; Xie et al., 2010). Lack of $\alpha X\beta 2$ in myeloid cells has been linked to the development of leukocyte adhesion deficiency (LAD) involving life-threatening and recurrent bacterial infections. It should be noted that in leukocyte adhesion deficiency I (LAD-I), the firm adhesion of leukocyte to the endothelium is defective as a result of mutations in the $\beta 2$ integrin gene (Fischer et al., 1988; Hanna and Etzioni, 2012). Integrin $\alpha X\beta 2$ has been identified as a leukocyte receptor for the opportunistic fungus *Candida albicans*. Evidence from a *Candida albicans* study demonstrated the unique role of $\alpha X\beta 2$ in the protection against fungal infections (Jawhara et al., 2012).

The differential functions of $\alpha X\beta 2$ suggest a dominant role of $\alpha X\beta 2$ over other related $\beta 2$ integrins in regulating the inflammatory function of recruited and tissue-resident macrophages (Lukácsi et al., 2020). The significant involvement of $\alpha X\beta 2$ in the immune system and related implications in multiple diseases makes this protein a good therapeutic target for autoimmune pathologies. Nuclear magnetic resonance studies of the αX I-domain will help provide a better understanding of the structural properties of this protein, including the molecular motions of in solution, and its interactions, which may be necessary for the subsequent design of agonist and antagonist compounds targeted to this receptor.

1.3 $\alpha X\beta 2$ ligands

The distinctive aspect of $\beta 2$ family of integrins is their ability to recognize and bind diverse collection of large molecules called ligands, which are either sub-endothelial matrix proteins or plasma proteins (Bilsland et al., 1994; Sadhu et al., 2007). As stated earlier, $\alpha X\beta 2$ is also known as complement receptor 4 and therefore is reported to bind the complement fragment—iC3b (Bilsland et al., 1994) and a glycosyl-phosphatidylinositol-linked receptor found on human neutrophils—Fc γ RIII-B (Galon et al., 1996). $\alpha X\beta 2$ is reported to bind to several extracellular matrix proteins such as fibrinogen (Loike et al., 1991) and type I collagen (Garnotel et al., 2000). Members of the immunoglobulin superfamily, such as intercellular adhesion molecules ICAM-1 (Blackford et al., 1996), ICAM-2 (Sadhu et al., 2007), and ICAM-4 (Ihanus et al., 2007), are among the diverse group of ligands $\alpha X\beta 2$ binds. $\alpha X\beta 2$ has also been shown to bind vascular adhesion molecule VCAM-1 (Sadhu et al., 2007). Furthermore, $\alpha X\beta 2$ interacts with a non-protein ligand (heparin) (Vorup-Jensen et al., 2007a), denatured proteins (Davis, 1992), and negatively charged amino acid residues (Vorup-Jensen et al., 2005). Basically, $\alpha X\beta 2$ is highly promiscuous receptor.

1.4 The αX I-domain

The αX subunit contains an α (inserted) I-domain, which is connected to the β -propeller domain that plays a central role in ligand binding and integrin activation. The αX I-domain adopts a similar structure to the αD I-domain; a Rossmann-type fold with a central hydrophobic six-stranded β -sheet surrounded by seven amphipathic α -helices. The αX I-domain contains a Mg^{2+} ion at the metal ion-dependent adhesion site (MIDAS) at the ligand-binding “top” face at the C terminal ends of the parallel β strands as shown in Figure 38C. Although the first crystal structure

of the α_X I-domain lacked a metal ion at the MIDAS, the crystal structure of the $\alpha_X\beta_2$ ectodomain discovered in later years had a metal ion at the MIDAS (Sen et al., 2013; Xie et al., 2010).

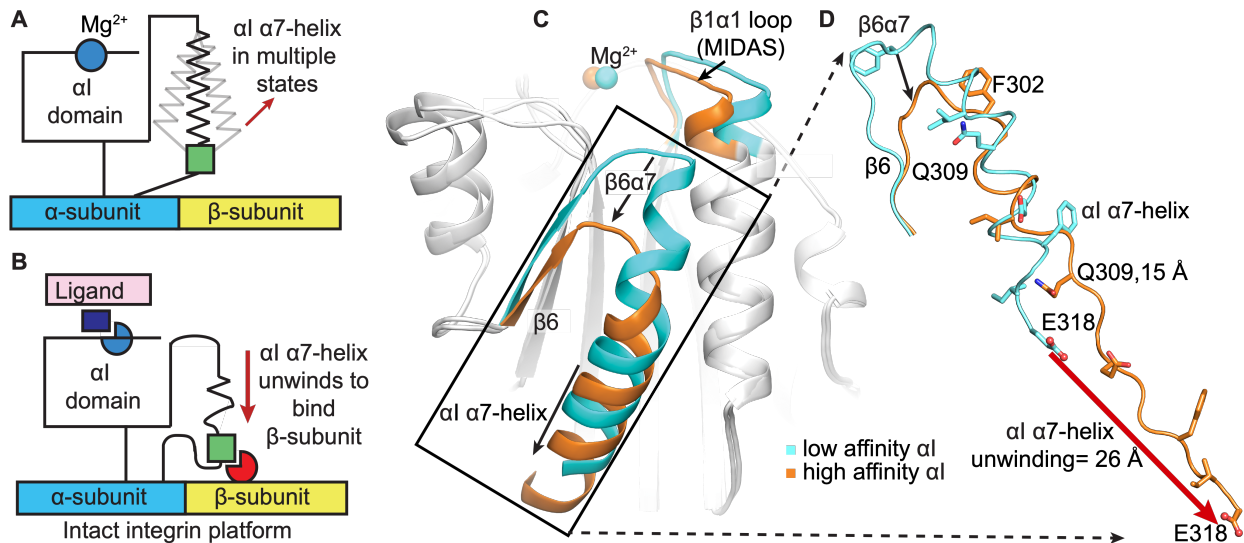


Figure 38. Structural rearrangements during integrin activation. Schematic diagrams of the α_I α_7 -helix motion during the integrin activation from (A) the closed/low-affinity states to (B) open/high-affinity states. (C) superimposition of the isolated closed (PDB# 1JLM) and open (PDB# 1IDO) α_M I-domain. (D) superimposition of the closed (PDB# 5ES4) and open (PDB# 4NEH) α_X I-domain on intact $\alpha_X\beta_2$. Adapted from (Manandhar et al., 2017)

The α_X I-domain, just like all characterized α_I -domain integrins, binds to its ligands using interactions with the coordinated Mg^{2+} ion and metal-coordinated residues in three different loops of MIDAS. The metal coordinating residues are mostly polar and negatively charged amino acids. For example, the first loop between the β_1 strand and α_1 helix contains three coordinating residues in a sequence of Asp-X-Ser-X-Ser (DXSXS) MIDAS motif, which is shown to be highly conserved among the α_I -domains. The second loop donates a threonine residue, and the third loop donates an aspartate residue. A water molecule forms a hydrogen bond with the side chains of MIDAS residues Asp-138, Thr-207, and Asp-240 as shown in Figure 39A. The ligand-binding

causes a synchronized reorganization of the loop around MIDAS and is hypothesized to induce a downward motion of the distal α X I α 7-helix through a 30 Å downward shift of the invariant Glu piston, allowing allosteric relay between the α and β subunits (Sen et al., 2013; Takagi et al., 2002; Takagi and Springer, 2002). This motion explained above results in the formation of a negative potential around the positively charged magnesium ion (Shimaoka et al., 2003b).

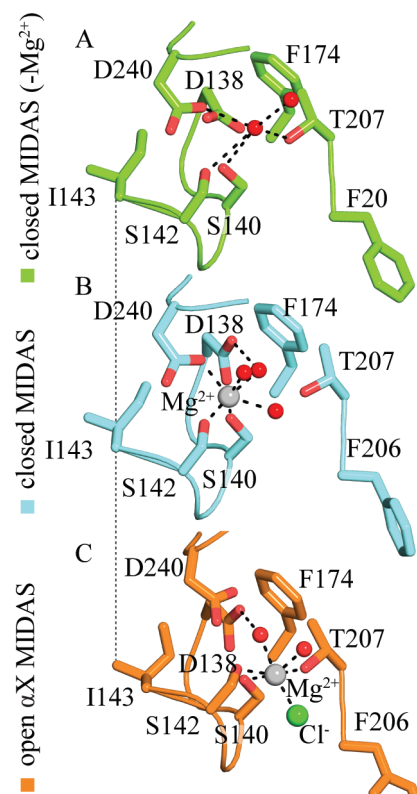


Figure 39. Difference in the magnesium coordination at MIDAS in the closed and open states of the α X I-domain. (A) Mg^{2+} -free closed/low- affinity state (B) Mg^{2+} -bound closed/low- affinity state (C) Mg^{2+} -bound open/high-affinity state.

2 MATERIALS AND EXPERIMENTAL PROCEDURES

2.1 Expression and purification of α X I-domain in minimal media

The DNA for the integrin α X I-domain was cloned into the pet28a expression vector with an N-terminal 6His affinity tag. The recombinant α X I-domain plasmid was transformed into *Escherichia coli* BL21(DE3) cells and tested for overexpression of the α X I-domain protein. Minimal media expression was tested by inoculating overnight LB grown cells in M9 salts minimal media, supplemented with 1X BME vitamins solution, 4 g/L D-glucose, CaCl₂ (0.1 mM), MgSO₄ (2 mM) and solution-Q and allowed to grow at 37 °C. It should be noted that the growth media contained 1 mM kanamycin and chloramphenicol. The cells were allowed to grow until OD_{600 nm} = ~0.7. Protein expression was induced with IPTG to a final concentration of 1 mM and then incubated overnight at 27 °C with vigorous shaking. Following overnight expression, 5 mL of cells were centrifuged at 13,000 rpm, and tested for expression by resuspending cell pellets in 120 μ L lysis buffer. After successful lysing of cells, protein expression was accessed by SDS-PAGE gel analysis. The gel was stained with Coomassie Brilliant blue G-250 and destained to observe protein expression.

2.2 Expression of double-labelled α X I-domain in minimal media

For isotopically double-labeled samples, ¹⁵NH₄Cl, (¹⁵NH₄)₂SO₄, and [¹³C₆] D-glucose (Cambridge Isotope Laboratories Inc.) were used as the sole nitrogen and carbon sources in the minimal media respectively. First, the expression construct transformed into *E. coli* BL21(DE3) cells were used to inoculate 5 mL LB for overnight growth in the presence of kanamycin and chloramphenicol at 37 °C with orbital shaking at 250 rpm. 1 mL of the overnight culture was used to inoculate 1 L of prepared ¹⁵N/¹³C-labelled minimal media and allowed to grow at 37 °C until the OD_{600 nm} = ~0.7. Components of the minimal media and their concentrations are listed in the

appendix. α X I-domain expression was induced by adding 1 mM IPTG and cells continued to grow overnight at 27 °C with vigorous shaking at 250 rpm. After overnight growth, cells were harvested by centrifugation at 4,000 rpm and stored at -80 °C for purification.

2.3 Expression of triple-labelled α X I-domain in minimal media

To produce triple-labeled ($^{13}\text{C}/^{15}\text{N}/^2\text{D}$ -labelled) α X I-domain for further NMR experimentation, the transformed BL21 Rosetta *E. coli* cells containing the α X I-domain expression construct were used to inoculate a 5 mL LB and grown overnight at 37 °C. This was used as the starting culture. Uniform labeling was achieved by growing cells in D_2O -based M9 minimal medium supplemented with $^{15}\text{NH}_4\text{Cl}$, $(^{15}\text{NH}_4)_2\text{SO}_4$, (Cambridge isotope laboratories Inc.) and C^{13} -labelled D-Glucose (Cambridge isotope laboratories Inc.) as the sole nitrogen and carbon sources, respectively. Next, prepared 1 L of D_2O -based M9 minimal medium (filter sterilized) as shown in appendix. 0.5 mL of the starting culture was used to inoculate 4.5 mL media comprising 1 mL of prepared D_2O -based M9 minimal medium and 3.5 mL LB media and allowed to grow overnight. 2.5 mL of the overnight culture was then used to inoculate 2.5 mL of D_2O -based M9 minimal medium and again allowed to grow overnight. 2 mL of the new culture was added to 5 mL of D_2O -based M9 minimal medium and allowed to grow until it reached an OD_{600} of 1.5. This culture was then centrifuged for 25 min at 4,000 rpm. The supernatant was discarded while the cell pellets were solubilized in 100 mL D_2O -based M9 minimal medium. The solubilized cells were further grown overnight at 37 °C. Finally, all the overnight culture (100 mL) was used to inoculate 1 L of D_2O -based M9 minimal medium and allowed to grow until OD_{600} reached 0.9. Expression of protein was then induced by addition of 1 mM IPTG. After overnight growth at 27 °C, cells were harvested by centrifugation at 4,000 rpm. The supernatant was placed in the orbital

shaker for 48 h to allow regrowth of any unpelleted cells. This was then recentrifuged and cells were harvested and stored at $-80\text{ }^{\circ}\text{C}$.

2.4 Purification of NMR samples

Purification of double-labelled and triple-labelled samples was carried out separately but followed the same protocol. Cell pellets harvested by centrifugation were resuspended in lysis buffer (20 mM Tris-HCl, pH 8.0, 200 mM NaCl and 10% glycerol) and lysed by passing the cell suspension through a homogenizer (3-5 times). The homogenate was left to shake at $4\text{ }^{\circ}\text{C}$ for 30 min after adding 1X PMSF and 1 mM DNase. Cell lysates were then centrifuged at 10,000 rpm at $4\text{ }^{\circ}\text{C}$ for 45 min and the insoluble pellet was discarded. The resulting supernatant was filtered and loaded onto a Ni-Sepharose HisTrap HP column (GE-Healthcare) for purification by affinity chromatography. After washing the column with the binding buffer (20 mM Tris, pH 8.0, 40 mM imidazole, 300 mM NaCl, 10% glycerol), bound protein was eluted with a linear gradient of 0-500 mM imidazole. Fractions were assessed by SDS-PAGE to check which fractions contained the αX I-domain protein. Fractions containing the αX I-domain were pooled and concentrated to a final volume of 4.0 mL. The superdex 75 size exclusion column (Pharmacia) was equilibrated with a running buffer containing 50 mM MES, pH 6.0, 5 mM MgCl_2 , 10 mM glutamate. Finally, the protein was loaded onto the superdex-75 gel filtration column eluted with the same buffer. The purified protein was then concentrated using an amicon ultra centrifugal filter unit with a 10 K molecular mass cutoff (Amicon^R). A Coomassie blue stained SDS-PAGE was used to evaluate the purity of the αX I-domain protein with a total yield of 10 mg/mL.

2.5 NMR sample conditions and acquisition

The buffer in which the α X I-domain protein remained was exchanged to an NMR buffer (50 mM MES, pH 6.0, 10 mM MgCl₂, 20% D₂O, .04% NaN₃, 2X PMSF). This NMR buffer was carefully selected after thermal screen experiment for buffer components that can stabilize α X I-domain domain samples for structural studies using differential scanning fluorimetry (DSF).

The final volume of the NMR sample was 450 mL. NMR experiments were conducted on a Bruker 800 MHz equipped with a triple resonance ¹H/¹³C/¹⁵N optimized for proton detection at 293K. Data was processed and analyzed using SPARKY software version 3.115 (Johnson, 2004; Lee et al., 2015). All experiments were conducted at the KECK Institute for molecular design facility at the University of Houston.

2.6 Triple resonance experiments and backbone specific NMR assignment

Sequential backbone resonance assignments were carried out using ¹³C/¹⁵N and 2D/¹³C/¹⁵N labeled samples of the α x I-domain. Ninety percent of assignments were obtained by through-bond triple resonance experiments including HNCACB, CBCA(CO)NH, HNCOC, HNCACO, NHCA, and HNCOCA conducted on a Bruker 800 MHz spectrometer.

Table 10. NMR acquisition parameters

	Parameter	Value	Parameter	Value
HNCACB/CBCA(CO)NH	time domain (t1)	50	time domain (t1)	120
	time domain (t2)	64	time domain (t2)	64
	time domain (t3)	2,048	time domain (t3)	4,096
	Spectral width (t1) Hz	11,682	Spectral width (t1) Hz	5,232
	Spectral width (t2) Hz	2,343	Spectral width (t2) Hz	2,594
	Spectral width (t3) Hz	9,615	Spectral width (t3) Hz	10,416
	Number of scans	32	Number of scans	32
	sample	$^2\text{H} / ^{13}\text{C} / ^{15}\text{N}$ labeled	sample	$^{13}\text{C} / ^{15}\text{N}$ labeled
	field strength	800 MHz cryogenic TCI probe	field strength	800 MHz cryogenic TCI probe
HN(CA)CO	time domain (t1)	90	time domain (t1)	128
	time domain (t2)	64	time domain (t2)	60
	time domain (t3)	2,048	time domain (t3)	2,048
	Spectral width (t1) Hz	2,817	Spectral width (t1) Hz	2,414
	Spectral width (t2) Hz	2,432	Spectral width (t2) Hz	2,594
	Spectral width (t3) Hz	10,000	Spectral width (t3) Hz	11,160
	Number of scans	48	Number of scans	40
	sample	$^2\text{H} / ^{13}\text{C} / ^{15}\text{N}$ labeled	sample	$^2\text{H} / ^{13}\text{C} / ^{15}\text{N}$ labeled
	field strength	800 MHz cryogenic TCI probe	field strength	800 MHz cryogenic TCI probe
HNCO	time domain (t1)	90		
	time domain (t2)	64		
	time domain (t3)	1,048		
	Spectral width (t1) Hz	2,817		
	Spectral width (t2) Hz	2,432		
	Spectral width (t3) Hz	9,615		
	Number of scans	16		
	sample	$^2\text{H} / ^{13}\text{C} / ^{15}\text{N}$ labeled		
	field strength	800 MHz cryogenic TCI probe		

3. RESULTS

NMR spectroscopy is a very useful technique for the study of three-dimensional molecular structures of proteins including the study of kinetic reactions and dynamic properties of proteins at the atomic level (Poulsen, 2002). The isotopically labeled protein in solution is exposed to a strong static magnetic field perturbed by a weak oscillating magnetic field allowing for the determination of the chemical shifts of atoms in the sample. In protein NMR spectroscopy, one common experiment which measures the chemical shift of the amide nitrogen and amide hydrogen is the ^{15}N heteronuclear single quantum coherence (HSQC). Each amino acid in a protein has distinct chemical shift values and hence corresponds to unique peak in the HSQC (Cavanagh et al., 2007; Cavanagh et al., 1995; Poulsen, 2002). The process of identifying or assigning these unique peaks in the HSQC spectra is known as NMR backbone assignment. This process relies on the use of triple-resonance experiments such as HNCA and HNCACB to correlate HSQC peaks to amino acids in a protein.

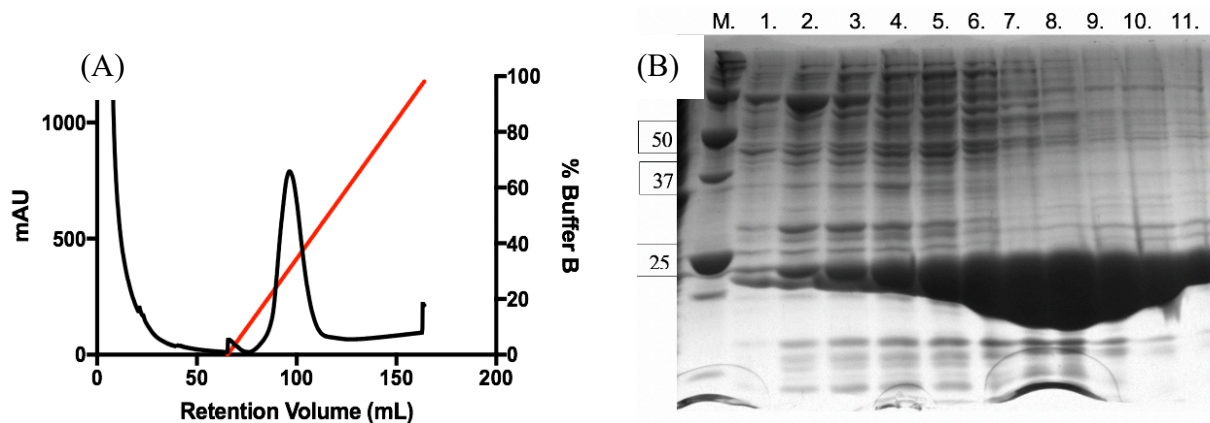


Figure 40: Affinity chromatography purification of the α X I-domain protein and SDS-PAGE analysis.

(A) Affinity chromatography purification of double labeled α X I-domain using a 5 mL HisTrap column. Protein was eluted by increasing the concentration of buffer B relative to buffer A by a linear gradient. Buffer A is 20 mM Tris, pH 8.0, 300 mM NaCl, 10% glycerol, and 40 mM imidazole. Buffer B is 20 mM Tris, pH 8.0, 300 mM NaCl, 10% glycerol, and 500 mM imidazole.

(B) SDS-PAGE of protein molecular marker (lane M) and fractions from HisTag/affinity chromatography (lane 1-11).

3.1 Expression and purification of isotopically labeled α X I-domain

To determine the backbone assignment of integrin α X I-domain, the α X I-domain cloned into a pet28a expression vector was successfully expressed in double and triple-labeled minimum media. Affinity chromatography using a Ni NTA agarose column was initially used to separate the α X I-domain protein from the cell lysates (Figure 40A and Figure 42A). The protein fractions from the affinity column were analyzed by SDS-PAGE, which confirmed the isolated His tag α X I-domain protein at around 25 kDa (Figure 40B and Figure 42B). Fractions which gave clear intense bands at 25 kDa on the SDS-Gel were pooled, concentrated, and further purified on a HiLoad superdex 75 gel filtration column (Figure 41A and 43A). Finally, about 98% pure α X I-domain protein was confirmed by SDS PAGE (Figure 41B and 43B).

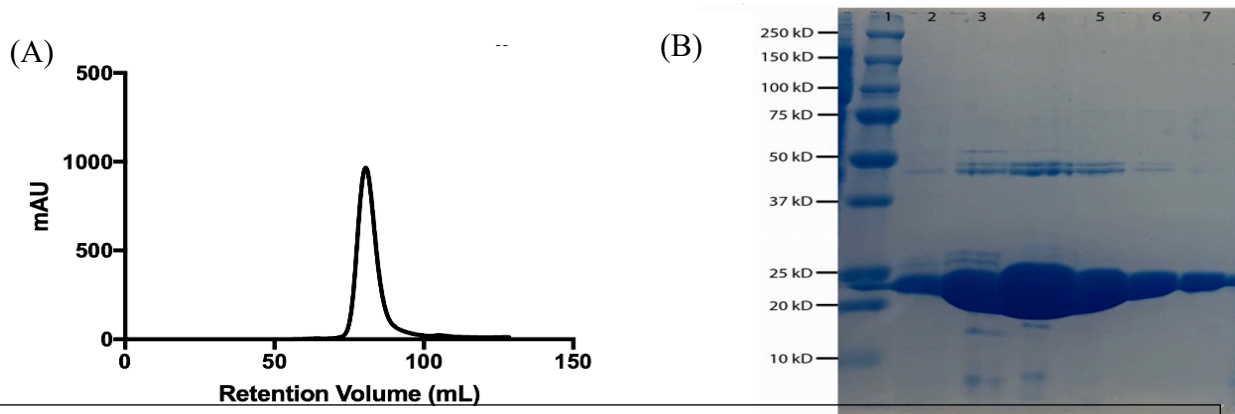


Figure 41: FPLC purification of α X I-domain protein by gel filtration chromatography and the SDS-PAGE analysis. (A) Size exclusion chromatography of double-labeled α X I-domain using Superdex 75 Hiload 16/60 column at 4 °C and a flow rate of 1 ml/min. The protein was eluted at elution volume of 80 ml using 50 mM MES, pH 6.0, 5 mM $MgCl_2$ buffer.

(B) SDS-PAGE gel of purified $^{13}C/^{15}N$ labelled α X I-domain in 12% polyacrylamide. Size exclusion chromatography fraction numbers listed at the top of the gel. Molecular weight standards are labelled at the side of the gel. The bands between 20 kD and 25 kD correspond to the α X I-domain

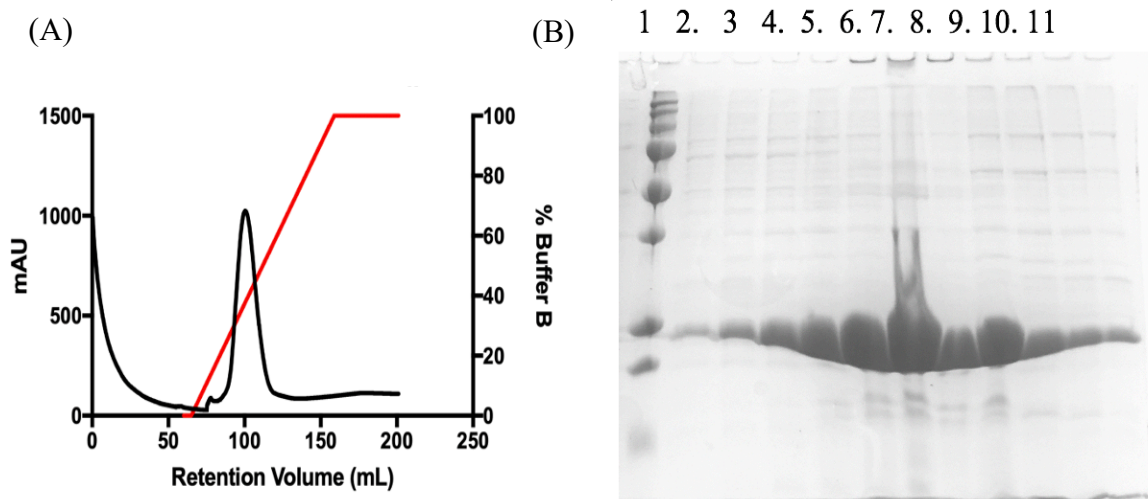


Figure 42: Affinity chromatography purification of triple-labeled α X I-domain protein and SDS-PAGE analysis. (A) Affinity chromatography purification of triple-labeled α X I-domain using a 5 mL HisTrap column. Protein was eluted by increasing the concentration of Buffer B relative to Buffer A by a linear gradient. Buffer A is 20 mM Tris, pH 8.0, 300 mM NaCl, 10% glycerol, and 40 mM imidazole. Buffer B is 20 mM Tris, pH 8.0, 300 mM NaCl, 10% glycerol, and 500 mM imidazole.

(B) SDS-PAGE of purified triple-labeled α X I-domain in 12% polyacrylamide. Protein molecular marker (lane 1) and fractions from HisTag/affinity chromatography (lane 2-11).

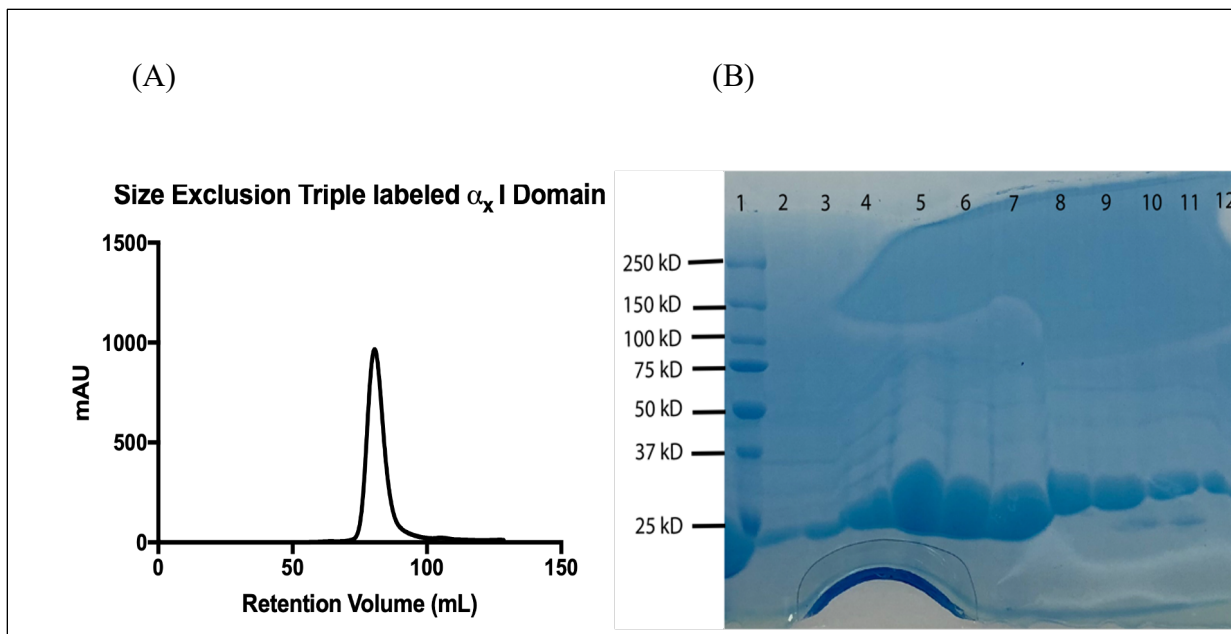


Figure 43: FPLC Purification of the α_X I-domain by size exclusion chromatography and the SDS-PAGE analysis. (A) Size exclusion chromatography of triple-labeled α_X I-domain using HiLoad 16/60 S75 column at 4 °C and a flow rate of 1 ml/min. The protein was eluted at elution volume of 80 ml using 50 mM MES, pH 6.0, 5 mM $MgCl_2$ buffer. (B) SDS-PAGE gel of purified triple-labelled α_X I-domain in 12% polyacrylamide. Size exclusion chromatography fraction numbers listed at the top of the gel. Molecular weight standards are labelled at the side of the gel. The bands between around 25 kD correspond to the α_X I-domain

3.2 ^{15}N heteronuclear single quantum coherence (HSQC) experiment

Triple resonance NMR backbone assignment is the preliminary experiment for structural studies of the α_X I-domain integrin protein. Initially, HSQC spectra was acquired for both triple-labeled ($^2D/^{13}C/^{15}N$) and double-labeled ($^{13}C/^{15}N$) α_X I-domain samples. As shown in figures 44 and 45, the HSQC spectra obtained for the triple-labeled sample has sharper and excellent dispersion of peaks relative to the HSQC of the double-labeled sample. This can be due to the slower tumbling caused by larger protein mass in the triple-labeled protein sample because most of the 1H were replaced by 2H . The HSQC spectra of the triple-labeled sample (Fig. 45) was therefore used as the template for most of the backbone assignments. For a few of the backbone

assignment, the double-labeled HSQC spectra provided resonances for residues that were not observable in the HSQC of the triple-labelled sample, such as I263.

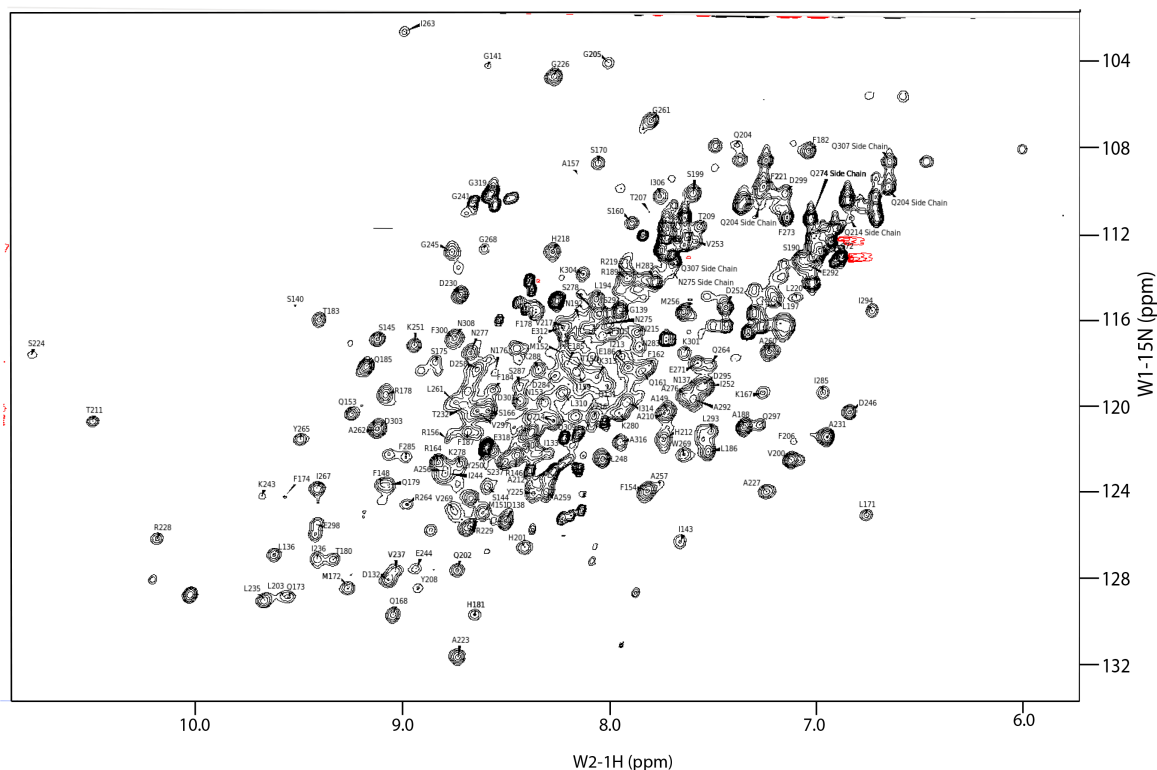


Figure 44: HSQC of double-labeled α X I-Domain. $^1\text{H}/^{15}\text{N}$ HSQC spectra of 10 mg/mL $^{13}\text{C}/^{15}\text{N}$ -labeled α X I-domain with an N-terminal hexameric histidine tag in 25 mM MES (pH 7.0) with 128 scans acquired on 800 MHz Bruker spectrometer.

Notably, in both the $^{13}\text{C}/^{15}\text{N}$ -labeled (double-labeled) and $^2\text{H}/^{13}\text{C}/^{15}\text{N}$ -labeled (triple-labeled) HSQC, there are several sets of “leak out” peaks neighboring principal peaks, which show identical resonances in triple-resonance experiments. In both HSQC spectra, 15 residues leak out peaks were observed. These residues were 149-152 as well as residues 296-306. These leak out peaks could point to ensembles of alternate conformations the protein occupies in solution. In each

alternate conformation, the local environment of an amino acid differs thus resulting in changes to chemical shift values.

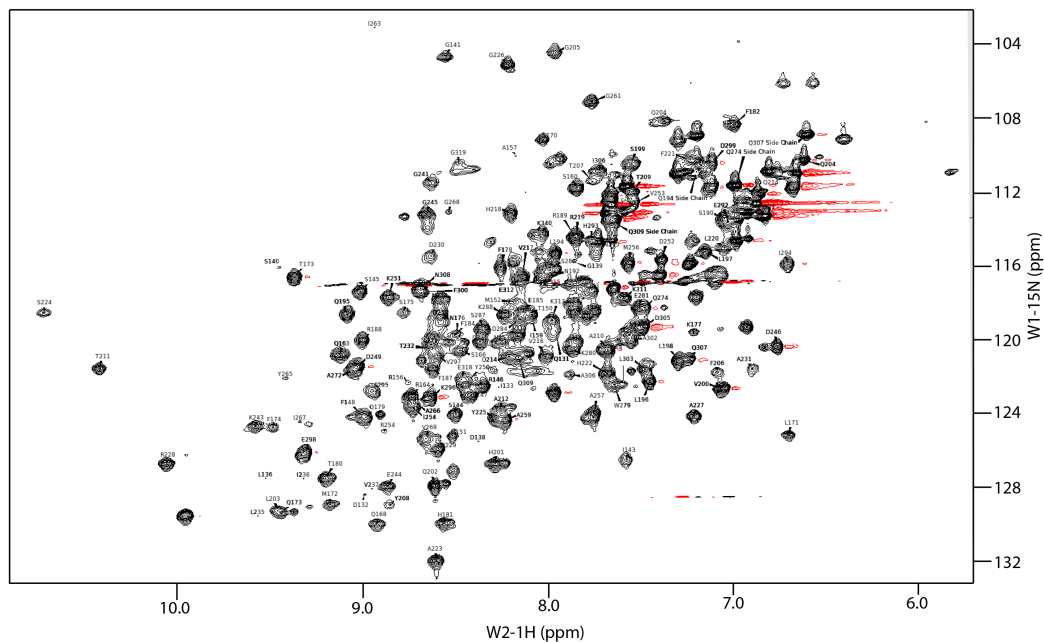


Figure 45: HSQC of triple-labeled αX I-domain. $^1\text{H}/^{15}\text{N}$ HSQC of 10 mg/mL triple-labeled αX I-domain with an N-terminal hexameric histidine tag in 25 mM MES (pH 7.0) with 128 scans acquired on 800 MHz Bruker spectrometer.

3.3 NMR backbone assignment

This backbone assignment was conducted by an undergraduate student in our laboratory, Omar Abousaway. Analysis of HNCACB and CBCA(CO)NH experiments provided the most direct way of obtaining a sequence specific backbone assignment. Strip plots showing HNCACB and CBCA(CO)NH spectra for residues K280- D284 are shown in Figure 46A.

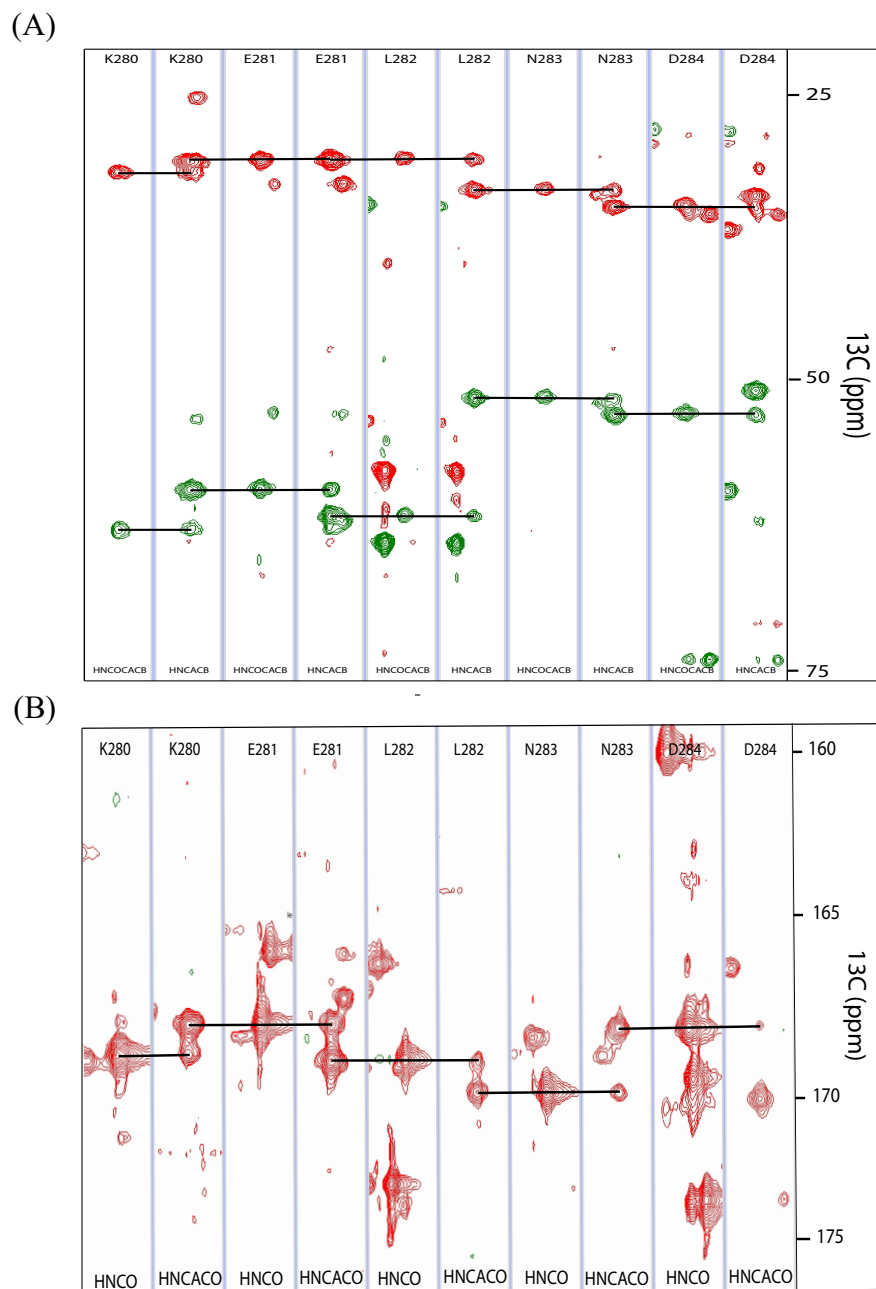


Figure 46. (A) $^2\text{D}/^{13}\text{C}/^{15}\text{N}$ -labeled triple resonance HN(CO)CACB and HNCACB spectra for residues K280-D284 of the αX I-domain showing the split resonances for $\text{C}\alpha$ and $\text{C}\beta$.

(B) HNCO and HNCACO plots for residues K280-D284 and showing the sequential through bond connectivities of ^{13}C O. The HNCO spectra at the left correlates the amide ^1H and ^{15}N resonance of the i th residue to the carbonyl ^{13}C O of the $i-1$ residue. The HNCACO spectra at the right correlates the ^1H and ^{15}N resonance of the i th residue to the carbonyl ^{13}C O of the i th and $i-1$ residue. Each spectrum was acquired at 298 K using 10 mg/mL of purified triple labeled αX I-domain.

Carbonyl carbon chemical shift assignments were made using HNCOCACB and HNCACB experiments. These experiments also served to corroborate and build on assignments made using the HNCACB and CBCA(CO)NH spectra. Shown in Figure 46B are strip plots of HNCOCACB and HNCACB spectra for residues K280-D284. Identification of Asn and Gln side chain amides is useful for assigning C β and C α chemical resonances by an analogous manner. In the HNCACB experiment, magnetization transfer of Asn amide side chain protons to the neighboring carbons will provide the chemical shifts of the C α and C β . In the same manner, magnetic transfer of the Gln amide side chain proton provides the chemical shifts of C γ and C β . Analysis of these peaks provides a convenient method to confirm the C α and C β assignments using the HNCACB and HNCOCACB spectra.

Overall, 88.7% of peaks were assigned in the HSQC. Assigned amino acids are presented in Figure 47. Missing peaks included: M129, E130, V134, F135, I137, S142, V155, V159, T167, F169, S191, K233, I234, I238, T239, D240, K242, R276, S290, and I317. List of chemical shifts for assigned residues in appendix.

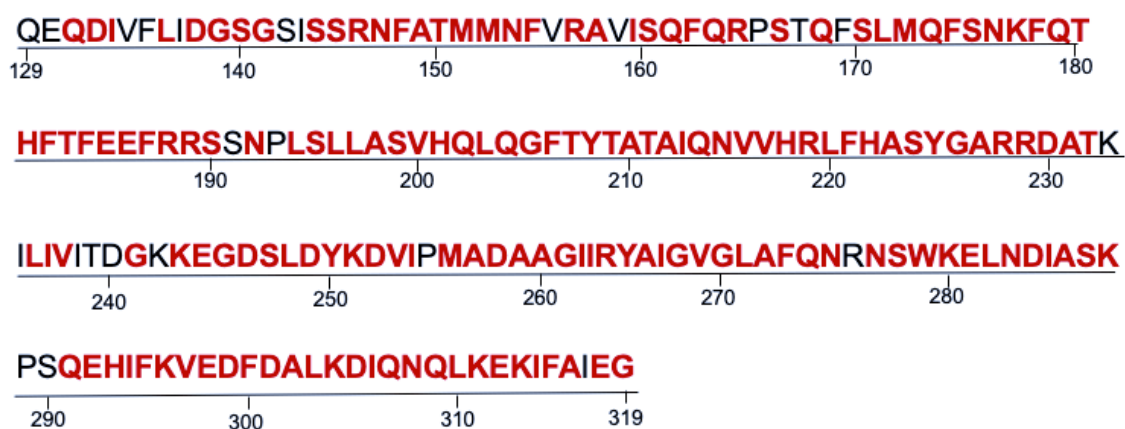


Figure 47: α X I-domain residues assigned in HSQC. Residues of α X I-domain assigned in HSQC spectra. Assigned residues colored in red. Residues not assigned in black.

4. DISCUSSION

This study reported the preliminary biophysical approach to discern and quantify α X I-domain conformational dynamics through 3D ^1H NMR. The reported assignments comprise 88.7% of all backbone ^1H , ^{15}N , $^{13}\text{C}\alpha$, and $^{13}\text{C}\beta$, and ^{13}CO resonances of the α X I-domain, covering 165 of the 186 non-proline residues. The assigned (red) and unassigned (black) amino acid residues are presented in Figure 10. The missing assignments can be attributed to the absence of corresponding backbone amide resonances in the 2D/3D spectra, likely due to severe chemical exchange line broadening—also prolines don't have amide signal and we have four number of prolines in the α X I-domain. The backbone assignment independently confirmed a SAXS and DSF data obtained from previous experiments with the α X I-domain conducted in our laboratory, which showed that the MIDAS and the $\alpha\text{I}-\alpha 7$ helix adopt multiple states, residues experiencing structural motions should theoretically move into multiple electronic configurations. The results from this study also confirms the hypothesis that split resonances in the ^1H -axis of 3D HNCACB ($^1\text{H} \rightarrow ^{15}\text{N} \rightarrow ^{13}\text{C}\alpha$ and $^{13}\text{C}\beta$) NMR spectra (Figure 48A), exclusively for the MIDAS and $\alpha\text{I}-\alpha 7$ helix as well as the $\beta 6$ -strand and $\beta 6-\alpha 7$ loop, indicate at least two unique conformations exist (Figure 48A). The identified secondary structure elements from the analysis of the assigned chemical shifts are in good agreement with the crystal structures of α X I-domain. Also, we noted similar dynamism in the α D I-domain structures determined. As shown in Figure 48B, all the residues having split peaks in the NMR (in red) were mapped to the superimposed closed and open structures together with conformationally moving $\text{C}\alpha$ -atoms indicated by black lines. Residues that did or did not show peak-splitting had a root-mean-square deviation (RMSD) of 9 Å and 0.8 Å, respectively. Furthermore, the presence of the leak out peaks suggests that the protein exists in more than one

ensemble conformations in solution. It should be noted that this is the first extensive NMR assignment obtained for the integrin α_X I-domain protein and thus the first report of this finding.

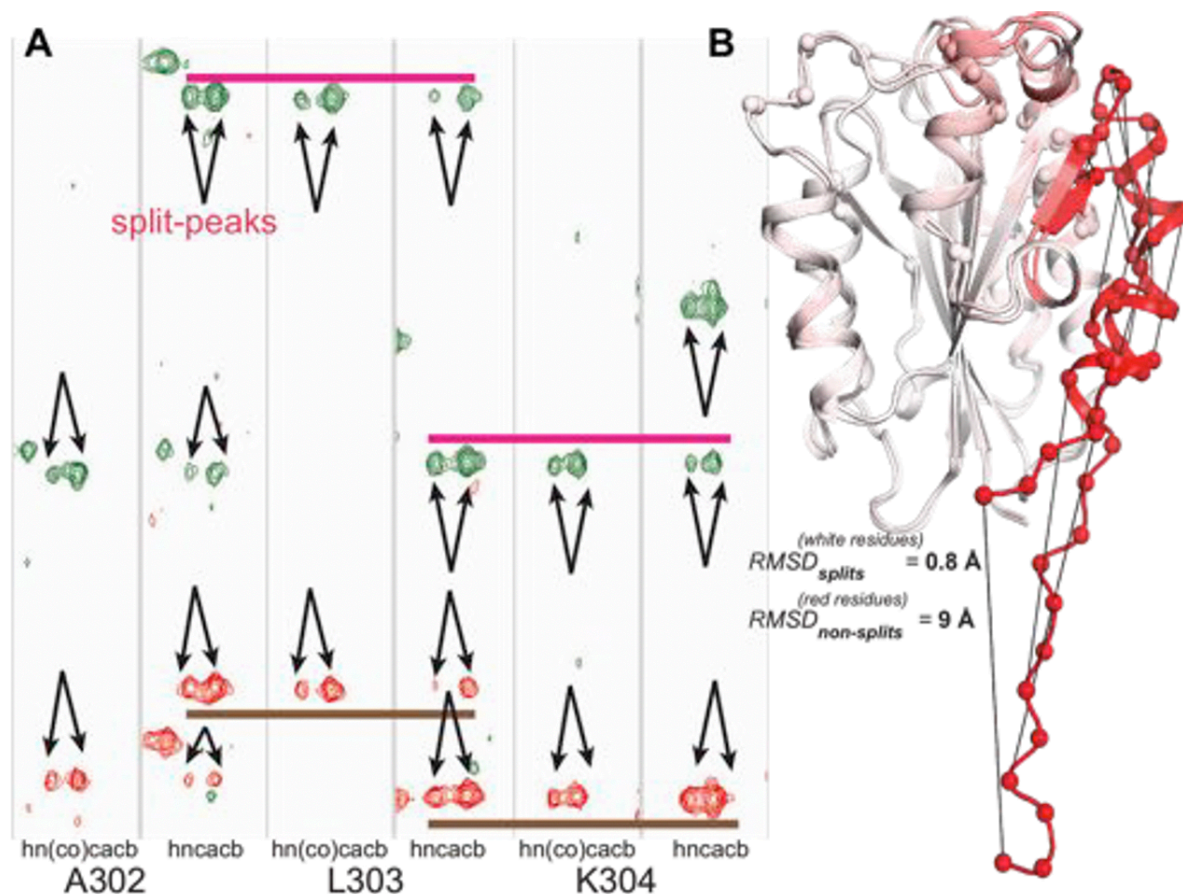


Figure 48. (A) $^1\text{H}/^{13}\text{C}/^{15}\text{N}$ triple resonance HNCACB and HN(CO)CACB plots for the residues (A302, L303, and K304) located the allosteric $\alpha\text{I}-\alpha 7$ helix and showed split resonances for $\text{C}\alpha$ and $\text{C}\beta$, directly showing two unique states. (B) All of the residues having split peaks in our NMR study are mapped to two structural states (closed and open). Residues moving more than 1 Å are shown with $\text{C}\alpha-\text{C}\alpha$ line.

The residues A149-M152 are found in the $\alpha 1$ helix, and residues 296-306 compose the $\beta 6-\alpha 7$ loop. These are the residues that are most affected by the suggested transition between alternate conformational states. NMR resonance splitting was extensively observed in the C-terminal residues encompassing the $\beta 6\alpha 7$ -loop and the $\alpha 7$ -helix as well. Given that the $\beta 6-\alpha 7$ loop has been

found to move in the transition between the open and closed conformational states, this data might suggest that the αX I-domain of the integrin $\alpha X\beta 2$ exists in both the open and closed conformations in solution. This could be significantly biologically relevant because it suggests that the αX I-domain can exist in the ligand binding-competent state without need of an intracellular signal.

5 CONCLUSION AND FUTURE DIRECTIONS

Protein NMR studies are often hindered by a number of problems including aggregation at high protein concentration and internal dynamics (Piserchio et al., 2012). Since the NMR technique requires stable, highly purified, and concentrated sample at temperatures over 20 °C, we employed the ThermoFluor screen platform via differential scanning fluorimetry (DSF) (Boivin et al., 2013) to obtain optimal conditions that helped stabilize α X I-domain samples at high concentration and ambient temperature. In general, our NMR backbone assignment suggests at least two unique conformations exist in the α X I-domain. Although the process of backbone resonance assignments is time and resource consuming, obtaining these assignments is clearly worthwhile due to their usefulness in investigating protein-protein or protein-ligand interactions as well as determining the overall molecular structure of this protein. In the near future, we plan to characterize the spatial and kinetic features of the α X I-domain shape-shifting using ^{19}F NMR, which provides a relatively nonperturbing probe without background in protein dynamics studies (Danielson and Falke, 1996). Several statin drugs, which are typically used to inhibit the production of cholesterol, have been reported to selectively bind and inhibit integrin proteins (Jensen et al., 2016; Weitz-Schmidt et al., 2001). For instance, the highly anti-inflammatory simvastatin, which is used clinically to reduce cholesterol levels by inhibiting HMG-CoA reductase has been reported to bind and competitively inhibit integrin interaction with extracellular ligands (Arora et al., 2006; Jensen et al., 2016; Rosenson et al., 1999). This means analogs of statin drugs optimized that selectively bind to leukocyte integrin could be promising anti-inflammatory drugs for a specific pathology. Future experiments could involve probing simvastatin- α X β 2 interaction via NMR spectroscopy.

APPENDIX I: Media, gels and buffers for α D I-domain sample preparation

To prepare 1 L Terrific Broth (TB) media

Reagent.	Quantity
Yeast Extract:	24 g
Tryptone:	12 g
Glycerol:	4 mL
0.17 M KH_2PO_4	
0.72 M K_2HPO_4 .	100 mL

Add 900 mL of deionized water to 24 g of yeast extract, 20 g of tryptone, and 4 mL of glycerol. Shake or stir until the solutes have dissolved and sterilize by autoclaving for 30 min at 15 psi (1.05 kg/cm²). Allow the solution to cool to ~25 °C and add 100 mL of sterilized phosphate buffer (0.17 M KH_2PO_4 + 0.72 M K_2HPO_4). Store TB at room temperature.

12% SDS PAGE gel recipe

Reagents	12% Running gel (V=10m)	4% Stacking gel (V=10m)
40% Acrylamide	3.12 mL	0.625 mL
1.5 M Tris-HCl (pH 8.8)	2.5 mL	
0.5 M Tris-HCl (pH 6.8)		1.5 mL
100% SDS	100 μL	100 μL
10% APS	100 μL	100 μL
TEMED	10 μL	10 μL
H ₂ O	4.38 mL	7.8 mL

Protein purification buffers (α D I-domain)

Lysis buffer: 20 mM Tris pH 8.0, 200 mM NaCl

Affinity chromatography (5 ml HisTrap column):

Running buffer: 20 mM Tris pH 8.0, 40 mM imidazole, 300 mM NaCl, 10% glycerol at 4°C

Elution buffer: 20 mM Tris pH 8.0, 500 mM imidazole, 300 mM NaCl, 10% glycerol at 4°C

Gel filtration chromatography (HiLoad Superdex75 16/60):

Running buffer 1: 20 mM HEPES pH 7.4, 150 mM NaCl, at 4 °C

Running buffer 2: 20 mM Tris pH 7.4, 150 mM NaCl, at 4 °C

APPENDIX II: Hampton Research crystal screen conditions

Table A1: Hampton Research crystal screen HR2-130 reagent formulation

#	Reagent	Formulation
1.(A1)		0.02 M calcium chloride dihydrate, 0.1 M sodium acetate trihydrate pH 4.6, 30% v/v (+/-)-2-methyl-2,4-pentanediol
2.(A2)		0.4 M potassium sodium tartrate tetrahydrate
3.(A3)		0.4 M ammonium phosphate monobasic
4. (A4)		0.1 M TRIS hydrochloride pH 8.5, 2.0 M ammonium sulfate
5. (A5)		0.2 M sodium citrate tribasic dihydrate, 0.1 M HEPES sodium pH 7.5, 30% v/v (+/-)-2-methyl-2,4-pentanediol
6. (A6)		0.2 M magnesium chloride hexahydrate, 0.1 M TRIS hydrochloride pH 8.5, 30% w/v polyethylene glycol 4,000
7. (A7)		0.1 M sodium cacodylate trihydrate pH 6.5, 1.4 M sodium acetate trihydrate
8. (A8)		0.2 M sodium citrate tribasic dihydrate, 0.1 M sodium cacodylate trihydrate pH 6.5, 30% v/v 2-propanol
9. (A9)		0.2 M ammonium acetate, 0.1 M sodium citrate tribasic dihydrate pH 5.6, 30% w/v polyethylene glycol 4,000
10. (A10)		0.2 M ammonium acetate, 0.1 M sodium acetate trihydrate pH 4.6, 30% w/v polyethylene glycol 4,000
11. (A11)		0.1 M sodium citrate tribasic dihydrate pH 5.6, 1.0 M ammonium phosphate monobasic
12. (A12)		0.2 M magnesium chloride hexahydrate, 0.1 M HEPES sodium pH 7.5, 30% v/v 2-propanol
13. (B1)		0.2 M sodium citrate tribasic dihydrate, 0.1 M TRIS hydrochloride pH 8.5, 30% v/v polyethylene glycol 400
14. (B2)		0.2 M calcium chloride dihydrate, 0.1 M HEPES sodium pH 7.5, 28% v/v polyethylene glycol 400
15. (B3)		0.2 M ammonium sulfate, 0.1 M sodium cacodylate trihydrate pH 6.5, 30% w/v polyethylene glycol 8,000
16. (B4)		0.1 M HEPES sodium pH 7.5, 1.5 M Lithium sulfate monohydrate
17. (B5)		0.2 M lithium sulfate monohydrate, 0.1 M TRIS hydrochloride pH 8.5, 30% w/v polyethylene glycol 4,000
18. (B6)		0.2 M magnesium acetate tetrahydrate, 0.1 M sodium cacodylate trihydrate pH 6.5, 20% w/v polyethylene glycol 8,000
19. (B7)		0.2 M ammonium acetate, 0.1 M TRIS hydrochloride pH 8.5, 30% v/v 2-propanol
20. (B8)		0.2 M ammonium sulfate, 0.1 M sodium acetate trihydrate pH 4.6, 25% w/v polyethylene glycol 4,000
21. (B9)		0.2 M magnesium acetate tetrahydrate, 0.1 M sodium cacodylate trihydrate pH 6.5, 30% v/v (+/-)-2-methyl-2,4-pentanediol
22. (B10)		0.2 M sodium acetate trihydrate, 0.1 M TRIS hydrochloride pH 8.5, 30% w/v polyethylene glycol 4,000
23. (B11)		0.2 M Magnesium chloride hexahydrate, 0.1 M HEPES sodium pH 7.5, 30% v/v Polyethylene glycol 400
24. (B12)		0.2 M calcium chloride dihydrate, 0.1 M sodium acetate trihydrate pH 4.6, 20% v/v 2-propanol
25. (C1)		0.1 M imidazole pH 6.5, 1.0 M sodium acetate trihydrate
26. (C2)		0.2M ammonium acetate, 0.1 M sodium citrate tribasic dihydrate pH 5.6, 30% v/v (+/-)-2-methyl-2,4-pentanediol
27. (C3)		0.2 M sodium citrate tribasic dihydrate, 0.1 M HEPES sodium pH 7.5, 20% v/v 2-propanol
28. (C4)		0.2 M sodium acetate trihydrate, 0.1 M sodium cacodylate trihydrate pH 6.5, 30% w/v polyethylene glycol 8,000
29. (C5)		0.1 M HEPES sodium pH 7.5, 0.8 M potassium sodium tartrate tetrahydrate
30. (C6)		0.2 M ammonium sulfate, 30% w/v polyethylene glycol 8,000
31. (C7)		0.2 M ammonium sulfate, 30% w/v polyethylene glycol 4,000
32. (C8)		2.0 M ammonium sulfate
33. (C9)		4.0 M sodium formate
34. (C10)		0.1 M sodium acetate trihydrate pH 4.6, 2.0 M sodium formate
35. (C11)		0.1 M HEPES sodium pH 7.5, 0.8 M sodium phosphate monobasic monohydrate, 0.8 M potassium phosphate monobasic
36. (C12)		0.1 M TRIS hydrochloride pH 8.5, 8% w/v polyethylene glycol 8,000
37. (D1)		0.1 M sodium acetate trihydrate pH 4.6, 8% w/v polyethylene glycol 4,000
38. (D2)		0.1 M HEPES sodium pH 7.5, 1.4 M sodium citrate tribasic dihydrate
39. (D3)		0.1 M HEPES sodium pH 7.5, 2% v/v polyethylene glycol 400, 2.0 M ammonium sulfate
40. (D4)		0.1 M sodium citrate tribasic dihydrate pH 5.6, 20% v/v 2-propanol, 20% w/v polyethylene glycol 4,000
41. (D5)		0.1 M HEPES sodium pH 7.5, 10% v/v 2-propanol, 20% w/v polyethylene glycol 4,000

Table A1 continued.

42. (D6)	0.05 M potassium phosphate monobasic, 20% w/v polyethylene glycol 8,000
43. (D7)	30% w/v polyethylene glycol 1,500
44. (D8)	0.2 M magnesium formate dihydrate
45. (D9)	0.2M zinc acetate dihydrate, 0.1 M sodium cacodylate trihydrate pH 6.5, 18% w/v polyethylene glycol 8,000
46. (D10)	0.2M calcium acetate hydrate, 0.1M sodium cacodylate trihydrate pH 6.5, 18% w/v polyethylene glycol 8,000
47. (D11)	0.1 M sodium acetate trihydrate pH 4.6, 2.0 M ammonium sulfate
48. (D12)	0.1 M TRIS hydrochloride pH 8.5, 2.0 M ammonium phosphate monobasic
49. (E1)	2.0 M sodium chloride, 10% w/v polyethylene glycol 6,000
50. (E2)	0.5 M sodium chloride, 0.01 magnesium chloride hexahydrate, 0.01 M hexadecyltrimethylammonium bromide
51. (E3)	25% v/v ethylene glycol
52. (E4)	35% v/v 1,4-Dioxane
53. (E5)	2.0 M ammonium sulfate, 5% v/v 2-propanol
54. (E6)	1.0 M imidazole pH 7.0
55. (E7)	10% w/v polyethylene glycol 1,000, 10% w/v polyethylene glycol 8,000
56. (E8)	1.5 M sodium chloride, 10% v/v ethanol
57. (E9)	0.1 M sodium acetate trihydrate pH 4.6, 2.0 M sodium chloride
58. (E10)	0.2 M sodium chloride, 0.1 M Sodium acetate trihydrate pH 4.6, 30% v/v (+/-)-2-methyl-2,4-pentanediol
59. (E11)	0.01 M cobalt (II) chloride hexahydrate, 0.1 M sodium acetate trihydrate pH 4.6, 1.0 M 1,6-hexanediol
60. (E12)	0.1 M cadmium chloride hydrate, 0.1 M Sodium acetate trihydrate pH 4.6, 30% v/v polyethylene glycol 400
61. (F1)	0.2M ammonium sulfate, 0.1 M sodium acetate trihydrate pH 4.6, 30% w/v PEG monomethyl ether 2,000
62. (F2)	0.2M potassium sodium tartrate tetrahydrate, 0.1M sodium citrate tribasic dihydrate pH 5.6, 2.0 M ammonium sulfate
63. (F3)	0.5M ammonium sulfate, 0.1 M sodium citrate tribasic dihydrate pH 5.6, 1.0 M lithium sulfate monohydrate
64. (F4)	0.5 M sodium chloride, 0.1 M sodium citrate tribasic dihydrate pH 5.6, 2% v/v ethylene imine polymer
65. (F5)	0.1 M sodium citrate tribasic dihydrate pH 5.6, 35% v/v tert-butanol
66. (F6)	0.01M iron (III) chloride hexahydrate, 0.1M sodium citrate tribasic dihydrate pH 5.6, 10% v/v Jeffamine ® M-600 ®
67. (F7)	0.1 M sodium citrate tribasic dihydrate pH 5.6, 2.5 M 1,6-hexanediol
68. (F8)	0.1 M MES monohydrate pH 6.5, 1.6 M magnesium sulfate heptahydrate
69. (F9)	0.1 M sodium phosphate monobasic monohydrate, 0.1 M potassium phosphate monobasic, 0.1 M MES monohydrate pH 6.5,
70. (F8)	0.1 M MES monohydrate pH 6.5, 12% w/v polyethylene glycol 20,000
71. (F11)	1.6 M ammonium sulfate, 0.1 M MES monohydrate pH 6.5, 10% v/v 1,4-dioxane
72. (F12)	0.05 M cesium chloride, 0.1 M MES monohydrate pH 6.5, 30% v/v Jeffamine ® M-600 ®
73. (G1)	0.01 M cobalt (II) chloride hexahydrate, 0.1 M MES monohydrate pH 6.5, 1.8 M ammonium sulfate
74. (G2)	0.2 M ammonium sulfate, 0.1 M MES monohydrate pH 6.5, 30% w/v PEG monomethyl ether 5,000
75. (G3)	0.01 M zinc sulfate heptahydrate, 0.1 M MES monohydrate pH 6.5, 25% v/v PEG monomethyl ether 550
76. (G4)	1.6 M sodium citrate tribasic dihydrate pH 6.5
77. (G5)	0.5 M ammonium sulfate, 0.1 M HEPES pH 7.5, 30% v/v (+/-)-2-Methyl-2,4-pentanediol
78. (G6)	0.1 M HEPES pH 7.5, 10% w/v polyethylene glycol 6,000, 5% v/v (+/-)-2-methyl-2,4-pentanediol
79. (G7)	0.1 M HEPES pH 7.5, 20% v/v Jeffamine ® M-600 ®
80. (G8)	0.1 M sodium chloride, 0.1 M HEPES pH 7.5, 1.6 M ammonium sulfate
81. (G9)	0.1 M HEPES pH 7.5, 2.0 M ammonium formate
82. (G10)	0.05 M cadmium sulfate hydrate, 0.1 M HEPES pH 7.5, 1.0 M sodium acetate trihydrate
83. (G11)	0.1 M HEPES pH 7.5, 70% v/v (+/-)-2-methyl-2,4-pentanediol
84. (G12)	0.1 M HEPES pH 7.5, 4.3 M sodium chloride
85. (H1)	0.1 M HEPES pH 7.5, 10% w/v polyethylene glycol 8,000, 8% v/v ethylene glycol
86. (H2)	0.1 M HEPES pH 7.5, 20% w/v polyethylene glycol 10,000
87. (H3)	0.2 M magnesium chloride hexahydrate, 0.1 M Tris pH 8.5, 3.4 M 1,6-hexanediol
88. (H4)	0.1 M Tris pH 8.5, 25% v/v tert-butanol
89. (H5)	0.01 M nickel (II) chloride hexahydrate, 0.1 M Tris pH 8.5, 1.0 M lithium sulfate monohydrate

Table A1 continued.

90. (H6)	1.5 M Ammonium sulfate, 0.1 M Tris pH 8.5, 12% v/v Glycerol
91. (H7)	0.2 M Ammonium phosphate monobasic, 0.1 M Tris pH 8.5, 50% v/v (+/-)-2-Methyl-2,4-pentanediol
92. (H8)	0.1 M Tris pH 8.5, 20% v/v Ethanol
93. (H9)	0.01M Nickel (II) chloride hexahydrate, 0.1 M Tris pH 8.5, 20% w/v PEG monomethyl ether 2,000
94. (H10)	0.1 M Sodium chloride, 0.1 M BICINE pH 9.0, 20% v/v Polyethylene glycol monomethyl ether 550
95. (H11)	0.1 M BICINE pH 9.0, 2.0 M Magnesium chloride hexahydrate
96. (H12)	0.1 M BICINE pH 9.0, 2% v/v 1,4-Dioxane, 10% w/v Polyethylene glycol 20,000

Table A2: Hampton Research crystal screen HR2-144 reagent formulation

Reagent #	Formulation
1	0.1 M citric acid pH 3.5, 2.0 M ammonium sulfate
2	0.1 M sodium acetate trihydrate pH 4.5, 2.0 M ammonium sulfate
3	0.1 M BIS-TRIS pH 5.5, 2.0 M ammonium sulfate
4	0.1 M BIS-TRIS pH 6.5, 2.0 M ammonium sulfate
5	0.1 M HEPES pH 7.5, 2.0 M ammonium sulfate
6	0.1 M Tris pH 8.5, 2.0 M ammonium sulfate
7	0.1 M citric acid pH 3.5, 3.0 M sodium chloride
8	0.1 M sodium acetate trihydrate pH 4.5, 3.0 M sodium chloride
9	0.1 M BIS-TRIS pH 5.5, 3.0 M sodium chloride
10	0.1 M BIS-TRIS pH 6.5, 3.0 M sodium chloride
11	0.1 M HEPES pH 7.5, 3.0 M sodium chloride
12	0.1 M Tris pH 8.5, 3.0 M sodium chloride
13	0.1 M BIS-TRIS pH 5.5, 0.3 M magnesium formate dihydrate
14	0.1 M BIS-TRIS pH 6.5, 0.5 M magnesium formate dihydrate
15	0.1 M HEPES pH 7.5, 0.5 M magnesium formate dihydrate
16	0.1 M TRIS pH 8.5, 0.3 M magnesium formate dihydrate
17	1.26 M sodium phosphate monobasic monohydrate, 0.14 M potassium phosphate dibasic, pH 5.6
18	0.49 M sodium phosphate monobasic monohydrate, 0.91 M potassium phosphate dibasic, pH 6.9
19	0.056 M sodium phosphate monobasic monohydrate, 1.344 M potassium phosphate dibasic, pH 8.2
20	0.1 M HEPES pH 7.5, 1.4 M sodium citrate tribasic dihydrate
21	1.8 M ammonium citrate tribasic pH 7.0
22	0.8 M succinic acid pH 7.0
23	2.1 M DL-malic acid pH 7.0
24	2.8 M sodium acetate trihydrate pH 7.0
25	3.5 M sodium formate pH 7.0
26	1.1 M ammonium tartrate dibasic pH 7.0
27	2.4 M sodium malonate pH 7.0
28	35% v/v Tacsimate™ pH 7.0
29	60% v/v Tacsimate™ pH 7.0
30	0.1 M sodium chloride, 0.1 M BIS-TRIS pH 6.5, 1.5 M ammonium sulfate
31	0.8 M potassium sodium tartrate tetrahydrate, 0.1 M Tris pH 8.5, 0.5% w/v polyethylene glycol monomethyl ether 5,000
32	1.0 M ammonium sulfate, 0.1 M BIS-TRIS pH 5.5, 1% w/v polyethylene glycol 3,350
33	1.1 M sodium malonate pH 7.0, 0.1 M HEPES pH 7.0, 0.5% v/v Jeffamine ® ED-2001 pH 7.0
34	1.0 M succinic acid pH 7.0, 0.1 M HEPES pH 7.0, 1% w/v polyethylene glycol monomethyl ether 2,000
35	1.0 M ammonium sulfate, 0.1 M HEPES pH 7.0, 0.5% w/v polyethylene glycol 8,000
36	15% v/v Tacsimate™ pH 7.0, 0.1 M HEPES pH 7.0, 2% w/v polyethylene glycol 3,350
37	25% w/v polyethylene glycol 1,500
38	0.1 M HEPES pH 7.0, 30% v/v Jeffamine ® M-600 ® pH 7.0
39	0.1 M HEPES pH 7.0, 30% v/v Jeffamine ® ED-2001 pH 7.0
40	0.1 M citric acid pH 3.5, 25% w/v polyethylene glycol 3,350
41	0.1 M sodium acetate trihydrate pH 4.5, 25% w/v polyethylene glycol 3,350
42	0.1 M BIS-TRIS pH 5.5, 25% w/v polyethylene glycol 3,350
43	0.1 M BIS-TRIS pH 6.5, 25% w/v polyethylene glycol 3,350
44	0.1 M HEPES pH 7.5, 25% w/v polyethylene glycol 3,350

Table A2 continued

45	0.1 M Tris pH 8.5, 25% w/v polyethylene glycol 3,350
46	0.1 M BIS-TRIS pH 6.5, 20% w/v polyethylene glycol monomethyl ether 5,000
47	0.1 M BIS-TRIS pH 6.5, 28% w/v polyethylene glycol monomethyl ether 2,000
48	0.2 M calcium chloride dihydrate, 0.1 M BIS-TRIS pH 5.5, 45% v/v (+/-)-2-methyl-2,4-pentanediol
49	0.2 M calcium chloride dihydrate, 0.1 M BIS-TRIS pH 6.5, 45% v/v (+/-)-2-methyl-2,4-pentanediol
50	0.2 M ammonium acetate, 0.1 M BIS-TRIS pH 5.5, 45% v/v (+/-)-2-methyl-2,4-pentanediol
51	0.2 M ammonium acetate, 0.1 M BIS-TRIS pH 6.5, 45% v/v (+/-)-2-methyl-2,4-pentanediol
52	0.2 M ammonium acetate, 0.1 M HEPES pH 7.5, 45% v/v (+/-)-2-methyl-2,4-pentanediol
53	0.2 M ammonium acetate, 0.1 M Tris pH 8.5, 45% v/v (+/-)-2-methyl-2,4-pentanediol
54	0.05 M calcium chloride dihydrate, 0.1M BIS-TRIS pH 6.5, 30% v/v PEG monomethyl ether 550
55	0.05M magnesium chloride hexahydrate,0.1M HEPES pH 7.5, 30% v/v PEG monomethyl ether 550
56	0.2 M potassium chloride, 0.05 M HEPES pH 7.5, 35% v/v pentaerythritol propoxylate (5/4 PO/OH)
57	0.05 M ammonium sulfate, 0.05 M BIS-TRIS pH 6.5, 30% v/v pentaerythritol ethoxylate (15/4 EO/OH)
58	0.1 M BIS-TRIS pH 6.5, 45% v/v polypropylene glycol P 400
59	0.02M magnesium chloride hexahydrate,0.1M HEPES pH 7.5, 22% w/v poly (acrylic acid sodium salt) 5,100
60	0.01 M cobalt (II) chloride hexahydrate, 0.1 M Tris pH 8.5, 20% w/v polyvinylpyrrolidone K 15
61	0.2 M L-proline, 0.1 M HEPES pH 7.5, 10% w/v polyethylene glycol 3,350
62	0.2 M trimethylamine N-oxide dihydrate, 0.1 M Tris pH 8.5, 20% w/v PEG monomethyl ether 2,000
63	5% v/v Tacsimate™ pH 7.0, 0.1 M HEPES pH 7.0, 10% w/v polyethylene glycol monomethyl ether 5,000
64	0.005M cobalt (II) chloride hexahydrate,0.005M Nickel (II) chloride hexahydrate,0.005M cadmium chloride hydrate,
65	0.1 M ammonium acetate, 0.1 M BIS-TRIS pH 5.5, 17% w/v polyethylene glycol 10,000
66	0.2 M ammonium sulfate, 0.1 M BIS-TRIS pH 5.5, 25% w/v polyethylene glycol 3,350
67	0.2 M ammonium sulfate, 0.1 M BIS-TRIS pH 6.5, 25% w/v polyethylene glycol 3,350
68	0.2 M ammonium sulfate, 0.1 M HEPES pH 7.5, 25% w/v polyethylene glycol 3,350
69	0.2 M ammonium sulfate, 0.1 M Tris pH 8.5, 25% w/v polyethylene glycol 3,350
70	0.2 M sodium chloride, 0.1 M BIS-TRIS pH 5.5, 25% w/v polyethylene glycol 3,350
71	0.2 M sodium chloride, 0.1 M BIS-TRIS pH 6.5, 25% w/v polyethylene glycol 3,350
72	0.2 M sodium chloride, 0.1 M HEPES pH 7.5, 25% w/v polyethylene glycol 3,350
73	0.2 M sodium chloride, 0.1 M Tris pH 8.5, 25% w/v polyethylene glycol 3,350
74	0.2 M lithium sulfate monohydrate, 0.1 M BIS-TRIS pH 5.5, 25% w/v polyethylene glycol 3,350
75	0.2 M lithium sulfate monohydrate, 0.1 M BIS-TRIS pH 6.5, 25% w/v polyethylene glycol 3,350
76	0.2 M lithium sulfate monohydrate, 0.1 M HEPES pH 7.5, 25% w/v polyethylene glycol 3,350
77	0.2 M lithium sulfate monohydrate, 0.1 M Tris pH 8.5, 25% w/v polyethylene glycol 3,350
78	0.2 M ammonium acetate, 0.1 M BIS-TRIS pH 5.5, 25% w/v polyethylene glycol 3,350
79	0.2 M ammonium acetate, 0.1 M BIS-TRIS pH 6.5, 25% w/v polyethylene glycol 3,350
80	0.2 M ammonium acetate, 0.1 M HEPES pH 7.5, 25% w/v polyethylene glycol 3,350
81	0.2 M ammonium acetate, 0.1 M Tris pH 8.5, 25% w/v polyethylene glycol 3,350
82	0.2 M magnesium chloride hexahydrate, 0.1 M BIS-TRIS pH 5.5, 25% w/v polyethylene glycol 3,350
83	0.2 M magnesium chloride hexahydrate, 0.1 M BIS-TRIS pH 6.5, 25% w/v polyethylene glycol 3,350
84	0.2 M magnesium chloride hexahydrate, 0.1 M HEPES pH 7.5, 25% w/v polyethylene glycol 3,350
85	0.2 M magnesium chloride hexahydrate, 0.1 M Tris pH 8.5, 25% w
86	0.2 M potassium sodium tartrate tetrahydrate, 20% w/v polyethylene glycol 3,350
87	0.2 M sodium malonate pH 7.0, 20% w/v polyethylene glycol 3,350
88	0.2 M ammonium citrate tribasic pH 7.0, 20% w/v polyethylene glycol 3,350
89	0.1 M succinic acid pH 7.0, 15% w/v polyethylene glycol 3,350
90	0.2 M sodium formate, 20% w/v polyethylene glycol 3,350
91	0.15 M DL-malic acid pH 7.0, 20% w/v polyethylene glycol 3,350
92	0.1 M magnesium formate dihydrate, 15% w/v polyethylene glycol 3,350
93	0.05 M zinc acetate dihydrate, 20% w/v polyethylene glycol 3,350
94	0.2 M sodium citrate tribasic dihydrate, 20% w/v polyethylene glycol 3,350
95	0.1 M potassium thiocyanate, 30% w/v polyethylene glycol monomethyl ether 2,000
96	0.15 M potassium bromide, 30% w/v polyethylene glycol monomethyl ether 2,000

Table A3: ProPlex HT crystal screen MD1-38 reagent formulation

Reagent #	Formulation
A1	0.1M Tris pH8.0 25%v/v PEG 350MME
A2	0.1M calcium acetate hydrate 0.1M MES pH6.0 15%v/v PEG 400
A3	0.1M lithium chloride 0.1M sodium HEPES pH7.5 20%v/v PEG 400
A4	0.1M Tris pH8.0 25%v/v PEG 400
A5	0.1M MES pH6.5 15%v/v PEG 500MME
A6	0.2M sodium chloride 0.1M sodium/potassium phosphate pH6.5 25%w/v PEG 1000
A7	0.1M ammonium sulfate 0.1M Tris pH7.5 20%w/v PEG 1500
A8	0.2M ammonium sulfate 0.1M sodium acetate pH5.5 10%w/v PEG 2000MME
A9	0.2M sodium chloride 0.1M MES pH6.0 20%w/v PEG 2000MME
A10	0.1M potassium chloride 0.1M Tris pH8.0 15%w/v PEG 2000MME
A11	0.1M sodium HEPES pH7.5 25%w/v PEG 2000MME
A12	0.2M sodium acetate trihydrate 0.1M Sodium citrate pH5.5 5%w/v PEG 4000
B1	0.2M lithium sulfate 0.1M Tris pH7.5 5%w/v PEG 4000
B2	0.1M calcium acetate hydrate 0.1M sodium acetate pH4.5 10 % w/v PEG 4000
B3	0.2M sodium acetate trihydrate 0.1M sodium citrate pH5.5 10%w/v PEG 4000
B4	0.2M sodium chloride 0.1M MES pH6.5 10%w/v PEG 4000
B5	0.1M magnesium chloride hexahydrate 0.1M Sodium HEPES pH7.5 10%w/v PEG 4000
B6	0.1M sodium HEPES pH7.0 10%w/v PEG 4000 10%v/v 2-propanol
B7	0.2M ammonium acetate 0.1M sodium acetate pH4.0 15%w/v PEG 4000
B8	0.1M magnesium chloride hexahydrate 0.1M sodium citrate pH5.0 15%w/v PEG 4000
B9	0.1M sodium cacodylate pH6.0 15%w/v PEG 4000
B10	0.15M ammonium sulfate 0.1M MES pH6.0 15%w/v PEG 4000
B11	0.1M sodium HEPES pH7.0 15%w/v PEG 4000
B12	0.1M magnesium chloride hexahydrate 0.1M sodium HEPES pH7.0 15%w/v PEG 4000
C1	0.15M ammonium sulfate 0.1M Tris pH8.0 15%w/v PEG 4000
C2	0.1M sodium citrate pH4.5 20%w/v PEG 4000
C3	0.2M ammonium acetate 0.1M sodium acetate pH5.0 20%w/v PEG 4000
C4	0.2M lithium sulfate 0.1M MES pH6.0 20%w/v PEG 4000
C5	0.1M Tris pH8.0 20%w/v PEG 4000
C6	0.15M ammonium sulfate 0.1M Sodium HEPES pH7.0 20%w/v PEG 4000
C7	0.1M sodium citrate pH5.6 20%w/v PEG 4000 20%v/v 2-propanol
C8	0.2M sodium chloride 0.1M Tris pH8.0 20%w/v PEG 4000
C9	0.1M sodium cacodylate pH5.5 25%w/v PEG 4000
C10	0.15M ammonium sulfate 0.1M MES pH5.5 25%w/v PEG 4000
C11	0.1M sodium cacodylate pH6.5 25%w/v PEG 4000
C12	0.2M potassium iodide 0.1M MES pH6.5 25%w/v PEG 4000
D1	0.2M sodium chloride 0.1M sodium HEPES pH7.5 25%w/v PEG 4000
D2	0.1M MES pH6.5 10%w/v PEG 5000 MME 12%v/v 1-propanol
D3	0.1M potassium chloride 0.1M Sodium HEPES pH7.0 15%w/v PEG 5000MME
D4	0.2M ammonium sulfate 0.1M Tris pH7.5 20%w/v PEG 5000MME
D5	0.1M magnesium chloride hexahydrate 0.1M MES pH6.0 8%w/v PEG 6000
D6	0.15M sodium chloride 0.1M Tris pH8.0 8%w/v PEG 6000
D7	0.1M sodium citrate pH5.5 15%w/v PEG 6000
D8	0.1M magnesium acetate tetrahydrate 0.1M sodium cacodylate pH6.5 15%w/v PEG 6000
D9	0.1M MES pH6.5 15%w/v PEG 6000 5%v/v MPD
D10	0.1M potassium chloride 0.1M sodium HEPES pH7.5 15%w/v PEG 6000
D11	0.1M Tris pH8.5 15%w/v PEG 6000
D12	0.1M Tris pH8.5 20%w/v PEG 6000
E1	0.1M magnesium acetate tetrahydrate 0.1M sodium acetate pH4.5 8%w/v PEG 8000
E2	0.1M sodium citrate pH5.0 8%w/v PEG 8000
E3	0.2M sodium chloride 0.1M sodium cacodylate pH6.0 8%w/v PEG 8000
E4	0.1M sodium HEPES pH7.0 8%w/v PEG 8000
E5	0.1M Tris pH8.0 8%w/v PEG 8000
E6	0.1M calcium acetate hydrate 0.1M sodium cacodylate pH5.5 12%w/v PEG 8000
E7	0.1M sodium phosphate pH6.5 12%w/v PEG 8000
E8	0.1M magnesium acetate tetrahydrate 0.1M MOPS pH7.5 12%w/v PEG 8000
E9	0.2M sodium chloride 0.1M sodium HEPES pH7.5 12%w/v PEG 8000

Table A3 continued.

E10	0.2M ammonium sulfate 0.1M Tris pH8.5 12%w/v PEG 8000
E11	0.1M sodium citrate pH5.0 20%w/v PEG 8000
E12	0.2M ammonium sulfate 0.1M MES pH6.5 20%w/v PEG 8000
F1	0.1M sodium HEPES pH7.0 20%w/v PEG 8000
F2	0.2M lithium chloride 0.1M Tris pH8.0 20%w/v PEG 8000
F3	0.1M magnesium acetate tetrahydrate 0.1M MES pH6.5 10%w/v PEG 10,000
F4	0.1M sodium HEPES pH7.0 18%w/v PEG 12,000
F5	0.1M sodium chloride 0.1M Tris pH8.0 8%w/v PEG 20,000
F6	0.1M sodium HEPES pH7.0 15%w/v PEG 20,000
F7	0.5M ammonium sulfate 0.1M MES pH6.5
F8	1.0M ammonium sulfate 0.1M sodium acetate pH5.0
F9	1.0M ammonium sulfate 0.1M MES pH6.5
F10	1.0M ammonium sulfate 0.1M Tris pH8.0
F11	1.5M ammonium sulfate 0.1M sodium acetate pH5.0
F12	1.5M ammonium sulfate 0.1M sodium HEPES pH7.0
G1	1.5M ammonium sulfate 0.1M Tris pH8.0
G2	2.0M ammonium sulfate 0.1M sodium acetate pH5.0
G3	2.0M ammonium sulfate 0.1M sodium HEPES pH7.0
G4	2.0M ammonium sulfate 0.1M Tris pH8.0
G5	1.0M ammonium sulfate 0.1M sodium HEPES pH7.0 1.0M potassium chloride
G6	2.0M sodium formate 0.1M sodium acetate pH5.0
G7	3.0M sodium formate 0.1M Tris pH7.5
G8	0.8M sodium/potassium phosphate pH7.5
G9	1.3M sodium/potassium phosphate pH7.0
G10	1.6M sodium/potassium phosphate pH6.5
G11	1.0M sodium acetate trihydrate 0.1M sodium HEPES pH7.5
G12	1.0M sodium citrate tribasic dihydrate 0.1M sodium HEPES pH7.0
H1	2.0M sodium chloride 0.1M sodium citrate pH6.0
H2	1.0M lithium sulfate 0.1M MES pH6.5
H3	1.6M lithium sulfate 0.1M Tris pH8.0
H4	1.4M sodium malonate dibasic monohydrate pH6.0
H5	1.2M potassium sodium tartrate tetrahydrate 0.1M Tris pH8.0
H6	1.6M magnesium sulfate heptahydrate 0.1M MES pH6.5
H7	0.1M sodium acetate pH5.0 2%w/v PEG 4000 15%v/v MPD
H8	0.05M calcium acetate hydrate 0.1M sodium cacodylate pH6.0 25%v/v MPD
H9	0.1M imidazole pH7.0 50%v/v MPD
H10	0.05M magnesium chloride hexahydrate 0.1M MES pH6.5 5%w/v PEG 4000 10%v/v 2-propanol
H11	0.2M ammonium acetate 0.1M sodium HEPES pH7.5 25%v/v 2-propanol
H12	0.1M sodium chloride 0.1M Tris pH8.0 15%v/v ethanol 5%v/v MPD

APPENDIX III: Media and buffers for NMR sample preparation

To prepare 1 L LB-medium

10 g NaCl

10 g Tryptone

5 g Yeast extracts

Add deionized H₂O to 1 L and autoclave

To prepare 5X M9 solution

64 g Na₂HPO₄·7H₂O

15 g KH₂PO₄

2.5 g NaCl

Add deionized H₂O to final 1 L volume and autoclave

To prepare 1 L solution Q

8 ml HCl (5 M)

5 g FeCl₂

185 mg CaCl₂

64 mg H₃BO₃

18 mg CoCl₂

4 mg CuCl₂

605 mg Na₂MoO₄

40 mg MnCl₂·4(H₂O)

Total volume of solubilization is 1 L.

To prepare 1 L minimal media for ¹³C/¹⁵N labelling

200 mL 5X M9 solution

2 mL 1 M MgSO₄

100 μL 1M CaCl₂

10 mL 100X vitamin solution

20 mL ¹⁵NH₄(Cl)₂

20 mL 20% D-glucose (¹³C-labelled)

4 mL Solution Q

Antibiotics (kanamycin and chloramphenicol)

Autoclaved H₂O to 1L

To prepare 1 L minimal media for ²D/¹³C/¹⁵N labelling

100 mL 10X M9 Solution (prepared with D₂O)

2 mL 1 M MgSO₄ (prepared with D₂O)

100 μL 1 M CaCl₂

10 mL 100X Vitamin Solution

20 mL ¹⁵NH₄(Cl)₂

20 mL 20% D-glucose (¹³C-labelled)

4 mL solution Q

Antibiotics (kanamycin and chloramphenicol)

Filter sterilized D₂O to 1 L

Protein purification buffers ((αX I-domain)

Lysis buffer: 20 mM Tris pH 8.0, 200 mM NaCl

Affinity chromatography (5 ml HisTrap Column):

Running buffer: 20 mM Tris pH 8.0, 40 mM imidazole, 300 mM NaCl, 10% glycerol at 4 °C

Elution buffer: 20 mM Tris pH 8.0, 500 mM imidazole, 300 mM NaCl, 10% glycerol at 4 °C

Gel filtration chromatography (HiLoad Superdex75 16/60):

Running buffer: 20 mM MES pH 6.6, 150 mM NaCl, 5 mM MgCl₂ at 4 °C

Table A4: Chemical shift Table of α X I-domain

Residue	N	HN	Ca	Cb	C'
Q131	119.244	7.961	34.542	58.328	166.841
D132	127.996	9.009	36.338	48.121	167.847
I133	122.245	8.274	28.884	51.808	168.764
L136	127.052	9.549	36.054	44.366	
D138	125.164	8.387	32.752		170.134
G139	115.518	7.858	42.966		
S140	115.653	9.463	30.674		169.383
G141	104.364	8.546	43.216		168.04
I143	126.249	7.582	26.775		169.843
S144	123.685	8.508	24.197	31.937	168.629
S145	116.981	9.021	27.438	26.596	172.564
R146	122.175	8.353	30.271	59.583	172.572
N147	119.131	7.514	34.102	52.043	170.467
F148	123.732	9.021	26.588	50.558	171.433
A149	120.268	7.676	33.635	72.097	175.027
T150	118.343	8.088	22.687	21.5	171.657
M151	124.862	8.527	29.214	57.26	171.897
M152	117.646	8.174	33.64	61.504	173.765
N153	119.777	8.252	33.53	51.822	172.208
F154	123.928	7.759	28.576	51.311	169.595
R156	121.933	8.766	32.254		167.182
A157	109.725	8.17	33.072		168.968
I159	118.608	8.087	23.355		173.114
S160	111.514	7.838	28.185	25.54	168.926
Q161	118.434	7.79	33.2	60.47	169.313
F162	118.189	7.745	31.637	47.3	169.498
Q163	120.425	9.136	33.499	58.576	170.242
R164	122.71	8.747	34.366	58.805	170.343
S166	120.235	8.483	25.409	26.923	171.437
S167			25.106	19.914	167.261
Q168	129.577	8.943	33.275	55.709	168.762

Table A4 continued.

S170	108.884	8.02	33.408	24.901	165.955
L171	124.964	6.694	35.435	43.306	168
M172	128.514	9.198	35.622	51.925	166.73
Q173	128.931	9.465	36.515	56.924	167.902
F174	124.301	9.506	34.379	43.656	165.825
S175	118.19	8.788	31.208	26.802	170.141
N176	119.379	8.499	35.423	51.219	166.575
K177	119.356	7.208	35.606	54.386	167.652
F178	115.73	8.256	32.901	48.295	169.377
Q179	123.8	9	34.168	57.978	168.379
T180	127.092	9.221	26.164	21.884	168.657
H181	129.563	8.58	29.864	60.39	170.401
F182	108.155	6.978	33.056	49.351	169.823
T183	116.185	9.38	29.164	18.108	168.99
F184	119.794	8.544	27.563	50.588	172.5
E185	118.116	8.135	30.318	60.219	172.858
E186	118.234	7.852	30.055	59.27	173.886
F187	121.21	8.631	26.879	48.664	171.882
R188	119.635	9.011	30.163	59.679	172.629
R189	114.167	7.849	32.335	58.602	171.137
S190	113.24	7.035	30.518	25.248	170.333
N192	116.384	8.033	38.435	51.079	167.371
L194	115.021	7.958	31.961	49.947	175.092
S195	115.646	7.984	27.969	25.994	171.104
L196	122.009	7.449	32.658	48.533	172.781
L197	114.995	7.141	33.58	48.635	171.851
A198	120.896	7.29	34.819	70.832	172.314
S199	110.264	7.542	31.804	25.818	167.735
V200	122.444	7.062	26.076	58.194	168.701
H201	126.384	8.296	35.521	58.551	169.046
Q202	127.541	8.624	33.386	62.209	171.968
L203	128.812	9.484	36.515	45.62	175.157
Q204	107.929	7.357	31.149	62.918	168.763
G205	104.17	7.948	45.056		169.435
Y208	128.567	8.871	35.842	55.202	171.37

Table A4 continued.

T209	111.749	7.531	23.542	20.699	170.968
A210	120.328	7.678	33.635	72.079	175.027
T211	121.032	10.448	21.321	22.074	171.181
A212	123.433	8.265	33.229	70.018	172.962
I213	117.778	7.862	23.003	51.874	171.402
Q214	120.587	8.215	29.259	60.946	171.57
N215	116.584	7.808	32.63	50.259	171.998
V216	120.6	8.02	22.136	58.244	171.023
V217	116.336	8.139	22.407	60.307	171.603
H218	112.824	8.197	31.406	57.844	170.874
R219	113.982	7.841	32.335	58.602	169.668
L220	114.838	7.036	30.452	49.086	172.352
F221	110.061	7.219	30.386	51.516	168.369
H222	121.564	7.679	30.997	56.533	171.88
A223	131.596	8.623	33.744	70.933	175.921
S224	117.99	10.748	27.54		170.275
Y225	123.913	8.292	31.222	51.612	170.281
G226	104.828	8.207	43.817		168.839
A227	123.907	7.208	36.577	70.334	123.907
R228	126.215	0.086	33.314	58.496	171.722
R229	125.543	8.607	29.902	59.178	171.816
D230	115.111	8.636	35.088		169.842
A231	121.359	6.89	37.167	69.717	171.822
T232	120.127	8.633	25.156	23.948	
L235	129.089	9.593	36.634		167.839
I236	127.092	9.342	28.52		167.902
V237	127.671	8.97	28.105		
G241	111.161	8.629	44.746		
K243	124.228	9.601	31.579	57.882	171.791
E244	127.558	8.883	32.703	56.585	169.489
G245	112.857	8.66	43.717		166.493
D246	120.18	6.751	36.344	46.669	171.246
S247	122.648	8.424	29.209	25.928	168.337
L248	122.575	7.97	35.756	45.909	169.501
Y250	122.101	8.454	26.253	53.086	173.093

Table A4 continued.

K251	117.322	8.869	30.908	58.609	170.397
D252	115.418	7.378	33.171	46.541	171.225
V253	112.353	7.523	27.053	54.978	169.49
I254	123.344	8.739	26.604	57.234	169.474
M256	115.572	7.561	30.813	57.866	173.017
A257	123.719	7.754	34.344	72.015	173.154
D258	118.397	8.586	31.903	49.777	174.933
A259	124.015	8.237	34.422	71.817	173.142
A260	117.476	7.191	37.347	70.419	171.369
G261	106.859	7.751	43.283		168.681
I262	119.046	7.479	28.139	51.095	169.723
I263					
R264	124.558	8.898	34.931	58.623	169.954
Y265	121.649	9.434	32.242	47.832	168.809
A266	123.054	8.727	38.753	66.861	168.378
I267	124.02	9.359	29.126	51.308	168.41
G268	112.729	8.536	44.013		166.366
V269	125.005	8.673	28.95	55.736	171.159
G270	109.924	7.928	44.51		170.472
L271	119.9	8.639	31.574	47.324	173.612
A272	121.259	9.065	37.364	71.02	173.268
F273	110.808	7.139	31.657	51.125	169.752
Q274	118.034	7.474	31.654	60.146	170.767
N275	116.058	8.019	36.551	49.432	170.213
N277	117.463	8.59	33.734	51.722	171.499
S278	115.821	7.991	28.613	24.733	170.235
W279	122.166	7.642	30.73	61.096	171.914
K280	120.213	7.875	29.742	57.509	171.286
E281	118.04	7.505	29.599	59.779	172.052
L282	112.863	6.812	32.157	49.771	172.744
N283	117.033	7.76	33.558	51.19	171.43
D284	118.541	8.153	32.645	49.152	172.929
I285	119.113	6.917	25.094	49.44	170.197
A286	119.477	7.558	36.836	68.07	172.616
S287	119.08	8.357	28.278	27.35	165.66
K288	118.338	8.236	35.505	57.653	170.187

Table A4 continued.

S291	115.646	7.984	27.969	25.994	171.658
E292	113.397	7.012	33.257	59.295	170.235
H293	114.302	7.76	32.777	58.201	165.863
I294	115.741	6.692	29.607	47.387	169.364
F295	122.511	8.946	32.55	46.808	167.646
K296	122.754	8.64	33.949	57.268	169.83
V297	120.532	8.607	29.458	55.241	171.012
E298	125.687	9.325	29.332	59.36	169.397
D299	110.25	7.1	36.645	47.281	169.969
F300	117.084	8.691	26.463	50.817	172.49
D301	119.774	8.373	32.156	49.227	169.891
A302	119.765	7.55	37.197	70.185	173.389
L303	121.34	7.476	31.249	49.815	172.449
K304	113.957	8.026	31.017	58.44	172.237
D305	119.052	7.481	32.898	48.676	172.2
I306	110.596	7.711	28.221	51.156	17.656
Q307	120.818	7.231	28.885	60.483	171.314
N308	116.858	8.694	33.404	51.817	171.582
Q309	120.66	8.165	30.269	60.267	172.854
L310	119.418	8.167	30.988	48.316	171.488
K311	117.493	7.587	28.915	58.091	171.612
E312	116.35	8.152	29.855	60.307	174.328
K313	118.663	7.98	29.884	57.726	173.65
I314	119.82	7.851	24.368	51.566	173.288
F315	116.787	7.969	29.206	59.166	171.884
A316	121.594	7.881	34.329	71.695	175.184
E318	121.805	8.477	32.851	58.952	171.27
G319	110.113	8.481	43.982		168.273

Bibliography

- Abram, C.L., and Lowell, C.A. (2009). The ins and outs of leukocyte integrin signaling. *Annu Rev Immunol* 27, 339-362.
- Adair, B.D., and Yeager, M. (2002). Three-dimensional model of the human platelet integrin alpha IIb beta 3 based on electron cryomicroscopy and x-ray crystallography. *Proc Natl Acad Sci U S A* 99, 14059-14064.
- Adams, P.D., Afonine, P.V., Bunkóczi, G., Chen, V.B., Davis, I.W., Echols, N., Headd, J.J., Hung, L.-W., Kapral, G.J., and Grosse-Kunstleve, R.W. (2010). PHENIX: a comprehensive Python-based system for macromolecular structure solution. *Acta Crystallogr Sect D Biol Crystallogr* 66, 213-221.
- Ajroud, K., Sugimori, T., Goldmann, W.H., Fathallah, D.M., Xiong, J.-P., and Arnaout, M.A. (2004). Binding affinity of metal ions to the CD11b A-domain is regulated by integrin activation and ligands. *J Biol Chem* 279, 25483-25488.
- Alonso, J.L., Essafi, M., Xiong, J.P., Stehle, T., and Arnaout, M.A. (2002). Does the integrin alphaA domain act as a ligand for its betaA domain? *Curr Biol* 12, R340-342.
- Altieri, D.C. (1991). Occupancy of CD11b/CD18 (Mac-1) divalent ion binding site (s) induces leukocyte adhesion. *J Immunol* 147, 1891-1898.
- Arnaout, M.A. (1990). Structure and function of the leukocyte adhesion molecules CD11/CD18. *Blood* 75, 1037-1050.
- Arnaout, M.A. (2016). Biology and structure of leukocyte β 2 integrins and their role in inflammation. *F1000Research* 5.
- Arora, M., Chen, L., Paglia, M., Gallagher, I., Allen, J.E., Vyas, Y.M., Ray, A., and Ray, P. (2006). Simvastatin promotes Th2-type responses through the induction of the chitinase family member Ym1 in dendritic cells. *Proc Natl Acad Sci U S A* 103, 7777-7782.
- Aziz, M.H., Cui, K., Das, M., Brown, K.E., Ardell, C.L., Febbraio, M., Pluskota, E., Han, J., Wu, H., Ballantyne, C.M., *et al.* (2017). The Upregulation of Integrin alphaDbeta2 (CD11d/CD18) on Inflammatory Macrophages Promotes Macrophage Retention in Vascular Lesions and Development of Atherosclerosis. *J Immunol* 198, 4855-4867.
- Bajic, G., Yatime, L., Sim, R.B., Vorup-Jensen, T., and Andersen, G.R. (2013). Structural insight on the recognition of surface-bound opsonins by the integrin I domain of complement receptor 3. *Proc Natl Acad Sci U S A* 110, 16426-16431.
- Baker, N.A., Sept, D., Joseph, S., Holst, M.J., and McCammon, J.A. (2001). Electrostatics of nanosystems: application to microtubules and the ribosome. *Proc Natl Acad Sci U S A* 98, 10037-10041.

- Baldwin, E.T., Sarver, R.W., Bryant, G.L., Curry, K.A., Fairbanks, M.B., Finzel, B.C., Garlick, R.L., Heinrikson, R.L., Horton, N.C., Kelley, L.-L.C., *et al.* (1998). Cation binding to the integrin CD11b I domain and activation model assessment. *Structure* 6, 923-935.
- Battye, T.G.G., Kontogiannis, L., Johnson, O., Powell, H.R., and Leslie, A.G. (2011). iMOSFLM: a new graphical interface for diffraction-image processing with MOSFLM. *Acta Crystallogr Sect D Biol Crystallogr* 67, 271-281.
- Bechard, D., Scherpereel, A., Hammad, H., Gentina, T., Tsicopoulos, A., Aumercier, M., Pestel, J., Dessaint, J.P., Tonnel, A.B., and Lassalle, P. (2001). Human endothelial-cell specific molecule-1 binds directly to the integrin CD11a/CD18 (LFA-1) and blocks binding to intercellular adhesion molecule-1. *J Immunol* 167, 3099-3106.
- Bilsland, C., Diamond, M.S., and Springer, T.A. (1994). The leukocyte integrin p150, 95 (CD11c/CD18) as a receptor for iC3b. Activation by a heterologous beta subunit and localization of a ligand recognition site to the I domain. *J Immunol* 152, 4582-4589.
- Blackford, J., Reid, H.W., Pappin, D.J., Bowers, F.S., and Wilkinson, J.M. (1996). A monoclonal antibody, 3/22, to rabbit CD11c which induces homotypic T cell aggregation: evidence that ICAM-1 is a ligand for CD11c/CD18. *Eur J Immunol* 26, 525-531.
- Boivin, S., Kozak, S., and Meijers, R. (2013). Optimization of protein purification and characterization using Thermofluor screens. *Protein Expr Purif* 91, 192-206.
- Bond, C.S. (2003). TopDraw: a sketchpad for protein structure topology cartoons. *Bioinformatics* 19, 311-312.
- Bruce, D., Cardew, E., Freitag-Pohl, S., and Pohl, E. (2019). How to Stabilize Protein: Stability Screens for Thermal Shift Assays and Nano Differential Scanning Fluorimetry in the Virus-X Project. *J Vis Exp* 144, e58666.
- Burridge, K., and Chrzanowska-Wodnicka, M. (1996). Focal adhesions, contractility, and signaling. *Annu Rev Cell Dev Biol* 12, 463-518.
- Calderwood, D.A., Yan, B., de Pereda, J.M., Alvarez, B.G., Fujioka, Y., Liddington, R.C., and Ginsberg, M.H. (2002). The phosphotyrosine binding-like domain of talin activates integrins. *J Biol Chem* 277, 21749-21758.
- Campbell, I.D., and Humphries, M.J. (2011). Integrin structure, activation, and interactions. *Cold Spring Harb Perspect Biol* 3, 1-14.
- Cavanagh, J., Fairbrother, W., Palmer, A., Skelton, N., and Rance, M. (2007). *spectroscopy: Principles and practice* (Academic Press Amsterdam and Boston, MA).
- Cavanagh, J., Fairbrother, W.J., Palmer III, A.G., and Skelton, N.J. (1995). *Protein NMR spectroscopy: principles and practice* (Elsevier).

- Celik, E., Faridi, M.H., Kumar, V., Deep, S., Moy, V.T., and Gupta, V. (2013). Agonist leukadherin-1 increases CD11b/CD18-dependent adhesion via membrane tethers. *Biophys J* 105, 2517-2527.
- Chandra, R.K. (1984). Excessive intake of zinc impairs immune responses. *JAMA* 252, 1443-1446.
- Chen, V.B., Arendall, W.B., Headd, J.J., Keedy, D.A., Immormino, R.M., Kapral, G.J., Murray, L.W., Richardson, J.S., and Richardson, D.C. (2010a). MolProbity: all-atom structure validation for macromolecular crystallography. *Acta Crystallogr Sect D Biol Crystallogr* 66, 12-21.
- Chen, X., Xie, C., Nishida, N., Li, Z., Walz, T., and Springer, T.A. (2010b). Requirement of open headpiece conformation for activation of leukocyte integrin $\alpha X\beta 2$. *Proc Natl Acad Sci U S A* 107, 14727-14732.
- Chouhan, B.S., K pyl , J., Denessiouk, K., Denesyuk, A., Heino, J., and Johnson, M.S. (2014). Early chordate origin of the vertebrate integrin αI domains. *PLoS One* 9, e112064.
- Cowtan, K. (2001). *Phase Problem in X-ray Crystallography, and Its Solution*. eLS Chichester: John Wiley & Sons Ltd.
- Critchley, D.R., Holt, M.R., Barry, S.T., Priddle, H., Hemmings, L., and Norman, J. (1999). Integrin-mediated cell adhesion: the cytoskeletal connection. *Biochem Soc Symp* 65, 79-99.
- Cuatrecasas, P. (1974). Membrane receptors. *Annu Rev Biochem* 43, 169-214.
- Danielson, M.A., and Falke, J.J. (1996). Use of ^{19}F NMR to probe protein structure and conformational changes. *Annu Rev Biophys Biomol Struct* 25, 163-195.
- Davis, G.E. (1992). The Mac-1 and p150,95 beta 2 integrins bind denatured proteins to mediate leukocyte cell-substrate adhesion. *Exp Cell Res* 200, 242-252.
- Davis, I.W., Murray, L.W., Richardson, J.S., and Richardson, D.C. (2004). MOLPROBITY: structure validation and all-atom contact analysis for nucleic acids and their complexes. *Nucleic Acids Res* 32, W615-W619.
- Day, E.S., Osborn, L., and Whitty, A. (2002). Effect of divalent cations on the affinity and selectivity of alpha4 integrins towards the integrin ligands vascular cell adhesion molecule-1 and mucosal addressin cell adhesion molecule-1: Ca^{2+} activation of integrin alpha4beta1 confers a distinct ligand specificity. *Cell Commun Adhes* 9, 205-219.
- de Azevedo-Quintanilha, I.G., Vieira-de-Abreu, A., Ferreira, A.C., Nascimento, D.O., Siqueira, A.M., Campbell, R.A., Ferreira, T.P.T., Gutierrez, T.M., Ribeiro, G.M., and e Silva, P.M. (2016). Integrin $\alpha D \beta 2$ (CD11d/CD18) mediates experimental malaria-associated acute respiratory distress syndrome (MA-ARDS). *Malar J* 15, 1-15.
- DeLano, W.L. (2002). Pymol: An open-source molecular graphics tool. *CCP4 Newsletter on protein crystallography* 40, 82-92.

- Diamond, M.S., Garcia-Aguilar, J., Bickford, J.K., Corbi, A.L., and Springer, T.A. (1993). The I domain is a major recognition site on the leukocyte integrin Mac-1 (CD11b/CD18) for four distinct adhesion ligands. *J Cell Biol* *120*, 1031-1043.
- Diederichs, K. (2010). Quantifying instrument errors in macromolecular X-ray data sets. *Acta Crystallogr Sect D Biol Crystallogr* *66*, 733-740.
- DMSc, M.S., and Kusuya Nishioka, M. (1998). Physiologic role of the complement system in host defense, disease, and malnutrition. *Nutrition* *14*, 391-398.
- Dransfield, I., Cabanas, C., Craig, A., and Hogg, N. (1992). Divalent cation regulation of the function of the leukocyte integrin LFA-1. *J Cell Biol* *116*, 219-226.
- Dransfield, I., and Hogg, N. (1989). Regulated expression of Mg²⁺ binding epitope on leukocyte integrin alpha subunits. *EMBO J* *8*, 3759-3765.
- Emsley, J., Knight, C.G., Farndale, R.W., Barnes, M.J., and Liddington, R.C. (2000). Structural basis of collagen recognition by integrin alpha2beta1. *Cell* *101*, 47-56.
- Emsley, P., and Cowtan, K. (2004). Coot: model-building tools for molecular graphics. *Acta Crystallogr Sect D Biol Crystallogr* *60*, 2126-2132.
- Fagerholm, S.C., Guenther, C., Lloret Asens, M., Savinko, T., and Uotila, L.M. (2019). Beta2-integrins and interacting proteins in leukocyte trafficking, immune suppression, and immunodeficiency disease. *Front Immunol* *10*, 254-263.
- Fischer, A., Lisowska-Grospierre, B., Anderson, D., and Springer, T. (1988). Leukocyte adhesion deficiency: molecular basis and functional consequences. *Immunodeficiency Rev* *1*, 39-54.
- Freire, E., Mayorga, O.L., and Straume, M. (1990). Isothermal titration calorimetry. *Anal Chem* *62*, 950A-959A.
- Gahmberg, C.G., Fagerholm, S.C., Nurmi, S.M., Chavakis, T., Marchesan, S., and Gronholm, M. (2009). Regulation of integrin activity and signalling. *Biochim Biophys Acta* *1790*, 431-444.
- Gahmberg, C.G., Tolvanen, M., and Kotovuori, P. (1997). Leukocyte adhesion: Structure and function of human leukocyte β 2-integrins and their cellular ligands. *Eur J Biochem* *245*, 215-232.
- Gaither, T.A., Vargas, I., Inada, S., and Frank, M.M. (1987). The complement fragment C3d facilitates phagocytosis by monocytes. *Immunology* *62*, 405-411.
- Galon, J., Gauchat, J.F., Mazières, N., Spagnoli, R., Storkus, W., Lötze, M., Bonnefoy, J.Y., Fridman, W.H., and Sautès, C. (1996). Soluble Fc γ receptor type III (Fc γ RIII, CD16) triggers cell activation through interaction with complement receptors. *J Immunol* *157*, 1184-1192.
- Garnotel, R., Rittié, L., Poitevin, S., Monboisse, J.C., Nguyen, P., Potron, G., Maquart, F.X., Randoux, A., and Gillery, P. (2000). Human blood monocytes interact with type I collagen through alpha x beta 2 integrin (CD11c-CD18, gp150-95). *J Immunol* *164*, 5928-5934.

- Grayson, M.H., Van der Vieren, M., Sterbinsky, S.A., Michael Gallatin, W., Hoffman, P.A., Staunton, D.E., and Bochner, B.S. (1998). $\alpha\beta 2$ integrin is expressed on human eosinophils and functions as an alternative ligand for vascular cell adhesion molecule 1 (VCAM-1). *J Exp Med* *188*, 2187-2191.
- Griggs, D.W., Schmidt, C.M., and Carron, C.P. (1998). Characteristics of cation binding to the I domains of LFA-1 and MAC-1. The LFA-1 I domain contains a Ca^{2+} -binding site. *J Biol Chem* *273*, 22113-22119.
- Gullberg, D. (2014). *I Domain Integrins* (Springer).
- Hadley, G.A., and Higgins, J.M. (2014). Integrin $\alpha\text{E}\beta 7$: molecular features and functional significance in the immune system. *I Domain Integrins* *819*, 97-110.
- Hall, E.R., and Slack, R.J. (2019). The effect of divalent metal cations on the αv integrin binding site is ligand and integrin specific. *Biomed Pharmacother* *110*, 362-370.
- Hanna, S., and Etzioni, A. (2012). Leukocyte adhesion deficiencies. *Ann N Y Acad Sci* *1250*, 50-55.
- Harburger, D.S., and Calderwood, D.A. (2009). Integrin signalling at a glance. *J Cell Sci* *122*, 159-163.
- Harris, E.S., Weyrich, A.S., and Zimmerman, G.A. (2013). Lessons from rare maladies: leukocyte adhesion deficiency syndromes. *Curr Opin Hematol* *20*, 16-25.
- Hinglais, N., Kazatchkine, M.D., Mandet, C., Appay, M.D., and Bariety, J. (1989). Human liver Kupffer cells express CR1, CR3, and CR4 complement receptor antigens. An immunohistochemical study. *Lab Invest* *61*, 509-514.
- Hu, X., Wohler, J.E., Dugger, K.J., and Barnum, S.R. (2010). $\beta 2$ -Integrins in demyelinating disease: not adhering to the paradigm. *J Leukoc Biol* *87*, 397-403.
- Huth, J.R., Olejniczak, E.T., Mendoza, R., Liang, H., Harris, E.A., Lupher, M.L., Wilson, A.E., Fesik, S.W., and Staunton, D.E. (2000). NMR and mutagenesis evidence for an I domain allosteric site that regulates lymphocyte function-associated antigen 1 ligand binding. *Proc Natl Acad Sci U S A* *97*, 5231-5236.
- Hynes, R.O. (2002). Integrins: bidirectional, allosteric signaling machines. *Cell* *110*, 673-687.
- Hyun, Y.-M., Lefort, C.T., and Kim, M. (2009). Leukocyte integrins and their ligand interactions. *Immunol Res* *45*, 195-208.
- Ihanus, E., Uotila, L.M., Toivanen, A., Varis, M., and Gahmberg, C.G. (2007). Red-cell ICAM-4 is a ligand for the monocyte/macrophage integrin CD11c/CD18: characterization of the binding sites on ICAM-4. *Blood* *109*, 802-810.

- Ilari, A., and Savino, C. (2008). Protein structure determination by X-ray crystallography. *Bioinformatics* 452, 63-87.
- Jawhara, S., Pluskota, E., Cao, W., Plow, E.F., and Soloviev, D.A. (2017). Distinct effects of integrins $\alpha X\beta 2$ and $\alpha M\beta 2$ on leukocyte subpopulations during inflammation and antimicrobial responses. *Infect Immun* 85, e00644-00616.
- Jawhara, S., Pluskota, E., Verbovetskiy, D., Skomorovska-Prokvolit, O., Plow, E.F., and Soloviev, D.A. (2012). Integrin $\alpha X\beta 2$ is a leukocyte receptor for *Candida albicans* and is essential for protection against fungal infections. *J Immunol* 189, 2468-2477.
- Jelicic, I., Jelcic, I., Faigle, W., Sospedra, M., and Martin, R. (2015). Immunology of progressive multifocal leukoencephalopathy. *J Neurovirol* 21, 614-622.
- Jensen, M.R., Bajic, G., Zhang, X., Laustsen, A.K., Koldsø, H., Skeby, K.K., Schiøtt, B., Andersen, G.R., and Vorup-Jensen, T. (2016). Structural basis for simvastatin competitive antagonism of complement receptor 3. *J Biol Chem* 291, 16963-16976.
- Jin, M., Andricioaei, I., and Springer, T.A. (2004). Conversion between three conformational states of integrin I domains with a C-terminal pull spring studied with molecular dynamics. *Structure* 12, 2137-2147.
- Johnson, B.A. (2004). Using NMRView to visualize and analyze the NMR spectra of macromolecules. In *Protein NMR Techniques* (Springer), pp. 313-352.
- Johnson, M.S., and Chouhan, B.S. (2014). Evolution of integrin I domains. *I Domain Integrins* 819, 1-19.
- Kabsch, W. (1993). Automatic processing of rotation diffraction data from crystals of initially unknown symmetry and cell constants. *J Appl Crystallogr* 26, 795-800.
- Kabsch, W. (2010). Integration, scaling, space-group assignment and post-refinement. *Acta Crystallogr Sect D Biol Crystallogr* 66, 133-144.
- Kabsch, W., and Sander, C. (1983). Dictionary of protein secondary structure: pattern recognition of hydrogen-bonded and geometrical features. *Biopolymers: Original Research on Biomolecules* 22, 2577-2637.
- Keizer, G.D., Borst, J., Visser, W., Schwarting, R., de Vries, J.E., and Figdor, C.G. (1987a). Membrane glycoprotein p150,95 of human cytotoxic T cell clone is involved in conjugate formation with target cells. *J Immunol* 138, 3130-3136.
- Keizer, G.D., Te Velde, A.A., Schwarting, R., Figdor, C.G., and De Vries, J.E. (1987b). Role of p150,95 in adhesion, migration, chemotaxis and phagocytosis of human monocytes. *Eur J Immunol* 17, 1317-1322.
- Kim, M., Carman, C.V., and Springer, T.A. (2003). Bidirectional transmembrane signaling by cytoplasmic domain separation in integrins. *Science* 301, 1720-1725.

- Kollmann, C.S., Bai, X., Tsai, C.-H., Yang, H., Lind, K.E., Skinner, S.R., Zhu, Z., Israel, D.I., Cuozzo, J.W., and Morgan, B.A. (2014). Application of encoded library technology (ELT) to a protein–protein interaction target: Discovery of a potent class of integrin lymphocyte function-associated antigen 1 (LFA-1) antagonists. *Bioorg Med Chem* 22, 2353-2365.
- Krueger, J.G., Ochs, H.D., Patel, P., Gilkerson, E., Guttman-Yassky, E., and Dummer, W. (2008). Effect of therapeutic integrin (CD11a) blockade with efalizumab on immune responses to model antigens in humans: results of a randomized, single blind study. *J Invest Dermatol* 128, 2615-2624.
- Kuhlman, B., O'Neill, J.W., Kim, D.E., Zhang, K.Y., and Baker, D. (2001). Conversion of monomeric protein L to an obligate dimer by computational protein design. *Proc Natl Acad Sci U S A* 98, 10687-10691.
- Kumar, V., and Cotran, S. (2007). *St. Robbins Basic Pathology*. WB Saunders Company Philadelphia Pennsylvania 307, 1244-1246.
- Kyte, J., and Doolittle, R.F. (1982). A simple method for displaying the hydropathic character of a protein. *J Mol Biol* 157, 105-132.
- LaFoya, B., Munroe, J.A., Miyamoto, A., Detweiler, M.A., Crow, J.J., Gazdik, T., and Albig, A.R. (2018). Beyond the Matrix: The Many Non-ECM Ligands for Integrins. *Int J Mol Sci* 19.
- Lau, T.-L., Dua, V., and Ulmer, T.S. (2008a). Structure of the integrin α IIb transmembrane segment. *J Biol Chem* 283, 16162-16168.
- Lau, T.-L., Partridge, A.W., Ginsberg, M.H., and Ulmer, T.S. (2008b). Structure of the integrin β 3 transmembrane segment in phospholipid bicelles and detergent micelles. *Biochemistry* 47, 4008-4016.
- Lee, J.-O., Rieu, P., Arnaout, M.A., and Liddington, R. (1995). Crystal structure of the A domain from the α subunit of integrin CR3 (CD11 b/CD18). *Cell* 80, 631-638.
- Lee, W., Tonelli, M., and Markley, J.L. (2015). NMRFAM-SPARKY: enhanced software for biomolecular NMR spectroscopy. *Bioinformatics* 31, 1325-1327.
- Legge, G.B., Kriwacki, R.W., Chung, J., Hommel, U., Ramage, P., Case, D.A., Dyson, H.J., and Wright, P.E. (2000). NMR solution structure of the inserted domain of human leukocyte function associated antigen-1. *J Mol Biol* 295, 1251-1264.
- Leitinger, B., McDowall, A., Stanley, P., and Hogg, N. (2000). The regulation of integrin function by Ca^{2+} . *Biochim Biophys Acta* 1498, 91-98.
- Lerner, M., and Carlson, H. (2006). APBS plugin for PyMOL. Ann Arbor: University of Michigan 522.
- Liddington, R.C., and Ginsberg, M.H. (2002). Integrin activation takes shape. *J Cell Biol* 158, 833-839.

Lietha, D., and Izard, T. (2020). Roles of membrane domains in integrin-mediated cell adhesion. *Int J Mol Sci* 21, 5531-5549.

Loike, J.D., Sodeik, B., Cao, L., Leucona, S., Weitz, J.I., Detmers, P.A., Wright, S.D., and Silverstein, S.C. (1991). CD11c/CD18 on neutrophils recognizes a domain at the N terminus of the A alpha chain of fibrinogen. *Proc Natl Acad Sci U S A* 88, 1044-1048.

Lu, C., Shimaoka, M., Ferzly, M., Oxvig, C., Takagi, J., and Springer, T.A. (2001a). An isolated, surface-expressed I domain of the integrin α L β 2 is sufficient for strong adhesive function when locked in the open conformation with a disulfide bond. *Proc Natl Acad Sci U S A* 98, 2387-2392.

Lu, C., Shimaoka, M., Zang, Q., Takagi, J., and Springer, T.A. (2001b). Locking in alternate conformations of the integrin α L β 2 I domain with disulfide bonds reveals functional relationships among integrin domains. *Proc Natl Acad Sci U S A* 98, 2393-2398.

Lukácsi, S., Gerecsei, T., Balázs, K., Francz, B., Szabó, B., Erdei, A., and Bajtay, Z. (2020). The differential role of CR3 (CD11b/CD18) and CR4 (CD11c/CD18) in the adherence, migration and podosome formation of human macrophages and dendritic cells under inflammatory conditions. *PLoS One* 15, e0232432.

Luo, B.H., Carman, C.V., and Springer, T.A. (2007). Structural basis of integrin regulation and signaling. *Annu Rev Immunol* 25, 619-647.

Luo, B.H., and Springer, T.A. (2006). Integrin structures and conformational signaling. *Curr Opin Cell Biol* 18, 579-586.

Luo, B.H., Takagi, J., and Springer, T.A. (2004). Locking the beta3 integrin I-like domain into high and low affinity conformations with disulfides. *J Biol Chem* 279, 10215-10221.

Manandhar, P., Abousaway, O., Le, T., and Sen, M. (2017). Role of structural dynamics in leukocyte integrins function: interplay between the shape-shifting mechanism and allostery. *Int J Cell Sci Mol Biol* 3, 59-62.

Matulis, D., Kranz, J.K., Salemme, F.R., and Todd, M.J. (2005). Thermodynamic stability of carbonic anhydrase: measurements of binding affinity and stoichiometry using ThermoFluor. *Biochemistry* 44, 5258-5266.

McCleverty, C.J., and Liddington, R.C. (2003). Engineered allosteric mutants of the integrin alphaMbeta2 I domain: structural and functional studies. *Biochem J* 372, 121-127.

McCoy, A.J. (2007). Solving structures of protein complexes by molecular replacement with Phaser. *Acta Crystallogr Sect D Biol Crystallogr* 63, 32-41.

McPherson, A. (2004). Introduction to protein crystallization. *Methods* 34, 254-265.

Metlay, J.P., Witmer-Pack, M.D., Agger, R., Crowley, M.T., Lawless, D., and Steinman, R.M. (1990). The distinct leukocyte integrins of mouse spleen dendritic cells as identified with new hamster monoclonal antibodies. *J Exp Med* 171, 1753-1771.

- Michishita, M., Videm, V., and Arnaout, M.A. (1993). A novel divalent cation-binding site in the A domain of the beta 2 integrin CR3 (CD11b/CD18) is essential for ligand binding. *Cell* 72, 857-867.
- Miyazaki, Y., Bunting, M., Stafforini, D.M., Harris, E.S., McIntyre, T.M., Prescott, S.M., Frutuoso, V.S., Amendoeira, F.C., de Oliveira Nascimento, D., and Vieira-de-Abreu, A. (2008). Integrin α D β 2 is dynamically expressed by inflamed macrophages and alters the natural history of lethal systemic infections. *J Immunol* 180, 590-600.
- Miyazaki, Y., Vieira-de-Abreu, A., Harris, E.S., Shah, A.M., Weyrich, A.S., Castro-Faria-Neto, H.C., and Zimmerman, G.A. (2014). Integrin alphaDbeta2 (CD11d/CD18) is expressed by human circulating and tissue myeloid leukocytes and mediates inflammatory signaling. *PLoS One* 9, e112770.
- Moriarty, N.W., Grosse-Kunstleve, R.W., and Adams, P.D. (2009). electronic Ligand Builder and Optimization Workbench (eLBOW): a tool for ligand coordinate and restraint generation. *Acta Crystallogr Sect D Biol Crystallogr* 65, 1074-1080.
- Muller, W.E. (1997). Origin of metazoan adhesion molecules and adhesion receptors as deduced from cDNA analyses in the marine sponge *Geodia cydonium*: a review. *Cell Tissue Res* 289, 383-395.
- Niesen, F.H., Berglund, H., and Vedadi, M. (2007). The use of differential scanning fluorimetry to detect ligand interactions that promote protein stability. *Nat Protoc* 2, 2212-2221.
- Nishida, N., Xie, C., Shimaoka, M., Cheng, Y., Walz, T., and Springer, T.A. (2006). Activation of leukocyte β 2 integrins by conversion from bent to extended conformations. *Immunity* 25, 583-594.
- Noti, J. (2002). Expression of the myeloid-specific leukocyte integrin gene CD11d during macrophage foam cell differentiation and exposure to lipoproteins. *Int J Mol Med*.
- Ostermann, G., Weber, K.S., Zerneck, A., Schroder, A., and Weber, C. (2002). JAM-1 is a ligand of the beta(2) integrin LFA-1 involved in transendothelial migration of leukocytes. *Nat Immunol* 3, 151-158.
- Pancer, Z., Kruse, M., Muller, I., and Muller, W.E. (1997). On the origin of Metazoan adhesion receptors: cloning of integrin alpha subunit from the sponge *Geodia cydonium*. *Mol Biol Evol* 14, 391-398.
- Papanastasiou, M., Koutsogiannaki, S., Sarigiannis, Y., Geisbrecht, B.V., Ricklin, D., and Lambris, J.D. (2017). Structural implications for the formation and function of the complement effector protein iC3b. *J Immunol* 198, 3326-3335.
- Park, E.J., Myint, P.K., Ito, A., Appiah, M.G., Darkwah, S., Kawamoto, E., and Shimaoka, M. (2020). Integrin-ligand interactions in inflammation, cancer, and metabolic disease: insights into the multifaceted roles of an emerging ligand irisin. *Front Cell Dev Biol* 8, 588066.

- Piserchio, A., Dalby, K.N., and Ghose, R. (2012). Assignment of backbone resonances in a eukaryotic protein kinase—ERK2 as a representative example. In *Protein NMR techniques* (Springer), pp. 359-368.
- Popovic, N., and Wilson, E. (2018). *Cell Surface Receptors*. Elsevier, 44-54.
- Poulsen, F.M. (2002). A brief introduction to NMR spectroscopy of proteins (users.cs.duke.edu).
- Project, C.C. (1994). The CCP4 suite: programs for protein crystallography. *Acta Crystallogr Sect D Biol Crystallogr* 50, 760-763.
- Qu, A., and Leahy, D.J. (1995). Crystal structure of the I-domain from the CD11a/CD18 (LFA-1, alpha L beta 2) integrin. *Proc Natl Acad Sci U S A* 92, 10277-10281.
- Ricklin, D., Hajishengallis, G., Yang, K., and Lambris, J.D. (2010). Complement: a key system for immune surveillance and homeostasis. *Nat Immunol* 11, 785-797.
- Rosenkranz, A.R., Coxon, A., Maurer, M., Gurish, M.F., Austen, K.F., Friend, D.S., Galli, S.J., and Mayadas, T.N. (1998). Impaired mast cell development and innate immunity in Mac-1 (CD11b/CD18, CR3)-deficient mice. *J Immunol* 161, 6463-6467.
- Rosenson, R.S., Tangney, C.C., and Casey, L.C. (1999). Inhibition of proinflammatory cytokine production by pravastatin. *Lancet (British edition)* 353, 983-984.
- Sadhu, C., Ting, H.J., Lipsky, B., Hensley, K., Garcia-Martinez, L.F., Simon, S.I., and Staunton, D.E. (2007). CD11c/CD18: novel ligands and a role in delayed-type hypersensitivity. *J Leukoc Biol* 81, 1395-1403.
- Schittenhelm, L., Hilkens, C.M., and Morrison, V.L. (2017). β 2 integrins as regulators of dendritic cell, monocyte, and macrophage function. *Front Immunol* 8, 1866-1876.
- Sebastian, E.S., Mercero, J.M., Stote, R.H., Dejaegere, A., Cossío, F.P., and Lopez, X. (2006). On the affinity regulation of the metal-ion-dependent adhesion sites in integrins. *J Am Chem Soc* 128, 3554-3563.
- Sen, M., Koxsal, A.C., Yuki, K., Wang, J., and Springer, T.A. (2018). Ligand- and cation-induced structural alterations of the leukocyte integrin LFA-1. *J Biol Chem* 293, 6565-6577.
- Sen, M., and Springer, T.A. (2016). Leukocyte integrin α L β 2 headpiece structures: The α I domain, the pocket for the internal ligand, and concerted movements of its loops. *Proc Natl Acad Sci U S A* 113, 2940-2945.
- Sen, M., Yuki, K., and Springer, T.A. (2013). An internal ligand-bound, metastable state of a leukocyte integrin, α X β 2. *J Cell Biol* 203, 629-642.
- Senisterra, G.A., Markin, E., Yamazaki, K., Hui, R., Vedadi, M., and Awrey, D.E. (2006). Screening for ligands using a generic and high-throughput light-scattering-based assay. *J Biomol Screen* 11, 940-948.

- Shimaoka, M., Lu, C., Palframan, R.T., von Andrian, U.H., McCormack, A., Takagi, J., and Springer, T.A. (2001). Reversibly locking a protein fold in an active conformation with a disulfide bond: integrin α L I domains with high affinity and antagonist activity in vivo. *Proc Natl Acad Sci U S A* *98*, 6009-6014.
- Shimaoka, M., Lu, C., Salas, A., Xiao, T., Takagi, J., and Springer, T.A. (2002). Stabilizing the integrin α M inserted domain in alternative conformations with a range of engineered disulfide bonds. *Proc Natl Acad Sci U S A* *99*, 16737-16741.
- Shimaoka, M., Salas, A., Yang, W., Weitz-Schmidt, G., and Springer, T.A. (2003a). Small molecule integrin antagonists that bind to the β 2 subunit I-like domain and activate signals in one direction and block them in the other. *Immunity* *19*, 391-402.
- Shimaoka, M., Xiao, T., Liu, J.H., Yang, Y., Dong, Y., Jun, C.D., McCormack, A., Zhang, R., Joachimiak, A., Takagi, J., *et al.* (2003b). Structures of the alpha L I domain and its complex with ICAM-1 reveal a shape-shifting pathway for integrin regulation. *Cell* *112*, 99-111.
- Shrake, A., and Ross, P. (1988). Biphasic denaturation of human albumin due to ligand redistribution during unfolding. *J Biol Chem* *263*, 15392-15399.
- Siegers, G.M., Barreira, C.R., Postovit, L.M., and Dekaban, G.A. (2017). CD11d beta2 integrin expression on human NK, B, and gammadelta T cells. *J Leukoc Biol* *101*, 1029-1035.
- Song, C., Zhang, S., and Huang, H. (2015). Choosing a suitable method for the identification of replication origins in microbial genomes. *Front Microbiol* *6*, 1049.
- Springer, T.A. (1997). Folding of the N-terminal, ligand-binding region of integrin alpha-subunits into a beta-propeller domain. *Proc Natl Acad Sci U S A* *94*, 65-72.
- Springer, T.A., and Dustin, M.L. (2012). Integrin inside-out signaling and the immunological synapse. *Curr Opin Cell Biol* *24*, 107-115.
- Springer, T.A., and Wang, J.H. (2004). The three-dimensional structure of integrins and their ligands, and conformational regulation of cell adhesion. *Adv Protein Chem* *68*, 29-63.
- Stefanidakis, M., and Koivunen, E. (2006). Cell-surface association between matrix metalloproteinases and integrins: role of the complexes in leukocyte migration and cancer progression. *Blood* *108*, 1441-1450.
- Stewart, M., Thiel, M., and Hogg, N. (1995). Leukocyte integrins. *Curr Opin Cell Biol* *7*, 690-696.
- Takada, Y., Ye, X., and Simon, S. (2007). The integrins. *Genome Biol* *8*, 1-9.
- Takagi, J., Erickson, H.P., and Springer, T.A. (2001). C-terminal opening mimics 'inside-out' activation of integrin alpha5beta1. *Nat Struct Biol* *8*, 412-416.

Takagi, J., Petre, B.M., Walz, T., and Springer, T.A. (2002). Global conformational rearrangements in integrin extracellular domains in outside-in and inside-out signaling. *Cell* *110*, 599-511.

Takagi, J., and Springer, T.A. (2002). Integrin activation and structural rearrangement. *Immunol Rev* *186*, 141-163.

Tang, R.-H., Tng, E., Law, S.A., and Tan, S.-M. (2005). Epitope mapping of monoclonal antibody to integrin α L β 2 hybrid domain suggests different requirements of affinity states for intercellular adhesion molecules (ICAM)-1 and ICAM-3 binding. *J Biol Chem* *280*, 29208-29216.

Thomas, A.P., Dunn, T.N., Oort, P.J., Grino, M., and Adams, S.H. (2011). Inflammatory phenotyping identifies CD11d as a gene markedly induced in white adipose tissue in obese rodents and women. *J Nutr* *141*, 1172-1180.

Tian, L., Yoshihara, Y., Mizuno, T., Mori, K., and Gahmberg, C.G. (1997). The neuronal glycoprotein telencephalin is a cellular ligand for the CD11a/CD18 leukocyte integrin. *J Immunol* *158*, 928-936.

Van der Vieren, M., Crowe, D.T., Hoekstra, D., Vazeux, R., Hoffman, P.A., Grayson, M.H., Bochner, B.S., Gallatin, W.M., and Staunton, D.E. (1999). The leukocyte integrin α D β 2 binds VCAM-1: evidence for a binding interface between I domain and VCAM-1. *J Immunol* *163*, 1984-1990.

Velázquez-Campoy, A., Ohtaka, H., Nezami, A., Muzammil, S., and Freire, E. (2004). Isothermal titration calorimetry. *Curr Protoc Cell Biol* *23*, 17-28.

Vinogradova, O., Velyvis, A., Velyviene, A., Hu, B., Haas, T., Plow, E., and Qin, J. (2002). A structural mechanism of integrin α (IIb) β (3) "inside-out" activation as regulated by its cytoplasmic face. *Cell* *110*, 587-597.

Vorup-Jensen, T., Carman, C.V., Shimaoka, M., Schuck, P., Svitel, J., and Springer, T.A. (2005). Exposure of acidic residues as a danger signal for recognition of fibrinogen and other macromolecules by integrin α X β 2. *Proc Natl Acad Sci U S A* *102*, 1614-1619.

Vorup-Jensen, T., Chi, L., Gjelstrup, L.C., Jensen, U.B., Jewett, C.A., Xie, C., Shimaoka, M., Linhardt, R.J., and Springer, T.A. (2007a). Binding between the integrin α X β 2 (CD11c/CD18) and heparin. *J Biol Chem* *282*, 30869-30877.

Vorup-Jensen, T., and Jensen, R.K. (2018). Structural immunology of complement receptors 3 and 4. *Front Immunol* *9*, 2716.

Vorup-Jensen, T., Ostermeier, C., Shimaoka, M., Hommel, U., and Springer, T.A. (2003). Structure and allosteric regulation of the α X β 2 integrin I domain. *Proc Natl Acad Sci U S A* *100*, 1873-1878.

- Vorup-Jensen, T., Waldron, T.T., Astrof, N., Shimaoka, M., and Springer, T.A. (2007b). The connection between metal ion affinity and ligand affinity in integrin I domains. *Biochimica et Biophysica Acta (BBA)-Proteins and Proteomics* *1774*, 1148-1155.
- Wagner, C., Hansch, G.M., Stegmaier, S., Deneffle, B., Hug, F., and Schoels, M. (2001). The complement receptor 3, CR3 (CD11b/CD18), on T lymphocytes: activation-dependent up-regulation and regulatory function. *Eur J Immunol* *31*, 1173-1180.
- Wegener, K.L., and Campbell, I.D. (2008). Transmembrane and cytoplasmic domains in integrin activation and protein-protein interactions (review). *Mol Membr Biol* *25*, 376-387.
- Weitz-Schmidt, G., Welzenbach, K., Brinkmann, V., Kamata, T., Kallen, J., Bruns, C., Cottens, S., Takada, Y., and Hommel, U. (2001). Statins selectively inhibit leukocyte function antigen-1 by binding to a novel regulatory integrin site. *Nat Med* *7*, 687-692.
- Whittaker, C.A., and Hynes, R.O. (2002). Distribution and evolution of von Willebrand/integrin A domains: widely dispersed domains with roles in cell adhesion and elsewhere. *Mol Biol Cell* *13*, 3369-3387.
- Wong, D.A., Davis, E.M., LeBeau, M., and Springer, T.A. (1996). Cloning and chromosomal localization of a novel gene-encoding a human beta 2-integrin alpha subunit. *Gene* *171*, 291-294.
- Wu, H., Gower, R.M., Wang, H., Perrard, X.Y., Ma, R., Bullard, D.C., Burns, A.R., Paul, A., Smith, C.W., Simon, S.I., *et al.* (2009). Functional role of CD11c⁺ monocytes in atherosclerosis associated with hypercholesterolemia. *Circulation* *119*, 2708-2717.
- Wu, H., Rodgers, J.R., Perrard, X.Y., Perrard, J.L., Prince, J.E., Abe, Y., Davis, B.K., Dietsch, G., Smith, C.W., and Ballantyne, C.M. (2004). Deficiency of CD11b or CD11d results in reduced staphylococcal enterotoxin-induced T cell response and T cell phenotypic changes. *J Immunol* *173*, 297-306.
- Xiao, T., Takagi, J., Collier, B.S., Wang, J.H., and Springer, T.A. (2004). Structural basis for allostery in integrins and binding to fibrinogen-mimetic therapeutics. *Nature* *432*, 59-67.
- Xie, C., Zhu, J., Chen, X., Mi, L., Nishida, N., and Springer, T.A. (2010). Structure of an integrin with an alphaI domain, complement receptor type 4. *EMBO J* *29*, 666-679.
- Xiong, J.P., Stehle, T., Diefenbach, B., Zhang, R., Dunker, R., Scott, D.L., Joachimiak, A., Goodman, S.L., and Arnaout, M.A. (2001). Crystal structure of the extracellular segment of integrin alpha Vbeta3. *Science* *294*, 339-345.
- Xu, S., Wang, J., Wang, J.H., and Springer, T.A. (2017). Distinct recognition of complement iC3b by integrins alphaXbeta2 and alphaMbeta2. *Proc Natl Acad Sci U S A* *114*, 3403-3408.
- Xua, S., Wangb, J., Wangc, J.-H., and Springerb, T.A. (2017). Distinct recognition of complement iC3b by integrins. *Proc Natl Acad Sci U S A* *114*, 3403-3408.

Yakubenko, V.P., Belevych, N., Mishchuk, D., Schurin, A., Lam, S.C., and Ugarova, T.P. (2008). The role of integrin alpha D beta2 (CD11d/CD18) in monocyte/macrophage migration. *Exp Cell Res* 314, 2569-2578.

Yakubenko, V.P., Yadav, S.P., and Ugarova, T.P. (2006). Integrin α D β 2, an adhesion receptor up-regulated on macrophage foam cells, exhibits multiligand-binding properties. *Blood* 107, 1643-1650.

Yang, J., Ma, Y.-Q., Page, R.C., Misra, S., Plow, E.F., and Qin, J. (2009). Structure of an integrin α IIb β 3 transmembrane-cytoplasmic heterocomplex provides insight into integrin activation. *Proc Natl Acad Sci U S A* 106, 17729-17734.

Zamir, E., and Geiger, B. (2001). Molecular complexity and dynamics of cell-matrix adhesions. *J Cell Sci* 114, 3583-3590.

Zhang, K., and Chen, J. (2012). The regulation of integrin function by divalent cations. *Cell adhesion & migration* 6, 20-29.

Zhu, J., Luo, B.H., Xiao, T., Zhang, C., Nishida, N., and Springer, T.A. (2008). Structure of a complete integrin ectodomain in a physiologic resting state and activation and deactivation by applied forces. *Mol Cell* 32, 849-861.